**People's Democratic Republic of Algeria**

**Ministry of Higher Education and Scientific Research**


National Polytechnic School

Department of Electronic

Laboratory of Signal and Communication

(LSC)


# PhD Thesis in Electronic

Presented by:


**Widad BELAOURA**


Entitled:

## Study of the transmitter-receiver architectures based on the combination of multi-antenna techniques and spatial modulation, and the optimization of communication quality

**Jury members:**

| | | |
|---|---|---|
| **Chair:** | Rachida Touhami | Professor / ENP. |
| **Supervisors:** | Khalida Ghanem | Research Director / CDTA, Algiers. |
| | Hicham Bousbia-Salah | MCA / ENP. |
| **Examiners:** | Latifa Hamami | Professor / ENP. |
| | Abderrazak Guessoum | Professor / Blida University. |
| | Belkacem Fergani | Professor / USTHB. |
| | Abdelkrim Hamza | MCA/ USTHB. |
| **Invited:** | Amine Mokraoui | MCB / ENP. |


ENP 2019

E.N.P. 10, Avenue HASSEN BADI –EL-HARRACH– ALGIERS.

**People's Democratic Republic of Algeria**

**Ministry of Higher Education and Scientific Research**


National Polytechnic School

Department of Electronic

Laboratory of Signal and Communication

(LSC)


# PhD Thesis in Electronic

Presented by:


**Widad BELAOURA**


Entitled:

## Study of the transmitter-receiver architectures based on the combination of multi-antenna techniques and spatial modulation, and the optimization of communication quality

**Jury members:**

| | | |
|---|---|---|
| **Chair:** | Rachida Touhami | Professor / ENP. |
| **Supervisors:** | Khalida Ghanem | Research Director / CDTA, Algiers. |
| | Hicham Bousbia-Salah | MCA / ENP. |
| **Examiners:** | Latifa Hamami | Professor / ENP. |
| | Abderrazak Guessoum | Professor / Blida University. |
| | Belkacem Fergani | Professor / USTHB. |
| | Abdelkrim Hamza | MCA/ USTHB. |
| **Invited:** | Amine Mokraoui | MCB / ENP. |


ENP 2019

E.N.P. 10, Avenue HASSEN BADI –EL-HARRACH– ALGIERS.

République Algérienne Démocratique et Populaire
Ministère de l'Enseignement Supérieur et de la Recherche Scientifique

Ecole Nationale Polytechnique
Département D'Electronique
Laboratoire Signal et Communication
(LSC)

**THESE**

Présentée pour l'obtention du diplôme DOCTEUR

**Filière**

Electronique

**Par : Melle. Widad BELAOURA**

Magister en Génie Electrique, Spécialité Télécommunication, Ecole Militaire Polytechnique (EMP), Alger.

# Etude d'architectures d'émetteurs et de récepteurs basées sur la combinaison des techniques multi antennes et de la modulation spatiale, et optimisation de la qualité de la communication

| | | |
|---|---|---|
| **Présidente** : | Rachida Touhami | Professeur /ENP. |
| **Directeurs** : | Khalida Ghanem | Directeur de recherche / CDTA, Alger. |
| | Hicham Bousbia-Salah | MCA / ENP. |
| **Examinateurs :** | Latifa Hamami | Professeur / ENP. |
| | Abderrazak Guessoum | Professeur / Blida. |
| | Belkacem Fergani | Professeur / USTHB. |
| | Abdelkrim Hamza | MCA / USTHB. |
| **Invité :** | Amine Mokraoui | MCB / ENP. |

ENP 2019

E.N.P. 10, Avenue HASSEN BADI –EL-HARRACH– ALGER.

# Acknowledgement

This thesis has been conducted at both the Telecommunications division at Centre de Développement des Technologies Avancées (CDTA), and the Laboratory of Signal and Communication in the Department of Electronic of Ecole Nationale Polytechnique (ENP) of Algiers.

First of all, thanks to almighty **ALLAH** for giving me strength and ability to understand, learn and accomplish my academic goals.

I would like to express my gratitude to my PhD supervisor Research director. **Ghanem Khalida** for providing me the opportunity to work with her, for her patience, motivation, and immense knowledge. She has made considerable efforts to help me provide the means to complete my work, beyond what could be expected. I consider myself to be really fortunate to have had the opportunity to work with such talented person.

I would like to express my deep and sincere gratitude to my Co-director Dr. **Hicham Bousbia-Salah** for his academic advise and his expert opinion and generous support throughout my doctoral studies.

I would like to thank the rest of my thesis committee: Prof. **Rachida Touhami**, Prof. **Latifa Hamami**, Prof. **Abderrazak Guessoum**, Prof. **Belkacem Ferguani**, Dr. **Abdelakrin Hamza**, and Dr. **Amine Mokraoui** for their insightful comments and their constructive analysis of the present work.

My sincere thanks also goes to Prof. **Mourad Nedil**, Professor-researcher at the University of Quebec in Abitibi-Temiscamingue (UQAT), Canada, and Dr. **Muhammad Zeeshan Shakir**, Associate Professor at the University of West of Scotland (UWS), UK, for their contributions in carrying out the work in this thesis.

I would like to thank my family: my parents and to my brothers and sisters for supporting me spiritually throughout writing this thesis and my life in general.

Finally, to all people who were involved in the accomplishment of this chapter of my life -THANK YOU!

**ملخص**

يتطلب تحقيق هوائيات **MIMO** في الاتصالات العملية تحت سطح الأرض، معالجة العديد من التحديات الرئيسية: (1) تقدير القناة ، (2) عيوب الأجهزة. في هذه الأطروحة، نهدف إلى تحسين المفاضلة بين الأداء وتعقيد النظام مع التركيز بشكل خاص على الاتصالات تحت الأرض متعددة الهوائيات بناءً على قياسات حقيقية للقناة التي تم إجراؤها في النطاق**60 GHz**. في هذا السياق، نقدم أولاً مساهمة في دراسة بنية جديدة تشتمل على **hybrid beamforming MIMO** حيث تم دمج عيوب الأجهزة في معالجة جهاز الإرسال والاستقبال. نقترح بعد ذلك معالجة forward-backward منخفضة التعقيد من أجل تقدير قناة تحت الأرض في نظام **STBC-FBMC**. أخيرًا، نحول انتباهنا إلى أنظمة **MU-MIMO mm-Wave** واقترحنا تصميمًا جديدًا UAV تعمل فيه الطائرات بدون طيار كمرحل للتشكيل الشعاعي، وبالتالي تخفيف عيوب انسداد **LOS** وتداخل الوصول المتعدد. يتم التحقق من أداء الأنظمة المقترحة من خلال المحاكاة لتأكيد كفاءة الأنظمة المقترحة.

**كلمات مفتاحية**

تحت الأرض **MIMO**، تقدير القناة ، الترميز الهجين ،

**Résumé :**

La réalisation des antennes MIMO dans les communications pratiques souterraines à ondes millimétriques nécessite toutefois des défis majeurs restent à relever: (i) l'estimation du canal, (ii) la dégradation du matériel. Dans le cadre de cette thèse, nous visons à améliorer le compromis entre performances et complexité du système, en mettant l'accent sur les communications souterraines à plusieurs antennes basées sur des mesures réelles de canal effectuée dans la bande de 60 GHz. Dans ce contexte, d'abord nous présentons une nouvelle architecture englobant la structure beamforming hybride MIMO, dans laquelle les dégradations matérielles ont été intégrées au traitement de l'émetteur-récepteur. Nous proposons ensuite un traitement forward-backward avec une faible complexité pour estimer le canal souterraine dans le système STBC-FBMC. Enfin, nous portons notre attention sur les systèmes MU-MIMO mm-Wave et proposons une nouvelle conception du déploiement de UAV dans laquelle le UAV fonctionne comme un relais beamforming, atténuant ainsi les inconvénients du blocage LOS et des interférences d'accès multiples. Les performances des systèmes proposés sont vérifiées par simulation pour confirmer l'efficacité des systèmes proposés.

**Mots Clés :**

Estimation de canal, beamforming hybride, MIMO souterraine

**Abstract:**

Realizing MIMO antennas in practical mm-Wave underground mining communications, however, requires addressing several key challenges: (i) channel estimation, (ii) hardware impairments. In this thesis, we aim to improve the trade-off between performances and system complexity with special focus toward multiple-antenna underground communications based on real channel measurements carried out at the 60 GHz band. In this context, we first present a contribution to study a novel architecture encompassing hybrid precoded mm-Wave MIMO structure, in which the hardware impairments have been incorporated in the transceiver processing. We then propose a low complexity forward-backward processing for underground mm-Wave channel estimation in the STBC-FBMC system. Finally, we turn our attention to mm-Wave MU-MIMO systems and proposed a new design of UAV deployment in which UAV operates as a beamforming relay, thereby mitigating the drawbacks of LOS blockage and multiple access interference. The performances of the proposed systems are verified by simulation to confirm the efficiency of the proposed systems.

**Keywords:**

Channel estimation, hybrid precoding, MIMO underground.

# CONTENTS

# LIST OF FIGURES

| | |
|---|---|
| 4G | Fourth Generation. |
| 5G | Fifth Generation. |
| A2A | Air to Air. |
| A2G | Air to ground. |
| AF | Amplify-and-Forward. |
| AWGN | Additive White Gaussian Noise. |
| AoA | Angle-of-Arrival. |
| AoD | Angle-of-Departure. |
| BER | Bit Error Rate. |
| BPSK | Binary Phase Shift Keying. |
| BS | Base Station. |
| CP | Cyclic prefix |
| CS | Compressive Sensing. |
| CIR | Channel Impulse Response. |
| CSI | Channel State Information. |
| CDF | Cumulative Distribution Function. |
| dB | decibel. |
| DOA | Direction of Arrival. |
| DOD | Direction of Departure. |
| DFT | Discrete Fourier Transform. |
| DoF | degree of freedom. |
| DL | Downlink |
| FDD | Frequency Division Duplexing. |
| DFT | Discret Fourier Transform. |
| FFT | Fast Fourier Transform. |
| FB | Forward-Backward. |
| FBMC | Filter-Bank Multi-Carrier. |
| FDD | Frequency Division Duplexing. |
| GHz | Giga Hertz. |
| Gbps | Giga Bits per Second. |
| HD | Half Duplex. |
| ICI | Inter Channel Interference. |
| IDFT | Inverse Discrete Fourier Transform. |
| IFFT | Inverse Fast Fourier Transform. |
| i.i.d | independent and identically distributed. |
| ISI | Inter Symbol Interference. |

| | |
|---|---|
| LOS | Line Of Sight. |
| LS | Least-Squares. |
| LTE | Long Term Evolution. |
| MIMO | Multiple Input Multiple Output |
| MISO | Multiple-Input Single-Output |
| Mm-Wave | Millimeter-Wave. |
| MMSE | Normalized Mean-Squared Error |
| MRC | Maximum Ratio Combining. |
| NLOS | None Line Of Sight. |
| OFDM | Orthogonal Frequency Division Multiplexing. |
| OQAM | Offset quadrature amplitude modulation. |
| OMP | orthogonal matching pursuit. |
| PA | Power Amplifier. |
| PL | path loss. |
| PN | Phase Noise. |
| PDP | Power Delay Profile. |
| PAPR | Peak to Average Power Ratio. |
| PHYDYAS | PHYsical layer for DYnamic spectrum AccesS and cognitive radio. |
| QoS | Quality of Service. |
| QAM | Quadrature Amplitude Modulation. |
| QPSK | Quadrature Phase Shift Keying. |
| RF | Radio Frequency. |
| SISO | Soft-Input Soft-Output. |
| SNR | Signal to Noise Ratio. |
| SINR | Signal-to-Interference-plus-Noise Ratio. |
| SVD | Singular Value Decomposition. |
| STBC | Space Time Bloc Code. |
| STC | Space-Time Coding. |
| SCN | Small Cell Network. |
| TDD | Time Division Duplexing. |
| UL | Uplink. |
| ZF | Zero Forcing. |
| 2D | Two Dimension. |
| 2D | Three Dimension. |
| ULA | Uniform Linear Array. |
| USPA | Uniform Square Planar Array. |
| UAV | Unmanned Aerial Vehicles. |

# CHAPTER 1

# GENERAL INTRODUCTION

## Contents

Wireless communications have attracted a great deal of interest due to the change in the way today's society creates, and consumes information, which most of the times require higher investments at the deployment process. Perhaps, it is fair to say that mobile communications, which directly impact our daily lives, have seen the most astonishing advancements of wireless communications [1]. This has become more prominent with the shift in paradigm of communication from voice centric to data centric. On the other side, the evolution of wireless data applications and increasing popularity of smart devices have led to a massive proliferation in mobile data traffic, creating radical challenges for mobile service providers.These escalating demands have shaped the design of the upcoming fifth generation (5G) of mobile networks, which is expected to support ubiquitous connectivity via quality-of-service (QoS) provisioned applications and services [2].

## 1.1 Background and Motivation

Nowadays, there is a rapidly growing interest in 5G wireless systems due to many benefits, such as ubiquitous connectivity, high data rates, improved reliability and scalability, ultra-low latency and low energy consumption [3, 4]. Towards these directions, a lot of emerging or evolutionary technologies have been already developed for 5G systems. The ambitious goals set for 5G wireless networks require dramatic changes in the design of different layers for next generation communications systems. Massive multiple-input multiple-output (MIMO) systems, filter bank multi-carrier (FBMC) modulation, non-orthogonal multiple access (NOMA), relaying technologies, and millimeter-Wave (mm-Wave) communications have been considered as some of the strong candidates for the physical layer design of 5G networks [5, 6].

In the field of wireless communication, multiple input multiple output (MIMO) is considered as the major technical breakthrough in recent years. MIMO systems utilize multiple antennas at transmitter, as well as receiver, to attain different gains through spatial multiplexing, diversity and beamforming [7]. As an extension of traditional MIMO technology, massive MIMO can greatly meet the specific 5G requirements, and is considered as an innovative research direction of 5G wireless communication [8]. Massive MIMO technology has the capacity to achieve the desired rate of 5G in terms of spectral efficiency (SE) and system throughput, by introducing several hundreds of antenna elements at the transmitter and/or receiver [7, 9]. This results in practically reducing the impacts of channel fading, interference and additive noise [10, 11].

The spectrum scarcity at sub-6 GHz frequency bands stimulated a new wave of wireless research that focuses on higher bands, namely mm-Wave. The mm-Wave communication has been retained as an attractive candidate for the 5G network first because it allows to realize a Gbps data transmission, it offers a huge amount of bandwidth resources between 30-300 GHz, and provides great potentialities for antennas miniaturization [12, 13]. These large, safe, and unoccupied frequency resources will help to alleviate the capacity limitation of current wireless systems and enable very high-speed applications [14, 15]. In the last decade, the unlicensed spectrum around 60 GHz has been applied to underground network, exploring the indoor use of mm-Wave communications [16, 17].

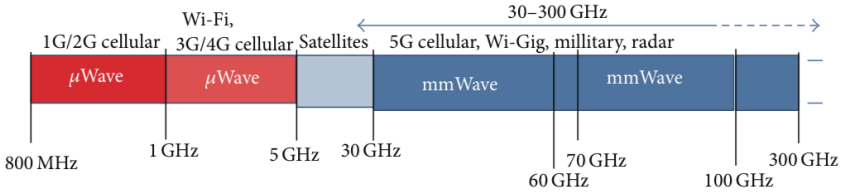


Figure 1.1: Available bandwidth in the mm-Wave spectrum

In a parallel avenue, another important axis of the research for 5G transmission, is the design of new waveforms for physical layer with better spectral properties. Among several new waveform candidates, FBMC systems have been considered as a promising multi-carrier modulation transmission technique [18]. This latter has been recently proposed as an efficient alternative to orthogonal frequency division multiplexing (OFDM) candidate since it does not require a cyclic prefix, and thus, it has a higher SE. The FBMC system, utilizes a specially designed prototype filter which is well localized both in time and frequency, which enables it to have a higher SE and a better spectral containment; making it more appealing than OFDM for 5G network. Therefore, it is possible to combine FBMC and mm-Wave systems to offer a higher data rate and a better spectrum efficiency for MIMO systems [19].

With the recent research on mm-Wave frequency bands, communications over underground mine environment at 60 GHz are regarded as the most important solution to improve the quality of mining communication applications, such as tele-montoring, video tele-surveillance, thereby enhancing productivity and safety. At high frequency band, one of the biggest challenges in this environment is related to its high propagation loss due to unfavorable oxygen absorption, and reflective indoor materials. Furthermore, underground channel is known by its high walls and galleries irregularities, and the superimposing of different layers and materials with different electrical

and magnetic characteristics, and by its wave-guide effect, which hinders the communication scheme throughput enhancement [20]. To bridge the resulting significant link budget gap in such environments, several real-world measurements around 60 GHz, carried out in underground mine environments, have revealed that using multi-antenna systems offers substantial capabilities in improving the transmission rate and reliability over the resulting channel [20–23].

Recently, a certain deal of research has been carried out to investigate multiple antennas for underground mine communications, since it can offer high improvements in throughput, as well as in energy efficiency [20, 24]. However, many challenges need to be addressed before building a commercially viable network. One important issue in this context is the design of radio frequency (RF) practical transceivers, which particularly operate at mm-Wave frequency bands, in which additional impairments are known to have a detrimental impact, such as in-phase/quadrature-phase (I/Q) imbalance, oscillator phase noise (PN), and power amplifier non-linearities at the transmitter [25]. Although the influence of these impairments can be mitigated by calibration schemes and compensation algorithms at the transceiver, there still remain residual impairments due to inaccurate calibration methods, and different types of noise [25]. Therefore, proper modeling of these imperfections at the mm-Wave range is of a special importance, and impose a huge challenge on developing new configurations in upcoming 5G wireless communication, as these imperfections dominate the performance of the overall system [26–28]. As a result, considering fundamental trade-offs over performance, power consumption and cost, the detrimental effects of RF impairments will be more pronounced in the transceivers operating at mm-Wave frequencies.

Theoretically, scaling up the number of antennas at the transmission and/or the reception leads to the enhancement of the throughput, to the generation of extra degrees of freedom (DoF) in the spatial domain, and to the mitigation of the effects of channel fading, which motivates the migration towards the concept of massive MIMO in mm-Wave bands [7, 9]. Moreover, large antenna arrays help the design of beamforming or precoding techniques to stear the signal in a certain direction, hence combating the severe path loss witnessed in mm-Wave channels. Nevertheless, realizing the beamforming operation with large-scale antenna arrays is not straightforward in mm-Wave systems. Traditional fully digital beamforming requires to equip one dedicated RF chain to each antenna element. Unfortunately, this fully-digital beamforming architecture cannot be practically employed in mm-Wave MIMO systems due to the unaffordable cost and power consumption of large numbers of mm-Wave RF

chains and other hardware components [29,30]. An elegant solution to remedy these inherent problems is to offload part of the beamforming to the FR domain, via analog beamforming, where the phase of the transmitted signal at each antenna element is controlled via a network of analog phase shifters. Compared to the digital beamforming, analog one is economically more attractive, nevertheless, its performance is inferior as it does not control the magnitude of the beamformer elements.

Recently, hybrid analog/digital beamforming has emerged as a potential solution for practical mm-Wave MIMO communications through striking a trade-off between system performance and hardware efficiency [31]. The hybrid beamforming architecture employs only a few RF chains to realize low dimensional digital beamformers and a large number of cost-efficient phase shifters to implement high-dimensional analog beamformers. As a result, the analog beamformers can provide a sufficient beamforming gain to compensate for the huge path loss in mm-Wave frequency bands, and the digital beamformers can offer the flexibility to realize multi-user/multiplexing techniques. While hybrid architectures were shown to provide achievable rates close to those of fully-digital architectures [31], they pose more constraints that complicate the channel estimation, more particularly under hardware impairments problem [32,33].

Indeed, working on the range of mm-Wave can be very beneficial to the new 5G networks, however, estimating the resulting channel sufficiently and accurately can be challenging, due to both low coherence time, pilot overhead, and a large number of antennas. Besides, conventional channel estimators, such as the least square (LS) estimator, demand a large amount of training resources, which can be impractical in mm-Wave systems. Fortunately, due to the sparse multi-path structure at the mm-Wave frequencies, a clever and a low-complexity channel estimation approach, which takes a full advantage of the inherent sparsity, has been recently introduced through the compressive sensing (CS) paradigm [34,35]. One attractive feature of CS-based estimation techniques is its evaluation of the channel parameters with less training data resources, rendering the training overhead reduced. The mm-Wave underground channels, as well, are sparse in the delay domain due to the limited number of significant channel gains effectively contributing in the propagation, thereby creating a sparsity which could be exploited to perform the CS channel estimation.

As previously mentioned, eventhough mm-Wave communications are among the mostly agreed-upon solutions to retain for future standards, this great potential is hindered by the associated severe path loss, their specific propagation characteristics, and their sensitivity to blockage from surrounding objects, e.g. high-rise build-

ings. Worthy to recall that in the particular case of ground-based radio, the line of sight (LOS) between ground nodes is often obstructed by obstacles; which makes the communication unreliable and inefficient [12, 36]. In the other hand, high channel dynamics, particularly in some outdoor environments, make the prevention of the blockage a quite challenging problem. Therefore, ensuring the communication between many ground base stations (BSs) and users reliably in urban environments is a quite challenging problem, due to the limited bandwidth and effective range of the communication equipment and the physical obscuration or occlusion [37].

To cope with the open research problems, researchers have proposed to endow the antennas operating in mm-Wave frequency bands with transmit hybrid beamforming capabilities, which alleviates the propagation impediments in such bands [31]. However, having solely recourse to hybrid beamforming techniques, or increasing the transmit power, constitutes a solution with a limited efficiency to the blockage drawback, and may even induce side effects. Interestingly, it is agreed upon nowadays that equipping the wireless communication systems in general, and the mm-Wave ones in particular, with cooperative relays and an efficient association between the source and the destination, allows to effectively extend both their range and their throughput [38, 39]. The joint user association and relaying is particularly important in mm-Wave networks due to the limited size of the cells.

Communications via unmanned aerial vehicles (UAVs), popularly referred to as drones, are one of the most important enabling technologies to realize a huge amount of connections for the upcoming 5G and beyond wireless networks. Recently, UAV communication has attracted lots of attention in both industry and academia [40–43]. This interest is motivated by their avoidance of the classical wireless communication scatters which degrade the communications quality, their large coverage and supervision of wide areas, and their targeting of potential applications such as police patrolling, surveillance, and as communication relays [40]. Compared to the deployment of conventional terrestrial infrastructures, such as ground relays, the aerial relay-assisted communications provide effective ways to prolong the mm-Wave communication range and offer a better signal quality [41, 44]. On one hand, the UAV relay can move freely in the three-dimensional (3D) space to adapt to the network mobility and enhance the system performance. On the other hand, the air-ground communications could bypass the obstacles on the ground, and are more likely to have LOS links, thus a better channel gain, which enables a higher link capacity and a lower power consumption [42].

In any practical mm-Wave communication network, there are many neighboring

BSs surrounded by a number of users, where the channel to each of these BS can vary significantly given the erratic nature of mm-Wave propagation with probabilistic LOS, and non-LOS (NLOS). Because of the higher path loss and sensitivity to blockage, mm-Wave signals can only propagate to much short distances, making it necessary for the mm-Wave network to use association mechanism [45, 46]. User association is necessary to determine which BS a user connects to in order to maximize BS throughput. Given that mm-Wave connections are highly directional and vulnerable to small channel variations, user association changes these connections and hence significantly affects the user's instantaneous rate, as well as network interference [47].

## 1.2 Contributions

Inspired by the above discussion, in this thesis, we provide a holistic study of the mm-Wave communication and the importance of using a large number of antennas, in order to improve the performances of the mm-Wave underground mine communication. In particular, large MIMO antenna arrays can help overcoming the dependency of path-loss on frequency in mm-Wave systems and cancel the worst conditions of propagation of underground mine environment. Nonetheless, they may require an efficient channel estimation, which will lead to new types of deployments. Consequently, in this thesis, we have taken as a topic for study the incorporation of 5G systems and beyond, in indoor and outdoor environments. As a representative of indoor environment the very specific underground mine channel was of interest. We have particularly focused on two critical aspects in practice, namely channel estimation problem and achievable data rate of large MIMO configuration when deployed there under hardware impairments. For the outdoor environment, we have taken as a study case a flexible cellular system, the futuristic UAV-based relaying architecture. The system was endowed with multi-user mm-Wave MIMO-OFDM capabilities. The most important contributions along with related publications are organized as follows:

- In Chapter 3, for the first time, real-world channel measurements carried out at the 60 GHz frequency band are used to analyze the performance of the proposed architecture encompassing the hybrid beamfomer structure for large MIMO underground communication system, in which the hardware impairment effects have been incorporated in the transceiver processing. Furthermore, a 2-D geometrical channel model, which is based on one ring configuration, to describe

the propagation mechanism in the underground channel, is applied on the measured channel on which the new proposed MIMO underground architecture is tested. The achievable rate performance is investigated based on this geometrical model and the modified transceiver structure for different configurations.

- In Chapter 4, our contributions have concerned underground channel estimation problems. Motivated by the spasre nature of the mm-Wave underground channel, a novel low complexity channel estimation that is based on the compressive sensing theory is proposed and incorporated into a new $2 \times 1$ STBC-FBMC/QAM system equipped with a pair of prototype filters. The proposed estimator relies on the forward-backward (FB) processing to accurately identify the sparse components of the channel. We later present a new system for MIMO underground mine communication by adopting the hybrid analog-digital structure to raise the achievable rate of the system. The construction of the precoding matrix requires the accurate channel estimation which is a rather challenging task for mm-Wave scenario. To achieve such objective, the channel estimation under the hardware impairments for hybrid beamforming based MIMO underground system is investigated when using real measurements of mm-Wave underground channel, and exploiting the space sparsity of the channel. Numerical results showed that, the transceiver hardware impairments have a deleterious impact on the achievable rate and channel estimation.

- In Chapter 5, we present a new wireless design of UAV architecture in which UAV operates as a beamforming relay in multi-user mm-Wave MIMO-OFDM system in order to improve the robustness to LOS blockage. Subsequently, a good link reliability between every BS and multiple ground users is maintained. Open challenges of user association in this context are highlighted, which sheds lights on the research direction. A distributed optimization algorithm which searches the best user-BS association, while maximizing the user data rate, is derived. Furthermore, in order to mitigate the interference impediment and overcome the propagation losses in such environments, hybrid beamforming scheme between the multiple BSs, the relay and the ground users is adopted, by merging the spatial processing and the amplify-and-forward (AF) operation. Finally, we provide some results to highlight the effect of the UAV altitude on the achievable rates and show the efficiency of the proposed system compared with the system without an UAV relay.

## 1.3 Thesis Organization

The rest of this thesis is organized as follows:

- Chapter 2 discusses the theoretical background related to the particular problems studied in this thesis, spanning the main differences between OFDM and FBMC systems, then the evolution of technology from MIMO to massive MIMO, and the resulting spectrum efficiency enhancement, followed by a summarize of the main advantages brought by mm-Wave frequencies, in particular in the 60 GHz band and beyond. Finally, mm-Wave relaying technologies are depicted along with open challenges addressed in this thesis.

- Chapter 3 presents the new practical architecture of encompassing hybrid beamfoming mm- Wave MIMO structure in underground communications, in which the hardware impairment effects have been considered in the transceiver processing. Furthermore, a 2-D geometrical channel model, which is based on one ring configuration, is presente to reproduce the underground channel behavior, by relying on measurements of this latter. The new communication architecture is tested based on the accuracy of this channel modeling.

- Chapter 4 presents the underground channel estimation. In particular, a novel channel estimation that is based on the compressive sensing theory is proposed for the mm-Wave underground channel in which a $2 \times 1$ STBC-FBMC system is deployed. We further adopt the hybrid analog-digital beamformer for MIMO underground mine communication to raise the achievable rate of the system. Then, the channel estimation operation performed under the hardware impairments accounted for in the hybrid beamforming- based MIMO underground system is investigated, when using the real measurements of the mm-Wave underground channel.

- Chapter 5 presents a new multi-user mm-Wave architecture in which UAV operates as a beamforming relay between multiple BSs and users to improve the robustness to blockage. The new approach is built upon, a distributed optimization algorithm which searches the best user-BS association, while maximizing the sum user data rate.

- Chapter 6 draws the final conclusions of this thesis by highlighting the main contributions to the considered problems and suggests future possible research extensions and directions based on the current work.

## Liste of Publications

The following is a list of research publications and patents that have been produced during this Ph.D. candidature.

**Journal Papers**

• W. Belaoura, K. Ghanem, M. Nedil, H. Bousbia-Salah, " Forward-backward processing for efficient underground channel estimation in 60 GHz MISO FBMC systems", In IET Electronics Letters, vol.55 , No. 2, pp. 92-94, 2018.

• W. Belaoura, K. Ghanem, MZ. Shakir, M. Nedil, H. Bousbia-Salah, " Achievable rate of hybrid precoding for hardware impaired MIMO underground mine channel", In IET Electronics Letters, vol.55 , No. 7, pp. 425-426, 2019.

**Conference Papers**

• W. Belaoura, K. Ghanem, H. Bousbia-Salah, " Effect of spatial correlation on the ergodic capacity for downlink massive MU-MIMO systems", In 6th IEEE International Conference on Systems and Control (ICSC), pp. 183-186, 2017.

• W. Belaoura, K. Ghanem, H. Bousbia-Salah, " Hybrid precoding for DL massive MU-MIMO systems with distributed antenna deployments", In 2017 IEEE International Symposium on Antennas and Propagation & USNC/URSI National Radio Science Meeting, pp. 1173-1174, 2017.

• W. Belaoura, K. Ghanem, M. Nedil, H. Bousbia-Salah, R. Labdaoui, " Compressive Sensing-Based Underground Channel Estimation Operating in Millimetter-Wave Band", In 2018 IEEE International Conference on Signal, Image, Vision and their Applications (SIVA), pp. 1-5, 2018.

• W. Belaoura, K. Ghanem, M. Nedil, H. Bousbia-Salah, " An Efficient FB-based Underground Channel Estimation for MIMO Mm-Wave Systems", In 2019 IEEE International Symposium on Antennas and USNC-USRI Radio Science Meeting AP-S/URSI, July 2019.

# CHAPTER 2

# MIMO WIRELESS COMMUNICATION BACKGROUND

## Contents

## 2.1 Introduction

As the digital world becomes increasingly intelligent, automated and ubiquitous, the flow of data becomes ever more vital. Mobile wireless networks are the data highways, and in a fully connected, intelligent digital world, they will need to connect everything from people, vehicles, and even robotic agents. 5G made a significant step towards developing a low latency access network, by providing new additional technologies. Yet, the rapid development of data-centric and automated processes may exceed even the capabilities of emerging 5G systems [3, 48]. This chapter, provides a literature review of some of the basic concepts of wireless communications to establish the concepts, schemes and architectures proposed in this thesis. It starts by a brief description of OFDM modulation as a commonly used technique in the current systems, followed by a technical description of FBMC waveform scheme. Then, an overview of MIMO wireless communications, covering the evolution of technology, from MIMO to massive MIMO, is depicted with an emphasis on the capacity enhancement which has followed. As the main technology trends behind the current wireless communication evolution have mainly aimed at boosting the transmission rate and system capacity using versatile methods, in the scope of this thesis, we have specifically turn our attention to mm-Wave MIMO systems, which offer a vast unused spectrum, in particular in 60 GHz band and beyond, and can double the SE of indoor underground environment. We then highlight even the advantages of using hybrid beamforming architecture for mm-Wave MIMO systems. Finally, we describe mm-Wave relaying technology, which helps resolving the LOS blockage issue in mm-Wave band and the main challenges encountered in this thesis.

## 2.2 Multi-Carrier Modulations

In wireless communications, fading channels are regarded as one of the main challenges faced by the development of next generation wireless systems, since they might seriously deteriorate the performance of the communication systems. It is now well-established that to combat the channel undesirable effects, the diversity technique has proved its efficiency by providing the receiver with multiple versions of the same signal [49]. The principle of diversity guarantees that the probability that multiple versions of a given signal are affected by a channel fading at the same time is quite low. This diversity could be performed either in space, time, or frequency domains.

### 2.2.1 OFDM Technique

An attractive and popular choice for transmission schemes overcoming the inter-symbol-interference (ISI) problem experienced over a frequency selective channel, is the so-called OFDM technique. In this approach the available spectrum is divided into several orthogonal narrowband subchannels, wherein each subchannel carries a low data rate stream as shown in Figure 2.1. The transmitted signal which bandwidth $B_s$ was greater than the coherence band of the channel $B_c$ before the application of OFDM, is transformed subsequently, into versions occupying a bandwidth which is at most equal to $B_c$. The corresponding subcarrier subchannels are then said to be flat. In conventional OFDM, the subcarriers are chosen to be orthogonal.

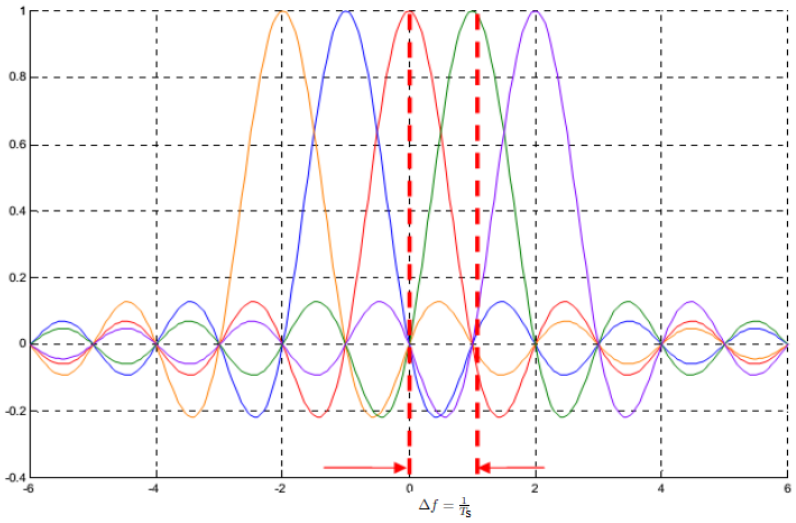


Figure 2.1: Orthogonal sub-carriers principle.

Orthogonality can be achieved by carefully selecting carrier spacing, to be equal to the reciprocal of the useful symbol period $\frac{1}{T_s}$, with $T_s$ being the period of the symbol. Hence, the orthogonality condition can be written as:

$$\frac{1}{T_s}\int_{t}^{t+T_s} e^{j2\pi f_p t} e^{j2\pi f_l t} dt = \begin{cases} 0 & si \quad p \neq l \\ 1 & \quad p = l \end{cases} \tag{2.1}$$

Due to the multipath fading channel and the variation of the channel during an OFDM block a loss of orthogonality may occur leading to inter-carrier interference (ICI), or to ISI. To prevent this, a cyclic prefix (CP) is inserted at the beginning of each OFDM symbol to be transmitted.

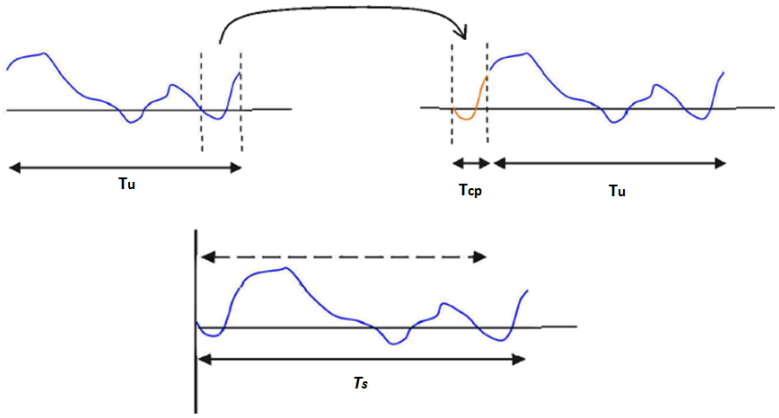


Figure 2.2: Insertion of prefix cyclic.

In generating the cyclic prefix, the last samples of an OFDM symbol are copied at its beginning, as illustrated in Figure 2.2. The duration $T_u$, in which the new generated information is sent, differs from the original period of the symbol $T_s$, by the duration of this CP $T_{cp}$, as expressed by the following equality:

$$T_s = T_u + T_{cp} \tag{2.2}$$

In order to overcome the ISI almost completely, the CP interval should be larger or equal to the maximum path delay.

Despite the many advantages of OFDM approach, relying on a CP-inserted transmission induces a reduction in the SE. Keeping in mind that a considerable amount of data rate is required in 5G systems and beyond, to cope with the users heteregenous needs and the spectrum-greedy future applications, several research initiatives have been conducted to design new waveforms which meet these requirements, such as FBMC technique.

### 2.2.2 FBMC Technique

FBMC systems are currently being considered as a prevalent candidate for replacing the long established OFDM in 4G LTE systems, since each subcarrier symbol is shaped by time-frequency well-localized prototype filters e.g. PHYDYAS filter [50]. The prototype filter provides FBMC with the ability of carrying a flexible spectrum shaping, along with a major increase in SE and robustness against time and frequency dispersive channels, which are features of fundamental importance in the envisaged

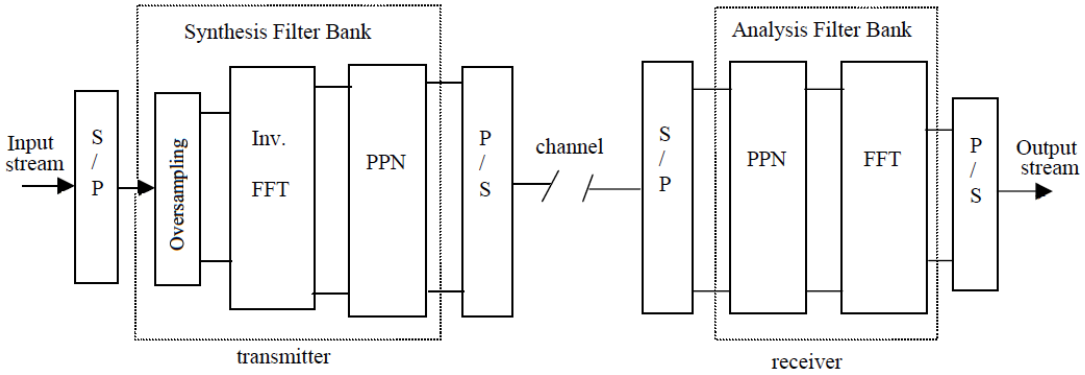


Figure 2.3: Block diagram of the FBMC transceiver.

networks, without the use of CP, unlike conventional OFDM [51, 52]. Depending on the modulation type, FBMC systems can be divided into two main categories: FBMC-offset quadrature amplitude modulation (FBMC-OQAM) and FBMC-QAM. The FBMC-OQAM introduced in [53, 54] adopt OQAM signaling with a half-symbol period shift, and utilize a single prototype filter that satisfies only real orthogonality conditions. The general structure of FBMC system is depicted in Figure 2.3, where the transmitter side is enriched with a synthesis filter bank (SFB) and the receiver with an analysis filter bank (AFB), while the structure of the FFT is the same as the one in OFDM technique. The discrete time transmit signal is given as:

$$\mathcal{S}(i) = \sum_{k=1}^{K} \sum_{n=-\infty}^{\infty} x_{k,n} g_{k,n}(i) \tag{2.3}$$

where $K$ is the number of subcarriers, $(k, n)$ refers to the $k^{th}$ subcarrier and the $n^{th}$ FBMC symbol, $x_{k,n}$ is the corresponding real OQAM symbol, and $g_{k,n}(i)$ represents the time and frequency shifted version of the prototype function $g(i)$ , which can be expressed as:

$$g_{k,n}(i) = g[i - nK] e^{j\frac{2\pi}{K}(k)(i - \frac{L_f - 1}{2})} \tag{2.4}$$

with $g(i)$ being the employed prototype filter impulse response with length $L_f$. After passing through a channel $h$, the received signal can be written as:

$$\mathrm{y}(i) = \mathcal{S}(i)h + n(i); \tag{2.5}$$

where $n(i)$ is the Gaussian noise with zero mean and variance $\sigma^2$. The essential difference between FBMC and OFDM resides in the frequency selectivity. This is illustrated

in Figure. 2.4, which shows the frequency responses, around a particular sub-carrier, in both cases. OFDM exhibits large ripples in the frequency domain, which imposes the orthogonality constraint between all the sub-carriers. On the contrary, the filter bank frequency response has a negligible amplitude beyond the center frequency of the adjacent sub-carriers. In fact, the filter bank divides the transmission channel of the system into a set of sub-channels, where any sub-channel overlaps with its immediate neighbor only.

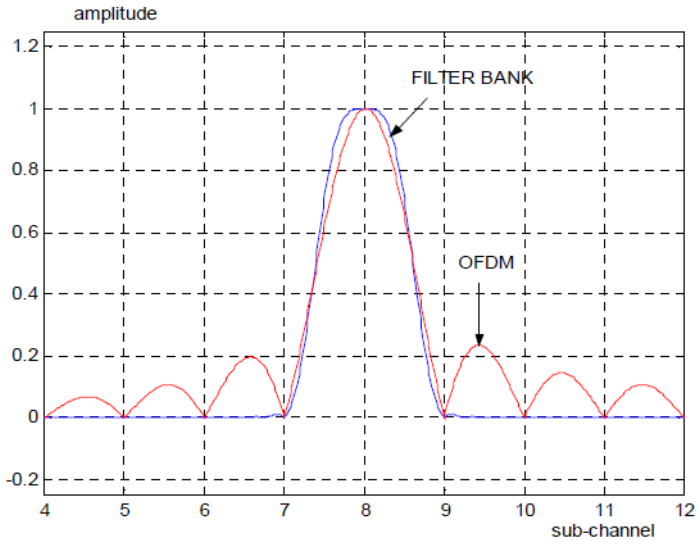


Figure 2.4: Comparison of the frequency responses of FBMC and OFDM.

The FBMC/OQAM technique suffers however from pure imaginary intrinsic interference caused by neighboring symbols. This leads to additional challenges, especially for MIMO system design and channel estimation [55–57]. To maintain compatibility, a new FBMC scheme that supports QAM signaling was proposed in [58], where dual prototype filters were used to transmit the QAM symbols, without CP, as a way to achieve the orthogonality condition between adjacent sub-carriers, thus improving the performance of the system. This system will be studied in details in Chapter 3.

## 2.3 From MIMO to Massive MIMO

In conventional wireless communications, a single antenna is used at the transmitter, and another single antenna is used at the receiver, also known as single-input single-output (SISO) system. In realistic scenarios, this gives rise to an inefficiency

in combatting multi-path effects, which results in severe degradation of the quality of the transmitted signal at the receiver [2]. By contrast to SISO architecture, MIMO alternative takes advantage of the multipath behavior by using multiple antennas at both the transmitter and the receiver. The usage of multiple antennas can be classified into two main categories: spatial diversity and spatial multiplexing.

### 2.3.1 Spatial Diversity Technique

Exploiting multiple antennas at the transmitter and/or receiver provides substantial benefits in both increasing system capacity and immunity to deep fading in wireless channels by using space-time coding. In 1998, Alamouti [49] introduced the first spatio-temporal code (STC), for two transmit antennas, which was then generalized by Tarokh et al. to systems with more than two transmit antennas. Its concept is based on the idea of adding redundancy to the transmitted data in order to increase the spatial diversity, hence avoiding a critical effect of the fading of the channel. When using space time bloc code (STBC) processing, the data stream is encoded in blocks before the transmission. As shown in Figure 2.5, the symbols $X_1$ and $X_2$ are simultaneously sent by the two transmit antennas in time slot one. Then, in time slot two, the signals $-X_2^*$ and $X_1^*$ are sent from antennas one and two, respectively, where $X_i^*$ is the complex conjugate of $X_i$. Therefore, the transmitted codeword is:

$$\begin{bmatrix} -X_2^* & X_1 \\ X_1^* & X_2 \end{bmatrix} \tag{2.6}$$

Let the path gains from transmit antennas one and two be $H_1$ and $H_2$. The received signals $r_1$ and $r_2$ in the two time slots, respectively, are given as:

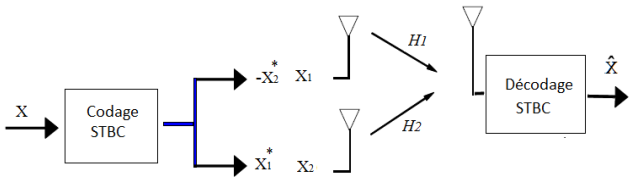


Figure 2.5: STBC principe.

$$\begin{aligned} r_1 &= X_1H_1 + X_2H_2 + n_1 \\ r_2 &= -X_2^*H_1 + X_1^*H_2 + n_2 \end{aligned} \tag{2.7}$$

where $n_1$ and $n_2$ are Gaussian noise signals at the unique receive antenna at the two time slots. For a coherent detection scheme, where the receiver knows the channel gains $H_1$ and $H_2$, the combining scheme builds the following two signals to estimate the transmitted signals:

$$\begin{aligned} \tilde{X}_1 &= H_1^* r_1 + H_2 r_2^* \\ \tilde{X}_2 &= H_2^* r_1 - H_1 r_2^* \end{aligned} \tag{2.8}$$

### 2.3.2 MIMO Systems

One another purpose of using multiple antennas at the transmitter and the receiver is to achieve throughput gains, wherein the transmitter spatially multiplexes parallel streams of data over the same time-frequency resources. Such MIMO systems have already been used in LTE and LTE-Advanced networks. Figure 2.6 illustrates a MIMO system with $N_t$ antennas at the transmitter and $N_r$ at the receiver in which the received signal can be given as:

$$\mathbf{r} = \mathbf{H}\mathbf{x} + \mathbf{n}, \tag{2.9}$$

where $\mathbf{x}$ is the $C^{N_t \times 1}$ transmitted signal vector, $\mathbf{H}$ is the $N_r \times N_t$ channel matrix between the transmitter and the receiver, and $\mathbf{n} \sim CN(0, \sigma^2)$ is the additive white Gaussian noise (AWGN) vector, with $\sigma^2$ standing for the element noise variance. For a given link, the capacity, which is a reference metric for the throughput, refers to the maximum amount of information in bits/s/Hz that can be transmitted on a propagation channel. The general capacity expression normalized to the bandwidth is given as [59] :

$$C = \log_2\{\det(\mathbf{I}_{N_r} + \frac{\gamma}{N_t}\mathbf{H}\mathbf{H}^H)\} \tag{2.10}$$

where $\mathbf{I}_{N_r}$ is the identity matrix of size $N_r$, and $\gamma$ is the the signal-to-noise ratio (SNR). It is agreed upon by now that the capacity of a MIMO channel increases linearly with the minimum number of transmit and receive antennas.

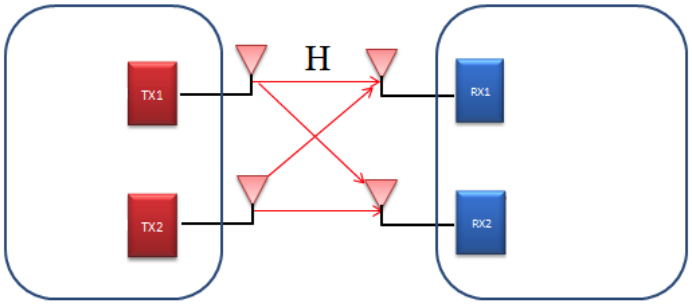


Figure 2.6: MIMO transmission.

### 2.3.3 What is Massive MIMO

By definition, massive MIMO (also known as large scale antennas systems) is a form of multi-user MIMO technology, where the base station (BS) is equipped with an excessively large number of antennas when compared to the number of users in the system. This technology was introduced for the first time by Thomas Marzetta in 2010 [11]. As illustrated in Figure 2.7, the idea of massive MIMO is to employ a huge number of antennas at the BS simultaneously serving many ten of users through spatial multiplexing mean. The purpose of this technology is to scale up the benefits of conventional MIMO systems and act as an enabler for more energy and spectral efficient, secure and robust systems [9]. These features allow massive MIMO to be one of the most potential technologies for the 5G wireless communications. Some main characteristics of Massive MIMO are summarized below:

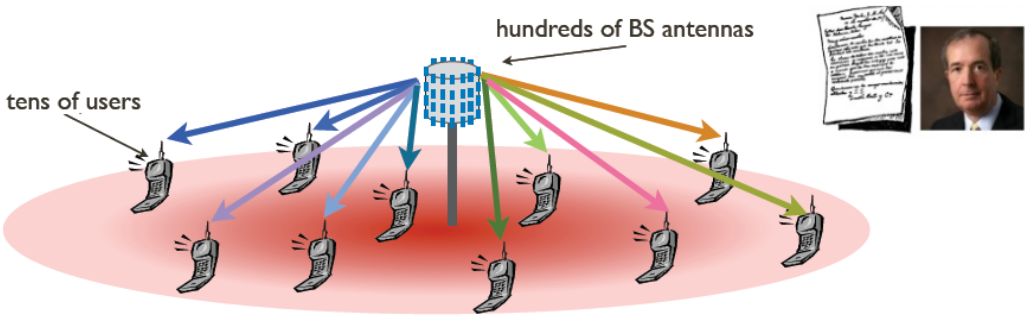


Figure 2.7: Massive MIMO system

- Time-division duplexing (TDD) operation: to fully exploit the potential of the large number of antennas, BS needs to have an accurate CSI. With frequency-division duplexing (FDD) mode, the channel estimation overhead depends on

the number of antennas. By contrast, with TDD mode, the channel estimation overhead is independent of antennas. In massive MIMO configuration, TDD operation is favorable thanks to its channel reciprocity in downlink (DL) and uplink (UL). As a result, adding more antennas does not affect the resources needed for the estimation.

- Linear processing: since the number of BS antennas and the number of users are large, the signal processing at the terminal ends must deal with large dimensional matrices/vectors. Thus, simple signal processing is preferable. In Massive MIMO, linear combing schemes in the UL and linear precoding schemes in the DL are nearly optimal.

- Deploying a large number of antennas at the BS results in an interesting propagation scenario, known as favourable propagation, where the channel becomes near-deterministic because the radio links between the BS and the users become nearly orthogonal to each other [60]. This in turn is because the effects of small-scale fading tend to disappear asymptotically when the number of antennas at the BS is increased unboundedly [61].

### 2.3.4 System Model and Ergodic Capacity

We consider one BS equipped with $M$ antennas and $K$ single-antenna mobile users, and assume that the receiver has a perfect CSI. The received signal at all users can be written as:

$$\mathbf{y} = \mathbf{H}\mathbf{x} + \mathbf{w}, \tag{2.11}$$

where $\mathbf{x} \in C^{M\times 1}$ is the transmitted signal to all users, and $\mathbf{w} \sim CN(0, \sigma^2)$ represents the AWGN at the receiver, where $\sigma^2$ stands for the noise variance, and $\mathbf{H} \in C^{K\times M}$ is the channel matrix from the BS to the users, and is modeled by Rayleigh distribution. In this case, the DL capacity of the MIMO channel is formulated as:

$$C = E\{\log_2 \det(\mathbf{I} + \frac{\mathrm{SNR}}{M}\mathbf{H}^H\mathbf{H})\} \quad bit/s/Hz \tag{2.12}$$

where $E\{.\}$ denotes the expectation operator and $\mathbf{I} \in C^{K\times K}$ is identity matrix.

## 2.4 Mm-Wave Systems

As the electromagnetic spectrum with favourable communication properties below 6 GHz is almost completely expended, it is evident that with the same spectral setting, the future demand for mobile data traffic will not be met. The attention of radio system designers and researchers has moved towards high frequency bands, such as mm- Waves frequency bands, to guarantee remarkably better performances in terms of capacity, as well as a potential unlicensed exploitation of such frequency band [13,62]. Thanks to the short wavelength of mmWave radio, many more critically spaced antennas can be packed into the limited dimensions of mm-Wave transceivers [63]. The short wavelength typically limits the use of mm-Wave communication systems to short-range communications, particularly in niche applications such as in tunnel environments including highway, railway and underground mine. However it has appeared that, using high directive antennas increases the coverage in mm-Wave frequency bands and increases their application to longer range outdoor links [64,65].

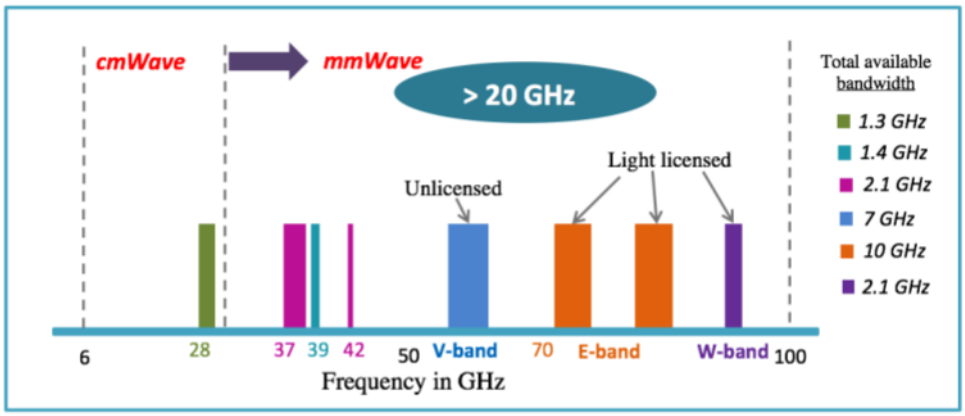


Figure 2.8: Available bandwidth in the mm-Wave spectrum

### 2.4.1 Mm-Wave Underground Systems

In the underground mine environment, the use of 60 GHz band is important due to its 5 mm wavelength, large bandwidth, and the density of antennas intergration. However relative to the low-band counterparts, the mm-Wave signals experiences more severe path loss, a smaller number of multipath components (MPCs), and a higher sensitivity to LOS blockage, which drastically limits the communication distance and makes the communication quality unpredictable [13, 66]. On the other hand, the

unique propagation environment of underground mines, such as long limited space, wall surface roughness, and the boundedness of walls, result in propagation characteristics of signals that are quite different from those of conventional indoor scenarios. As a consequence, when working in mm-Wave bands, the propagation attributes and the presence of channel impairments should be carefully considered. Let us summarize these so-mentioned major mm-Wave channel characteristics herein:

- Path loss: the path loss is a relevant parameter for characterizing the mm-Wave wireless channel, depending on the carrier frequency $f_c$. Increasing this latter will reduce the antenna size, since the effective aperture of the antenna scales by a factor of $\frac{\lambda}{4\pi}$, while the free space path loss grows with $f_c$. The natural way to combat the path loss is by proportionally increasing the antenna aperture, which can be achieved in practice by using MIMO antenna arrays.

- Blockage: mm-Wave signals experience a prismatic propagation and suffer less diffraction than the microwave signals, making them much more susceptible to blockages. This will result in a nearly bimodal channel according to the lack and existence of LOS. Thus, the connection set will shift from being usable to unusable, based on the occurrence of blockages.

- Atmospheric and rain absorption: A major impediment to mm-Wave communications is the attenuations due to rain, foliage, and atmospheric absorption, which are of the order of 15 dB/km within the 60 GHz band.

In order to provide a complete characterization of the mm-Wave channel in underground mine environments, measurement campaigns are carried out by using the appropriate setup, which devices are tuned to communication at these bands [16,24,67].

### 2.4.2 Experiment Mining Setup

The first work on mm-Wave propagation within underground channels was reported in [68], where the measurements were carried out in a real underground mine operated by the Canadian Center for Minerals and Energy Technology (CANMET), and located at 40 m deep underground level. The gallery stretches over a length of 75 m with both a width and a height of approximately 5 m. A map of the underground gallery is shown in Figure 2.9. The setup system is mainly composed of two microstrip patch antennas distant by a wavelength, i.e 5 mm, from the center to center and which are placed on opposite sides of the gallery. During the measurements, the


Figure 2.9: Underground gallery scenarios.

transmitter was maintained fixed, while the receiver was moved at different positions along the gallery, from 1m up to 10m apart from the transmitter, with steps of 1 m. Further details on channel measurements are available in [68]. For each position, the complex frequency-domain transfer function is:

$$G(f) = A(f)e^{j\theta(f)} \tag{2.13}$$

where $A(f)$, $\theta(f)$ are the measured magnitude and phase responses at a particular frequency, respectively. The sub-channels are then used to generate the measured MIMO transfer function for each position over the mm-Wave bandwidth, an the IFFT is subsequently applied. Thus, the time-domain channel impulse response (CIR) could be expressed as follows:

$$H(\tau) = \sum_{f=1}^{F} G(f)e^{j2\pi\tau f/F} \tag{2.14}$$

where $F$ is the number of frequency subcarriers. As shown in Figure 2.10, the obtaind mm-Wave underground channel is sparse in time domain, because eventhough the delay spread could be very large, the number of significant paths is very small.

The underground mine propagation channel is complicated, as different structures cause different propagation phenomena, like reflection, refraction, diffraction, and scattering, which result in multipath propagation. The wireless channel can be

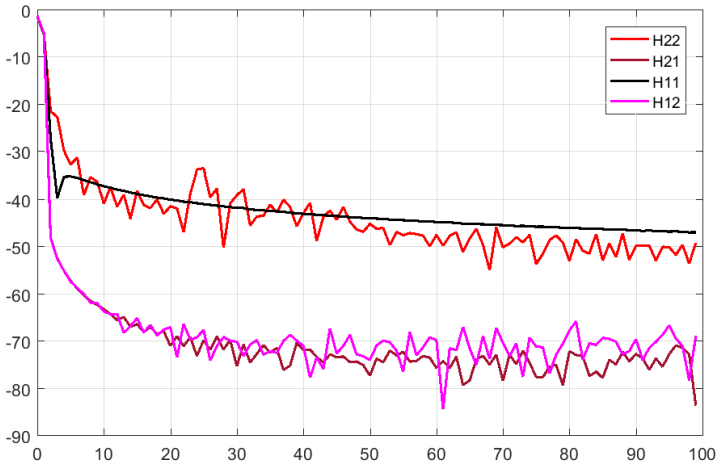


Figure 2.10: Illustration of the power delay profile of mm-Wave underground channel in time domain.

described by its impulse response, or by its power delay profile (PDP), where for any fixed location between transmitter and receiver, the overall average of the magnitude squared of the impulse response is given by:

$$PDP(\tau) = \|H(\tau)\|^2 \tag{2.15}$$

The channel should be sparse in time domain means that $H$ can be represented using only a small number of samples $S_i \ll L$ as follows [69,70]:

$$\|H\|_0 = S_i \ll L, \tag{2.16}$$

where $S_i$ is the sparsity level and $\|.\|_0$ denotes the $l_0$ operation which counts the number of non zero coefficient, where their positions are unknown.

### 2.4.3 Mm-Wave Massive MIMO Systems

As mentioned earlier, the mm-Wave communications are characterized by a higher path-loss and a stronger sensitivity to blockage than the micro-Wave communications. To face these impairments, the short wavelengths of mm-Wave frequency bands could be exploited to embed a large number of antenna elements at both transceiver ends, thus enabling large array structures which allow to provide high beamforming gains and enhance the system's SE [71]. However, the use of high-frequency bands, opens various technological challenges related to high path loss and multiple access. Thus,

an additional system improvement needs to be achieved, in order to be suitable for adoption at the next generation wireless communications.

Massive MIMO systems combined with beamforming antenna array technologies are expected to play a key role in next-generation wireless communication systems [72]. The fundamental principle of beamforming is to transmit identical information on each element of the array, while varying the amplitude and/or the phase of the signal at each antenna. When implementing antenna arrays in hardware, several structures of beamforming can be used. However, three different cases could be differentiated:

#### 2.4.3.1 Fully Digital Beamforming Structure

In a conventional MIMO system, a full digital architecture is used, where in each antenna usually requires one dedicated RF chain, including high-resolution digital to analog converters (DACs) [73]. As a result, hardware complexity and energy consumption for digital baseband beamformers become significant issues, as the number of antennas becomes huge. Because of the huge number of employed antenna elements, the full digital beamforming technique can't be deployed in mm-Wave massive MIMO systems.

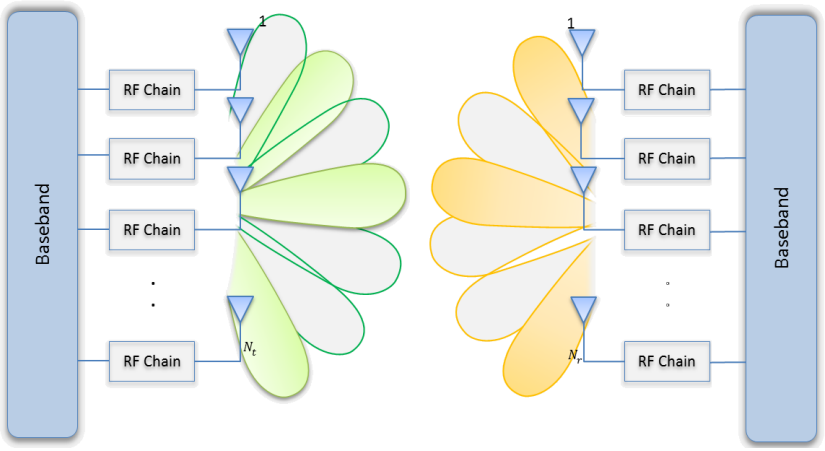


Figure 2.11: Conventional MIMO systems using digital beamforming design.

#### 2.4.3.2 Analog-only Beamforming Design

The analog beamforming was widely used in the past, because of the implementation simplicity of the associated approaches to improve the directivity gain in mm-Wave

systems. In analog beamforming, phase shifts are applied to each antenna element of the array in order to steer the beam towards a certain direction [74,75]. However, since only the phases of the signals are controlled, the performance loss of analog beamforming technique is obvious. More importantly, analog beamforming can only support a single-stream transmission, and could hardly be extended to multi-stream or multi-user scenarios. An example of such an architecture is depicted in Figure 2.12. By adopting the pure LOS channel, the analog beamformer $\mathbf{F}_{\mathrm{RF}}$ can be expressed as [73]:

$$\mathbf{F}_{\mathrm{RF}} = \frac{1}{\sqrt{N_t}}[1, e^{j2\pi d \sin(\theta)/\lambda}, ..., e^{j2\pi(N_t-1)d\sin(\theta)/\lambda}]^T \tag{2.17}$$

where $N_t$ is the number of antennas at the transmitter, $\theta$ is the angle of departure (AoD), which assumed to be uniformly distributed $\in [0, 2\pi]$, $d$ represents the inter-element antenna spacing, while $\lambda$ represents the wavelength of the signal.

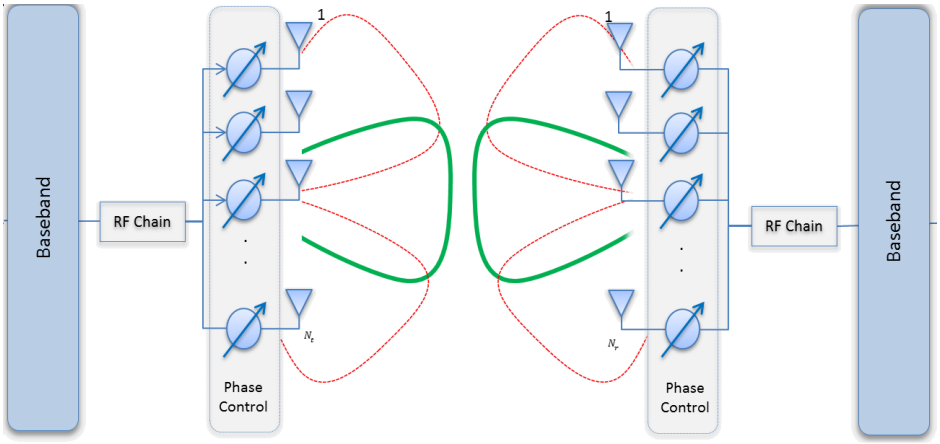


Figure 2.12: Mm-Wave MIMO systems using analog-only beamforming design.

#### 2.4.3.3 Hybrid Beamforming: Basic Concepts

Hybrid beamforming architectures is a promising candidate solution that overcome the limitations of pure analog and digital beamforming architectures, as they incorporate the advantages of both [31]. These schemes improve the beamforming gain and enhance the MIMO communication benefits, by enabling multiple stream beamforming. The principal design criterion is limiting the number of RF chains and make it less than the number of antennas is the system, thus reducing the complexity compared to fully digital solutions. This actually allows more freedom than conventional

analog beamforming by dividing the beamforming process between the analog and the digital domains. In this hybrid solution, the digital signal processing can be realized at the baseband frequency using microprocessors whereas, the analog signal processing can be enabled at the RF frequency by employing low cost phase shifters. An advantage of the hybrid approach is that the digital beamforming can compensate for the lack of precision in the analog domain, for e.g., it can cancel residual multi-stream interference, thus achieving higher beamforming gains. For all these reasons, deploying mm-Wave massive MIMO systems with limited number of RF chains in the hybrid analog-digital architecture has recently received a significant attention.

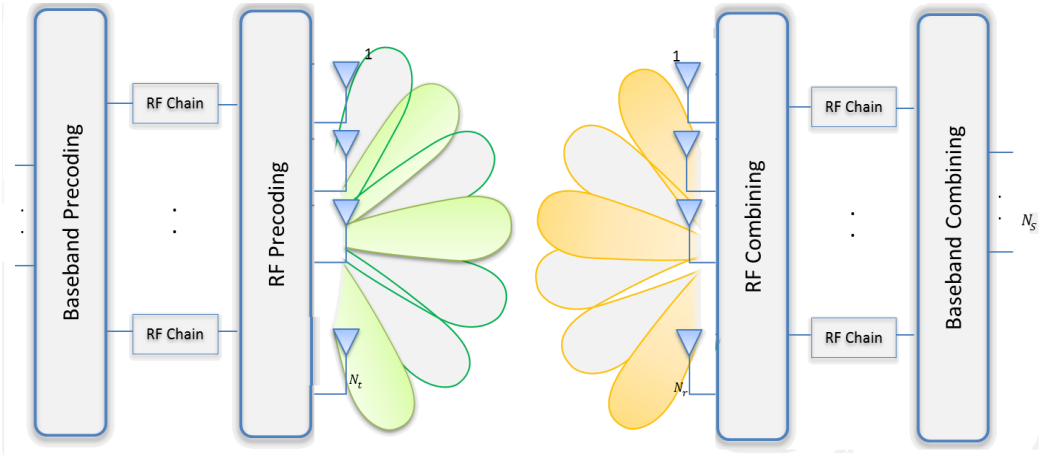


Figure 2.13: Hybrid beamforming design.

By making more than one digital RF chain available for beamforming, it is possible to utilize channels with multiple paths, by communicating different spatial streams at the same time, and by relying on the physical fact that mm-Wave signals are easily blocked, it is highly desirable to have multiple spatial streams available for transmission at any time. For this reason, hybrid architectures are typically favored over analog-only beamforming design.

## 2.5 Mm-Wave Relaying Technologies

The availability of bands in the range of 30-300 GHz makes mm-Wave a lucrative prospect in the design of 5G networks [76, 77]. However, one distinct disadvantage of mm-Wave communications is that the transmitted signals can be easily blocked by LOS obstacles like buildings, concrete walls, vehicles, trees, etc ..., which results in substantial performance losses [36]. To cope with the open research problems, it

is agreed upon nowadays that, in addition to using massive MIMO antennas at the transceiver to compensate the mm-Wave drawbacks, the cooperative transmission in relay networks is another way to enhance system throughput, in which BSs can transmit to different users [37]. This strategy improves the received power, reduces path loss, enables long-distance mm-Wave communications, and expands their coverage.

### 2.5.1 Ground Relays

Cooperative relaying transmission is an essential strategy for enabling long-distance mm-Wave communications and improving the level of the received power. With the help of a relay, the signals can be transmitted over a longer distance, and it is likely that the channel between the source and relay and (relay and destination) is LOS allowing to achieve a better system performance than the scenario where the relay is not adopted and in which the channel between the source and destination is most probably.

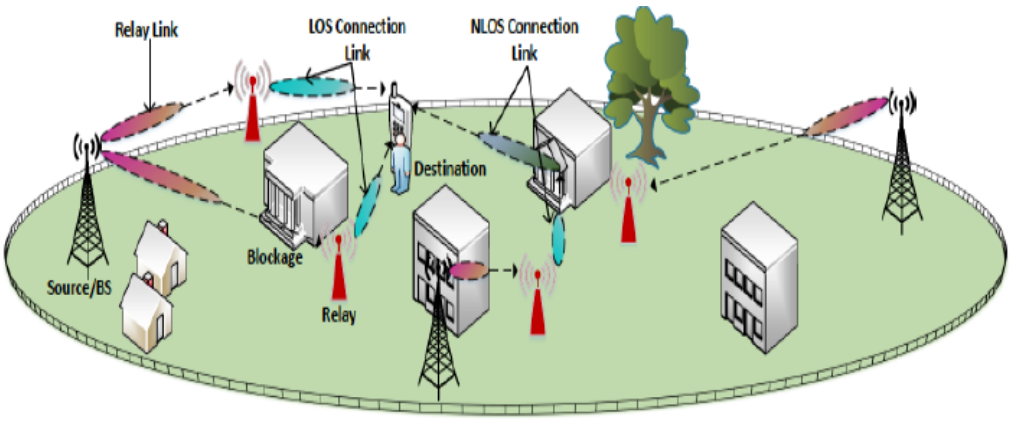


Figure 2.14: An illustration of an outdoor mm-Wave network aided by relays.

In some environments (hills, modern urban areas,...), the effect of shadowing and blockages might be critical, and the ground relay nodes might become unable to support the transmission from the source to the destination because they are constained by the nature of the covered land and their positions relative to it. A possible solution, which has started emerging in the research, is to circumvent the blockages by the aid of an aerial relay.

### 2.5.2 Aerial UAV Relay

Due to the impracticality of establishing long LoS links, especially in dense urban environments, UAV based relays in mm-Wave communications are able to provide on-the-fly communications and establish reliable LOS links between the ground stations. This interest is motivated by their avoidance of the classical wireless communication scatterers which degrade the communications quality, their coverage and supervision of wide areas, and their targeting of potential applications such as police patrolling, surveillance, and as communication relays [40]. In this perspective, while opting for the conventional ground relays allows a long term operation thanks to the stable power supply, at the expense of a penalizing NLOS communication mode, aerial relay assisted communications are a viable solution to mitigate the limited performance resulting from the blockage effect, and exploit the relay flexibility, mobility, adaptive altitude and low cost in enabling long-range mm-Wave communications [41]. With the rapid development of UAV, mobile relays have become possible in real-world scenarios, which can mitigate some of the afore-mentioned limitations of mm-Wave communications, offer a direct and uncrowded link with the ground users, and improve the connectivity for wide-range area networks [42].

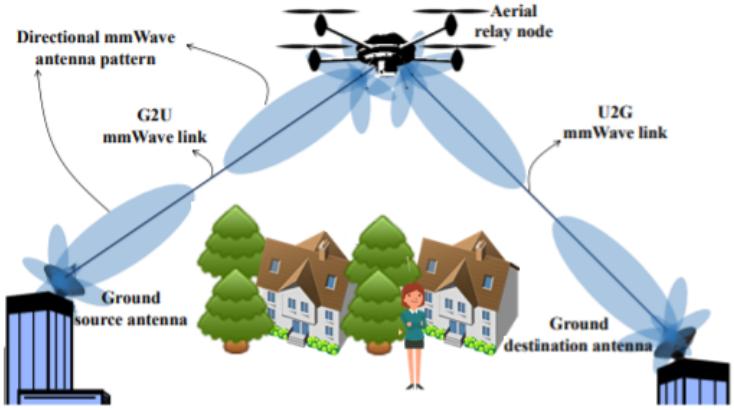


Figure 2.15: UAV relay.

The integration of UAVs relays and mm-Wave wireless systems has been recently proposed to provide high data rate aerial links for next generation wireless networks. Despite the manifold benefits, currently establishing UAV as the mobile relays is quite challenging from these point of views:

- 3D placement: UAVs need to be deployed by considering the constraints of a 3D system, which therefore makes their deployment more complicated, as

compared to that of the terrestrial relays. In this regard, the altitude of the UAVs plays a vital role in establishing a LoS communication link with the terrestrial network and should therefore be optimized accordingly.

- Channel modeling: UAV-based mm-Wave communication is different from terrestrial communication in various aspects, which essentially necessitates a statistical RF propagation model for the UAV communication channel.

- Design of a multi-hop aerial network: as mentioned earlier, UAVs can form a multihop aerial network for coverage extension or backhaul connectivity for the ground BSs. However, a major challenge in that scope is the formation of such an aerial network. In particular, the UAVs need to form the A2A and A2G link while taking into account the delay incurred over the formed multihop links.

- Antenna design: Current network deployments assume that communication occurs within a 2D plane, and must support human devices (with low mobility) and ground vehicles (with potentially high mobility). Nevertheless, aerial networks consist of Air-to-Ground (A2G) and Air-to-Air (A2A) links and require data to be delivered at different altitudes and orientation angles. As such, directed antenna radiation characteristics are more likely to have high impact on the performance of 3D connectivity.

## 2.6 Mm-Wave Massive MIMO Challenges

While mm-Wave massive MIMO configuration is able to achieve terrific benefits, the employment of large number of antennas unveils a series of challenges, which are addressed in this section. Generally, there are plenty of implementation challenges for such technology, such as low-cost hardware elements, hybrid beamforming strategies, channel estimation algorithms, and user association design. In particular, our main focus will reside on the channel estimation challenges, hardware impairments and user association design [7, 40].

- Channel estimation: the most immediate challenge faced by mm-Wave MIMO channel estimation comes from signal propagation losses inherent in this frequency range and the large number of antennas. Because of this, the omnidirectional transmission of any pilot signal results in very low SNRs, which ultimately

leads to less accurate channel estimation [12]. To increase the SNR it is necessary to employ proper beamforming during channel estimation. Moreover, the exploitation of the sparsity of mm-Wave channels allows to reduce the overhead and lower the estimation complexity. Hence, instead of estimating all the entries of the channel matrix, one would estimate only the angle of the depart (AoDs) and AoAs of the dominant paths and the corresponding path gains by using compessive sensing concepts.

- Hardware impairments: Another challenge in mm-Wave systems is the presence of hardware imperfections which impose a huge challenge on 5G network deployment, owing to the degraded system performance emanating from severe signal contamination. This problem is considered as the biggest limitation when considering the deployment of large antenna arrays. For example, practical transceiver hardware is impaired by phase noise, limited phase shifters resolution, non-linear power amplifiers, I/Q imbalance, and limited ADC/DAC resolution. Therefore, RF impairments form a key design challenge for developing new configurations in upcoming 5G wireless communication, as these imperfections dominate the performance of the overall system [78].

- User association: the unique characteristics of mm-Wave bands, making it necessary for the mm-Wave cellular network to be dense, is that they are mainly interference-limited. In particular, the aforementioned mm-Wave channel characteristics, have a significant effect on cell coverage, which indicates that the attainable throughput of mm-Wave networks is highly dependent on the user association, i.e., the process that associates a user with a particular serving BS. Hence, it is urgently needed to desig new association rules for dense mm-Wave networks [76,79].

## 2.7 Conclusion

In this chapter, we have reviewed the basic principles and technologies investigated in this thesis such as, the FBMC modulation and its advantages, some theoretical background behind MIMO wireless communication systems, covering the evolution of technology from MIMO to massive MIMO, and the capacity achieved by multi-antenna channels. Subsequently, the emphasis was put on mm-Wave MIMO systems, in particular underground MIMO communications at 60 GHz based on real measure-

ments. Furthermore, an up-to-date overview of mm-Wave based hybrid beamforming was discussed to justify the proposition of hybrid beamforming architecture as an alternative to conventional analog only beamforming MIMO schemes. Stating all these concepts, the operation principle of this novel communication scheme will be discussed in next chapter. Finally, we present the mm-Wave relaying technologies and discuss some important challenges the mm-Wave MIMO systems have to overcome.

# CHAPTER 3

# HYBRID BEAMFORMING FOR MIMO UNDERGROUND SYSTEM

## Contents

## 3.1 Introduction

Future underground mining environment will require various high data rates applications, such as video surveillance and onsite real-time high-data rate connectivity targeted for mining operation information and safety purposes. Millimiter-Wave (Mm-Wave) technology is intended for multi-Gb/s applications and has attracted a significant attention, more particularly for confined environments, such as the operation within underground mine galleries. Interestingly, scaling up the number of antennas, enhances the spectral efficiency and mitigates the effects of the channel fading. Moreover, because of the quite low wavelength, designing large scale antenna systems at high frequencies induces a reasonnable hardware size, but this may come at the cost of an increased hardware complexity. In this context, hybrid beamforming is considered as a well-accepted approach to enhance the achievable rate in the adverse mm-Wave MIMO underground channels, with a low hardware complexity. Motivated by the above discussion, in this chapter, a new architecture for MIMO underground communications encompassing a hybrid beamforming structure, is presented. The main contributions of this chapter can be summarized as follows:

- First, we describe the system model of the proposed large MIMO architecture for underground communications, followed by the MIMO model alternative, which takes into account the impairments and their impact on the transmitted and received signals, thereby paving the way to a more realistic evaluation of the benefits of 5G systems. The proposed architecture aims at enhancing the achievable rate of underground communications by adopting the MIMO hybrid beamforming processing for such stressed environment, while reducing the impingement of hardware transceivers practical defects on it.

- Second, to effectively design the communication systems, fundamental understanding of the propagation characteristics expressed through channel models is required, a newly 2-D geometrical scattering one ring-based model on real channel measurements is proposed to capture the spatial representation of the underground channel, on which the resulting architecture is tested.

- By modeling the residual impairments as an additional distortion noise, the expression for the data rate of both hybrid beamforming and analog RF beamforming in mm-Wave underground MIMO channels are derived. The performance of the proposed MIMO underground-based hybrid beamforming architecture is evaluted and compared with similar structures incorporating solely analog and

digital beamforming, through Monte Carlo simulations. Results demonstrate that the performance of the presented architecture is indeed viable, and is superior to that of analog-only counterpart. Furthermore, it is close to the one of the optimal digital beamforming.

## 3.2 Mm-Wave MIMO Underground System

In this section, the expression of the received signal with the proposed hardware impaired MIMO underground system incorporating hybrid beamforming for the downlink scenario depicted in Figure 3.2, is extracted. As such, we first consider the ideal scenario of MIMO transceivers with no hardware imperfections and retain it as a benchmark to the system with hardware impairments. We assume that the system operates in TDD mode and that the CSI is available at both the transmitter and the receiver sides.

### 3.2.1 Underground System Model

Let us consider a hybrid beamforming architecture deployed in a mm-Wave MIMO underground system, wherein the transmitter is equipped with $N_t$ antennas and $N_{\text{RF}}$ RF chains, and the receiver is equipped with $N_r$ antennas and $N_{\text{RF}}$ RF chains, as shown in Figure 3.1. We assume that the transmitter and the receiver communicate via $N_s$ data streams, such that $N_s \leq N_{\text{RF}} \leq N_t$ and $N_s \leq N_{\text{RF}} \leq N_r$.

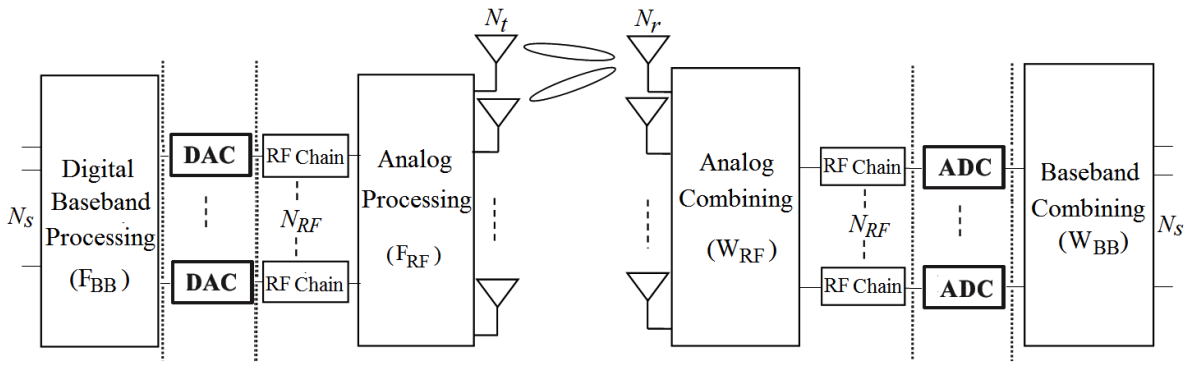


Figure 3.1: Transceiver structure of hybrid mm-Wave MIMO underground system.

In this setup, the transmitter is assumed to apply two consecutive beamforming

operations, namely $\mathbf{F}_{\mathrm{BB}} \in \mathbb{C}^{N_{\mathrm{RF}} \times N_s}$ and $\mathbf{F}_{\mathrm{RF}} \in \mathbb{C}^{N_t \times N_{\mathrm{RF}}}$, where the former refers to the digital baseband beamformer, whilst the latter denotes the analog counterpart. Hence, the transmitted signal can be given as:

$$\mathbf{x} = \mathbf{F}_{\mathrm{RF}}\mathbf{F}_{\mathrm{BB}}\mathbf{s} \tag{3.1}$$

where $\mathbf{F}_{\mathrm{T}} = \mathbf{F}_{\mathrm{RF}}\mathbf{F}_{\mathrm{BB}} \in \mathbb{C}^{N_t \times N_s}$ is the hybrid beamforming matrix, $\mathbf{s} \in \mathbb{C}^{N_s \times 1}$ is the transmitted symbols vector, where $\mathbb{E}[\mathbf{s}\mathbf{s}^H] = \frac{P_s}{N_s}\mathbf{I}_{N_s}$, with $P_s$ being the average total transmit power, and the transmit covariance matrix defined as $\mathbf{Q} = \mathbb{E}[\mathbf{x}\mathbf{x}^H]$. Since $\mathbf{F}_{\mathrm{RF}}$ is implemented using analog phase shifters, its entries are of a constant modulus. We normalize these entries to satisfy the condition $\left|\mathbf{F}_{\mathrm{RF}}\right|^2 = N_t^{-1}$. We adopt the underground mine channel model in which the receiver observes the received signal as:

$$\mathbf{r} = \mathbf{H}\mathbf{F}_{\mathrm{T}}\mathbf{s} + \mathbf{n}, \tag{3.2}$$

where $\mathbf{H} \in \mathbb{C}^{N_r \times N_t}$ is the underground mine channel at the mm-Wave band emulated using the 2-D geometrical model and which will be explained in more details in the next section, while $\mathbf{n} \sim \mathcal{N}(0, \sigma^2 I_{N_r})$ represents the additive white Gaussian noise (AWGN) vector at the receiver, with $I_{N_r}$ standing for the $N_r \times N_r$ identity matrix and $\sigma^2$ for the element noise variance.

At the receiver side, the hybrid combiner $\mathbf{W}_{\mathrm{T}}$, is used to extract the transmitted data from the received signal, as follows:

$$\mathbf{y}_r = \mathbf{W}_{\mathrm{T}}^H\mathbf{H}\mathbf{F}_{\mathrm{T}}\mathbf{s} + \mathbf{W}_{\mathrm{T}}^H\mathbf{n}, \tag{3.3}$$

where $\mathbf{W}_{\mathrm{T}} = \mathbf{W}_{\mathrm{RF}}\mathbf{W}_{\mathrm{BB}}$, in which $\mathbf{W}_{\mathrm{BB}} \in \mathbb{C}^{N_{\mathrm{RF}} \times N_s}$ is the digital baseband combiner, and $\mathbf{W}_{\mathrm{RF}} \in \mathbb{C}^{N_r \times N_{\mathrm{RF}}}$ presents the RF analog combiner, which is implemented using phase shifters, where all its non-zero entries are constrained to satisfy the constant modulus i.e, $|\mathbf{W}_{\mathrm{RF}}|^2 = N_r^{-1}$.

### 3.2.2 Non Ideal Underground System Model

In real systems, both the transmitter and the receiver are affected by inevitable residual additive impairments that emerge from different sources, such as the antenna coupling, I/Q mistmatch, and the imperfect compensation of the quantization noise in the transceiver, ... etc. As a result, the received signal is distorted, while at the

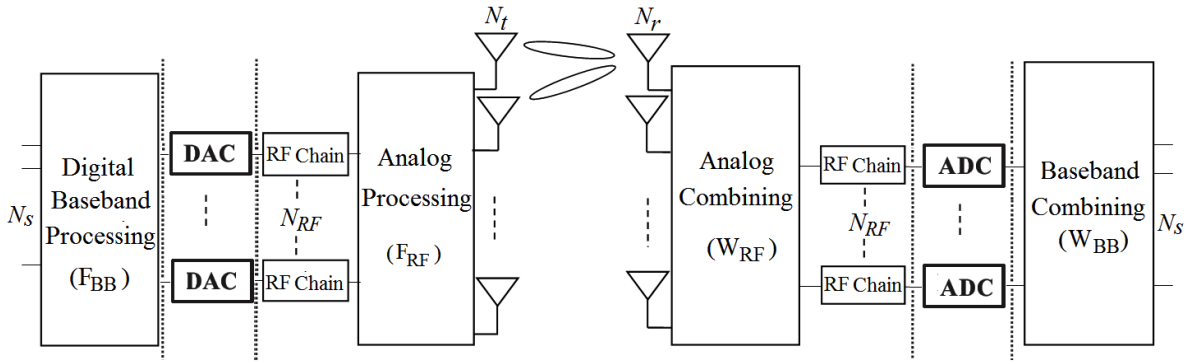


Figure 3.2: An illustration of a realistic basic hybrid mm-Wave MIMO underground system with transceiver hardware impairments.

transmitter side, a mismatch appears between the signal that is transmitted and the generated one. Generally, the transmitter and receiver distortion noises are modeled as Gaussian distributed processes, where their average power is proportional to the average of the transmit signal power, as shown by measurement results in [25]. On the other hand, there are hardware impairments which have a multiplicative distortion effect on the channel vector, hence causing channel attenuation and phase shifts. Herein, our analysis focuses on the impact of the residual additive hardware impairment only, while the study of multiplicative impairments is left for future work. For realistic performance evaluations of mm-Wave underground communication at 60 GHz, hardware impairments from the RF chains should be considered. As discussed in [27, 80], the impaired received signal can be modeled as:

$$\mathbf{y}_r = \mathbf{W}_{\mathrm{T}}^H \mathbf{H}(\mathbf{F}_{\mathrm{T}}\mathbf{s} + \boldsymbol{\eta}_t) + \mathbf{W}_{\mathrm{T}}^H \boldsymbol{\eta}_r + \mathbf{W}_{\mathrm{T}}^H \mathbf{n}, \tag{3.4}$$

where $\boldsymbol{\eta}_t, \boldsymbol{\eta}_r$ refer to the transceiver impairments residue in the transmitter and the receiver hardwares, respectively, and which are assumed to be independent of the transmitted signal. Motivated analytically by the central limit theorem, the distortion noises are modeled as Gaussian distributions. Mathematically speaking, these terms are given as [81]:

$$\boldsymbol{\eta}_t \sim \mathcal{N}(0, k_t^2 \mathrm{diag}(|q_{11}|^2, ..., |q_{N_t N_t}|^2)), \tag{3.5}$$

$$\boldsymbol{\eta}_r \sim \mathcal{N}(0, k_r^2 tr(\mathbf{Q})\mathbf{I}_{N_r}), \tag{3.6}$$

where the coefficients $k_t$ and $k_r$ are characterizing the levels of impairments at the transmitter and the receiver, respectively, $q_i$ denoting the $i^{th}$ diagonal element of the signal covariance matrix $\mathbf{Q}$, and $tr(.)$ stands for the trace of the matrix. In the LTE standard, the $k_t$ and $k_r$ were shown to be in the range $[0.08^2, 0.175^2]$ [26]. In practical mm-Wave systems, since cheap devices are encouraged to be used, the larger values of $k_t$ and $k_r$ are of interest in this work. Note that $k_t = k_r = 1$ in perfectly operating hardware while $k_t = k_r = 0$ for useless hardware that turns everything into distortion.

## 3.3 Geometrical-based Underground Channel Model

One way of designing high-speed systems for underground wireless communications is to utilize the mm-Wave frequency bands, especially the 60 GHz band. Nevertheless, the mm-Wave underground channel is considered as one of the most challenging mediums and has only recently come into focus again, due to the latest technical progresses in antennas fabrication and miniaturization, and the affordable measurement campaigns of the pertaining channels. There is now a growing interest in implementing MIMO systems in underground mines aiming for the improvement of the communication performance in an underground environment. For system design to, the performance simulation of underground communication systems to be accurate, a thorough understanding of the underlying MIMO channel and corresponding model is indispensable. The approach of geometry-based one ring modelling has widely been used for irregular shaped scattering environments, such as tunnels, due to its simplicity of representation. Thus, a geometry-based one ring model is proposed to represent the propagation within the mm-Wave MIMO underground channel, in the scenario where the transmitter is usually unobstructed by no scatterer, whereas the receiver is located at the center of a ring surrounded by scatterers, as illustrated in Figure 3.4.

Exploiting the real mine underground channel measurements is carried out for the extraction of the geometrical one ring model under the asumption that the scatters are sparse, which reflects indeed the reality [68]. During the measurements, and using a vector network analyzer (VNA) and patch antennas at the transmitter and the receiver, the former was maintained fixed, while the latter was moved at different locations along the gallery, from 1 m up to 10 m apart from the transmitter, with steps of 1m, as depicted in Figure 3.3. All the measurements at the receive patch antenna which are conducted at the various distances are exploited to form a large MIMO

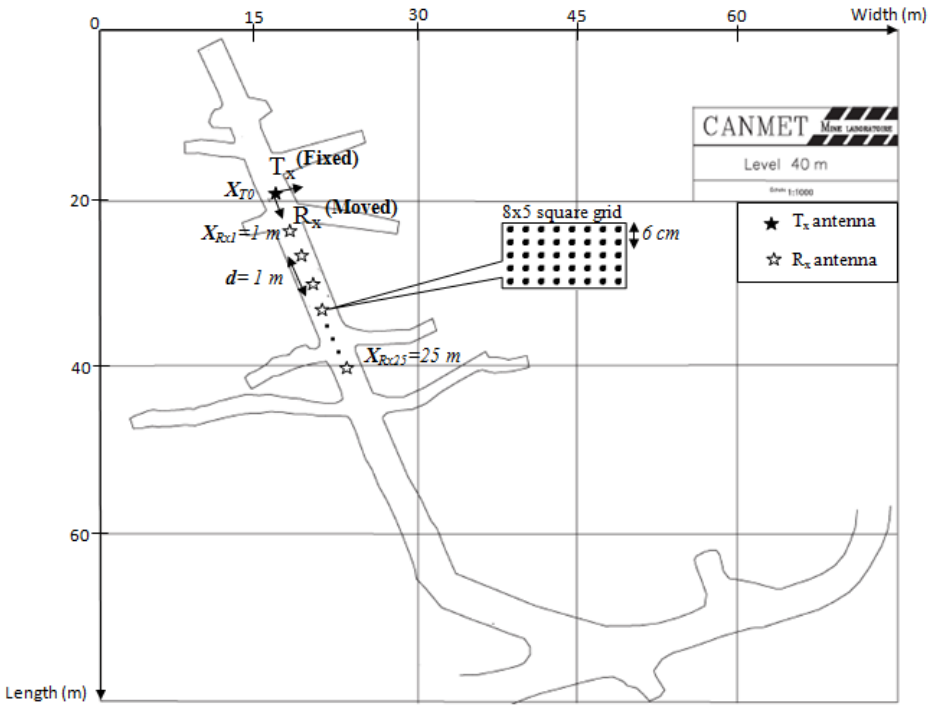


Figure 3.3: Underground gallery map.

scenario, namely massive MIMO. Furthermore, this model uses a 2D geometry by assuming that transmitted waves propagate only in a horizontal plane. It is therefore reasonable to assume that the receiver collects the signals from different directions determined by the distribution of the local scatterers. In deriving the channel model, the following assumptions are made:

- Every scatterer that lies at an angle $\phi^{\mathrm{Rx}}$ to the receiver is represented by a corresponding effective scatterer located at the same angle on the scatterer ring centered on the receiver.
- The effective scatterers are assumed to be distributed uniformly in $\phi^{\mathrm{Rx}}$.
- The local scatterers are located on a ring with radius $R$.

As it can be seen in Figure 3.4, the ring has a radius of $R$ and its center of the ring is located at 0, while the $l^{th}$ scatterer is designated by $S_l$ with $(l = 1, ..., L)$ and the AoD and AoA of the associated reflection path $l$ are denoted as $\phi^{\mathrm{Tx}}$ and $\phi^{\mathrm{Rx}}$, respectively. The set of AoAs $\{\phi^{\mathrm{Tx}}\}_l^L$ are modeled by independent and identically distributed (i.i.d.) random variables to characterize the azimuth spread of the signals at the receiver. Consequently, the set of AoDs $\{\phi^{\mathrm{Rx}}\}_l^L$ are similarly modelled as random variables whose distribution is determined by the one of the AoAs and

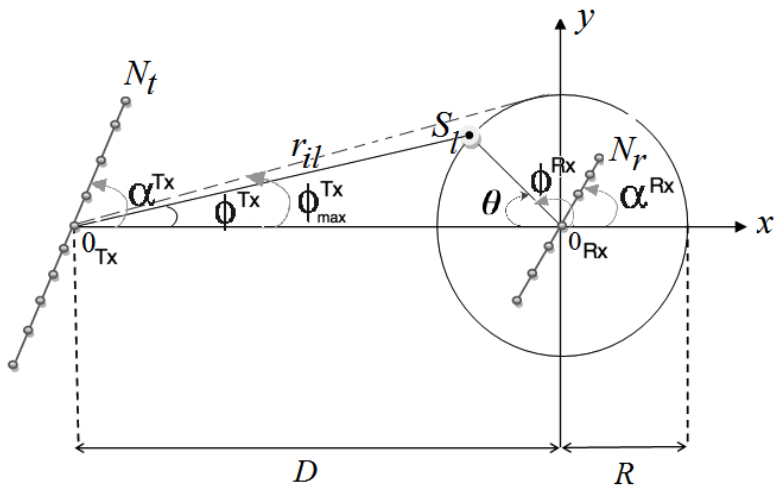


Figure 3.4: Illustration of the geometrical one ring model for a MIMO underground mining channel.

the geometrical parameters, such as $D$ and $R$, where $D$ is the distance between the transmitter and the receiver. Moreover, the $\phi^{\mathrm{Tx}}$ is limited by the maximal departure angle of the transmitt signal $\phi^{\mathrm{Tx}}_{\mathrm{max}}$, which is given as:

$$\phi^{\mathrm{Tx}}_{\mathrm{max}} = arctan(\frac{R}{D}) = \frac{R}{D}, \tag{3.7}$$

where $R$ is usually small in comparison with the distance $D$. The angles $\boldsymbol{\alpha}^{\mathrm{Tx}}$ and $\boldsymbol{\alpha}^{\mathrm{Rx}}$ in Figure 3.4 are the one from the horizontal axis to the transmit antenna array, and from the horizontal axis to that the receive antena array, respectively.

In this model, the path length from the $i^{th}$ transmit antenna to the $r^{th}$ receive antenna via the $l^{th}$ scatterer $S_l$ is obtained through geometrical considerations as a function of $D$ [82]. Indeed, applying the law of cosines in the triangle $0_{\mathrm{Tx}}S_l0_{\mathrm{Rx}}$, its exact expression can be obtained as follows:

$$d_{ilr} = R + \sqrt{(D^2 + R^2 - 2DR\cos(\boldsymbol{\theta}))}, \tag{3.8}$$

where $\boldsymbol{\theta} = \arcsin(\frac{r_{il}}{D})$ is the AoA of the $l^{th}$ scatterer, with $r_{il}$ being the position of the $l^{th}$ scatterer $S_l$ relative to the transmitter, which can be generated randomly as $U(1m, 7/4D)$ [83]. In the MIMO system, with $N_t$ transmit and $N_r$ receive antennas, the corresponding channel model generated by the one ring approach, corresponding to the $r^{th}$-$i^{th}$ link, is expressed as follows [84]:

$$H_{i,r} = \frac{1}{\sqrt{L}} \sum_{l=1}^{L} \sqrt{\mathcal{B}_{li,r}} a^t_l b^r_l e^{(-j2\pi(\frac{d_{ilr}}{\lambda}) + j\varphi_{li,r})}, \tag{3.9}$$

where $L$ is the number of multipath componentts, $\mathcal{B}_{li,r}$ is the $l^{th}$ measured time domain path loss obtained from the channel impulse response, for any fixed location between the transmitter and the receiver, $\varphi_{li,r}$ is the phase shift associated with each scatter $S_l$, which is assumed in our case as uniformly distributed in the interval $[-\pi, \pi]$, and $\lambda$ is the corresponding wavelength at the operating frequency, and $\boldsymbol{a}_l^t$ and $\boldsymbol{b}_l^r$ are the steering vectors at the transmitter and the receiver sides, respectively, which are defined as:

$$\boldsymbol{a}_l^t = [1, ..., e^{j\pi \frac{\delta_t}{\lambda}(N_t-1)[\cos(\boldsymbol{\alpha}^{\mathrm{Tx}}))+\boldsymbol{\phi}_{\max}^{\mathrm{Tx}} \sin(\boldsymbol{\alpha}^{\mathrm{Tx}}) \cos(\boldsymbol{\phi}^{\mathrm{Rx}})]}], \tag{3.10}$$

$$\boldsymbol{b}_l^r = [1, ..., e^{j\pi \frac{\delta_r}{\lambda}(N_r-1)[\cos(\boldsymbol{\phi}^{\mathrm{Rx}}-\boldsymbol{\alpha}^{\mathrm{Rx}})]}], \tag{3.11}$$

## 3.4 Achievable Rate Analysis

In this section, we derive the achievable data rate for the cases of ideal hardware hardware operation scenario, first, then generalize this to the one considering hardware impairments for MIMO underground system, with hybrid beamforming configuration. This aims at getting better insights into how those imperfections and analog beamformers affect the proposed system performance. By modeling the residual impairments as an additional distortion noise, expressions of the achievable rates for both hybrid and analog RF beamforming structures for mm-Wave underground MIMO system, are derived. According to (3.4), the achievable rate when adopting a fully analog beamforming scheme, in the absence of any distortion, could be written as follow:

$$\text{Rate} = \log_2 \det(\mathbf{I}_{\mathrm{Ns}} + \frac{P_s}{\sigma^2 N_s} \boldsymbol{R}_T^{-1} |\mathbf{W}_{\mathrm{RF}}^H \mathbf{H} \mathbf{F}_{\mathrm{RF}}|^2), \tag{3.12}$$

where $\boldsymbol{R}_T = \mathbf{W}_{\mathrm{RF}}^H \mathbf{W}_{\mathrm{RF}}$ is the post-processing noise covariance matrix. Similarly, the achievable rate of a hybrid beamforming-based MIMO underground system is given by the expression:

$$\text{Rate} = \log_2 \det(\mathbf{I}_{\mathrm{Ns}} + \frac{P_s}{\sigma^2 N_s} \boldsymbol{R}_T^{-1} |\mathbf{W}_T^H \mathbf{H} \mathbf{F}_{\mathrm{T}}|^2), \tag{3.13}$$

wherein $\boldsymbol{R}_T = \mathbf{W}_{\mathrm{BB}}^H \mathbf{W}_{\mathrm{RF}}^H \mathbf{W}_{\mathrm{RF}} \mathbf{W}_{\mathrm{BB}}$ is the equivalent noise covariance matrix. In the presence of non-ideal, yet practical transceiver hardware imperfections, as given in (3.4), the achievable rate is could be expressed as:

$$\text{Rate} = \log_2 \det(\mathbf{I}_{\mathrm{Ns}} + \frac{P_s}{\sigma^2 N_s} \boldsymbol{R}_\eta^{-1} |\mathbf{W}^H \mathbf{H} \mathbf{F}_{\mathrm{T}}|^2), \tag{3.14}$$

where $\boldsymbol{R}_\eta$ represents the noise covariance matrix with hardware imperfections, which is formulated as:

$$\boldsymbol{R}_\eta = (k_t^2 \frac{P_s}{N_s} + P_s k_r^2) \mathbf{W}_{\mathrm{T}}^H \mathbf{H} \mathbf{H}^H \mathbf{W}_{\mathrm{T}}, \tag{3.15}$$

These expressions provide important evaluations of the practical impact of hardware impairments, and the realistic efficiency of the deployment of MIMO underground system.

## 3.5 Hybrid Beamforming/Combining Design

To alleviate the hardware constraints, while realizing a full potential of the proposed mm-Wave MIMO underground system as mentioned previously, we incorporate the hybrid beamforming in our system. The optimal hybrid beamforming is built by minimizing the Euclidean distance between the fully digital beamformer $\mathbf{F}^{\mathrm{opt}}$ and the hybrid beamformer, which leads to the maximization of the achievable rate of the mm-Wave MIMO underground system in (3.14). Based on SVD decomposition of the channel $\mathbf{H}$, we have:

$$\mathbf{H} = \mathbf{U} \Xi \mathbf{V} = [u_1, u_2 ..., u_{N_t}] \begin{bmatrix} \xi_1 & 0 & \dots & 0 \\ 0 & \xi_2 & \dots & 0 \\ \vdots & \vdots & \ddots & \vdots \\ 0 & 0 & \dots & \xi_{N_t} \end{bmatrix} \begin{bmatrix} v_1 \\ v_2 \\ \vdots \\ v_{N_r} \end{bmatrix}, \tag{3.16}$$

where $\Xi$ is the diagonal matrix containing the singular values of $\mathbf{H}$ arranged in a decreasing order and which satisfy $\xi_1 \geq ... \geq \xi_{N_t} \geq 0$, $\mathbf{U} \in \mathbb{C}^{Nt \times Nt}$ and $\mathbf{V} \in \mathbb{C}^{Nr \times Nr}$ are the transmit and receive unitary matrices. We note that the optimal unconstrained unitary beamformer for $\mathbf{H}$ is simply given by $\mathbf{F}^{\mathrm{opt}} = \mathbf{V}$. Proceeding with the design of $\mathbf{F}_{\mathrm{BB}}$, the hybrid beamforming design problem can be formulated as:

$$\mathbf{F}_{\mathrm{RF}}^{\mathrm{opt}}\mathbf{F}_{\mathrm{BB}}^{\mathrm{opt}} = \underset{\mathbf{F}_{\mathrm{RF}}\mathbf{F}_{\mathrm{BB}}}{\arg\min}\|\mathbf{F}^{\mathrm{opt}} - \mathbf{F}_{\mathrm{RF}}\mathbf{F}_{\mathrm{BB}}\|_F \tag{3.17a}$$

$$\mathbf{F}_{\mathrm{RF}}^{c} \in \{\boldsymbol{a}_l^t, 1 \leq l \leq L\} \tag{3.17b}$$

$$\|\mathbf{F}_{\mathrm{RF}}\mathbf{F}_{\mathrm{BB}}\|_F^2 = N_s \tag{3.17c}$$

where the vector $\mathbf{F}_{\mathrm{RF}}^{c}$ is the $c^{th}$ column of the $\mathbf{F}_{\mathrm{RF}}$ matrix which is selected from the set of transmit steering vectors $\boldsymbol{a}_l^t$, and $\|\mathbf{F}_{\mathrm{RF}}\mathbf{F}_{\mathrm{BB}}\|_F^2 = N_s$ is the power constraint at the transmitter, while $\mathbf{F}_{\mathrm{RF}}$ and $\mathbf{F}_{\mathrm{BB}}$ are the analog and digital beamformers to be optimized. It is intuitively true that the optimal hybrid precoders should be sufficiently close to the unconstrained optimal digital beamformer.

**Algorithm 1** Hybrid beamforming design

**Inputs:** $\mathbf{F}_{\mathrm{opt}}$, $\mathbf{A}_{\mathrm{Tx}}$

**Output:** $\mathbf{F}_{\mathrm{RF}}$, $\mathbf{F}_{\mathrm{BB}}$.

**Initialisation**: $\mathbf{F}_{\mathrm{RF}}$=$\emptyset$; $\mathbf{F}_{\mathrm{res}}$=$\mathbf{F}_{\mathrm{opt}}$.

1: **for** $i \leq N_{\mathrm{RF}}$ **do**

2: $\boldsymbol{\psi}_t = \mathbf{A}_{\mathrm{Tx}}^H\mathbf{F}_{\mathrm{res}}$;

3: $q = \underset{l=1,\ldots,L}{\mathrm{argmax}}(\boldsymbol{\psi}_t^H\boldsymbol{\psi}_t)_l$;

4: $\mathbf{F}_{\mathrm{RF}} = [\mathbf{F}_{\mathrm{RF}} \mid (\mathbf{A}_{\mathrm{Tx}})^{(q)}]^T$

5: $\mathbf{F}_{\mathrm{BB}} = (\mathbf{F}_{\mathrm{RF}}^H\mathbf{F}_{\mathrm{RF}})^{-1}\mathbf{F}_{\mathrm{RF}}^H\mathbf{F}_{\mathrm{opt}}$

6: $\mathbf{F}_{\mathrm{res}} = \frac{\mathbf{F}_{\mathrm{opt}}-\mathbf{F}_{\mathrm{RF}}\mathbf{F}_{\mathrm{BB}}}{\|\mathbf{F}_{\mathrm{opt}}-\mathbf{F}_{\mathrm{RF}}\mathbf{F}_{\mathrm{BB}}\|_F}$

7: **end for**

8: $\mathbf{F}_{\mathrm{BB}} = \frac{\mathbf{F}_{\mathrm{BB}}}{\|\mathbf{F}_{\mathrm{RF}}\mathbf{F}_{\mathrm{BB}}\|_F}$

9: $\mathbf{F}_{\mathrm{RF}}$, and $\mathbf{F}_{\mathrm{BB}}$

Following the sparsity design approach, this problem could be solved using the pursuit methods for sparse approximation, such as the OMP algorithm, by finding

the projection of on the set of hybrid precoders with $\mathbf{A}_{\mathrm{Tx}}$, where $\mathbf{A}_{\mathrm{Tx}} = [\boldsymbol{a}_1^t, ..., \boldsymbol{a}_L^t]$ is a $N_t \times L$ matrix. The hybrid beamforming design procedure at the transmit side, relying on OMP algorithm, for the mm-Wave MIMO underground system, is summarized in **Algorithm 1**. In steps 2 and 3 of the algorithm, the row of $\mathbf{A}_{\mathrm{Tx}}$ that is most strongly correlated with the residual error $\mathbf{F}_{\mathrm{res}}$ is chosen for the transmitter beamforming. Then the selected column is appended to $\mathbf{F}_{\mathrm{RF}}$ (step 4). In step 5, LS solution is used to calculate $\mathbf{F}_{\mathrm{BB}}$, then the contribution of the selected vector is removed in step 6 and the algorithm proceeds to find the column along which $\mathbf{F}_{\mathrm{res}}$ has the largest projection. The process continues until all $N_{\mathrm{RF}}$ columns of $\mathbf{F}_{\mathrm{RF}}$ have been determined. At the end of this algorithm, the power constraint is guaranteed by step 8.

Then at the reception side, for the realistic design of the hybrid combiners for the mm-Wave MIMO underground receiver in Figure 3.2, we engage in the minimization of the MSE between the transmitted and processed received signals, over the practical mm-Wave MIMO underground channel including transceiver hardware impairment, by relying on the OMP method [85]. In such case, the problem for which the solution provides the optimal combiners, denoted as $(\mathbf{W}_{\mathrm{RF}}^{\mathrm{opt}}, \mathbf{W}_{\mathrm{BB}}^{\mathrm{opt}})$, takes the following form [86]:

$$\begin{aligned}\mathbf{W}_{\mathrm{RF}}^{\mathrm{opt}}\mathbf{W}_{\mathrm{BB}}^{\mathrm{opt}} &= \underset{\mathbf{W}_{\mathrm{RF}}\mathbf{W}_{\mathrm{BB}}}{\arg\min} \quad \mathbb{E}\left[\left\|\mathbf{s} - \left\{\mathbf{W}_{\mathrm{BB}}^H\mathbf{W}_{\mathrm{RF}}^H\left(\mathbf{H}(\mathbf{F}_{\mathrm{T}}\mathbf{s} + \boldsymbol{\eta}_t) + \boldsymbol{\eta}_r + \mathbf{n}\right)\right\}\right\|_2^2\right] \\ &= \underset{\mathbf{W}_{\mathrm{RF}}\mathbf{W}_{\mathrm{BB}}}{\arg\min} \quad \mathbb{E}\left[\left\|\mathbf{s} - \mathbf{W}_{\mathrm{BB}}^H\mathbf{W}_{\mathrm{RF}}^H\mathbf{y}\right\|_2^2\right],\end{aligned}$$

$$\text{s.t} \quad \mathbf{W}_{\mathrm{RF}}^c \in \{\boldsymbol{b}_l^r, 1 \leq l \leq L\} \tag{3.18a}$$

where $\mathbf{W}_{\mathrm{RF}}^c$ is the $c^{th}$ column of the $\mathbf{W}_{\mathrm{RF}}$ matrix which is selected from the set of receive steering vectors $\boldsymbol{b}_l^r$. Herein, we assume that the optimal beamformers matrices, $(\mathbf{F}_{\mathrm{RF}}^{\mathrm{opt}}, \mathbf{F}_{\mathrm{BB}}^{\mathrm{opt}})$, which have been determined in the previous step at the transmitter side, are fixed. In the presence of hardware limitations that restrict the set of feasible linear receivers, solving (3.18) analytically impossible. To overcome this difficulty, we rewrite the optimization problem in (3.18) in terms of the well-known solution to MMSE minimization problems given as [87]:

$$\mathbf{M}_{\mathrm{MMSE}}^H = \mathbb{E}[\mathbf{s}\mathbf{y}^H]\mathbb{E}[\mathbf{y}\mathbf{y}^H]^{-1}, \tag{3.19}$$

where $\mathbf{M}_{\mathrm{MMSE}}^H$ is the optimal MMSE combiner. We start by reformulating the problem in (3.18) by expanding MMSE as follows:

$$\begin{aligned}\mathbb{E}\left[\left\|\mathbf{s}-\mathbf{W}_{\mathrm{BB}}^{H}\mathbf{W}_{\mathrm{RF}}^{H}\mathbf{y}\right\|_2^2\right] &= \mathbb{E}\left[(\mathbf{s}-\mathbf{W}_{\mathrm{BB}}^{H}\mathbf{W}_{\mathrm{RF}}^{H}\mathbf{y})^{H}(\mathbf{s}-\mathbf{W}_{\mathrm{BB}}^{H}\mathbf{W}_{\mathrm{RF}}^{H}\mathbf{y})\right] \\ &= \mathbb{E}\left[tr((\mathbf{s}-\mathbf{W}_{\mathrm{BB}}^{H}\mathbf{W}_{\mathrm{RF}}^{H}\mathbf{y})(\mathbf{s}-\mathbf{W}_{\mathrm{BB}}^{H}\mathbf{W}_{\mathrm{RF}}^{H}\mathbf{y})^{H})\right] \\ &= tr\big(\mathbb{E}\left[(\mathbf{s}\mathbf{s}^{H})\right]\big) - 2\mathbb{R}tr\big(\mathbb{E}\left[(\mathbf{s}\mathbf{y}^{H})\mathbf{W}_{\mathrm{RF}}\mathbf{W}_{\mathrm{BB}}\right]\big)+ \\ & tr\big(\mathbf{W}_{\mathrm{BB}}^{H}\mathbf{W}_{\mathrm{RF}}^{H}\mathbb{E}\left[(\mathbf{y}\mathbf{y}^{H})\right]\mathbf{W}_{\mathrm{RF}}\mathbf{W}_{\mathrm{BB}}\big).\end{aligned} \tag{3.20}$$

We now note that since the optimization problem in (3.18) is over the variables $\mathbf{W}_{\mathrm{RF}}$ and $\mathbf{W}_{\mathrm{BB}}$, we can add any term that is independent of $\mathbf{W}_{\mathrm{RF}}$ and $\mathbf{W}_{\mathrm{BB}}$ to its objective function without changing the outcome of the optimization. Thus, we choose to add the constant term $tr(\ \mathbf{M}_{\mathrm{MMSE}}^{H}\mathbb{E}[\mathbf{y}\mathbf{y}^{H}]\mathbf{M}_{\mathrm{MMSE}}) - tr(\mathbb{E}[\mathbf{s}\mathbf{s}^{H}])$ and minimize the equivalent objective function:

$$\begin{aligned}\mathbf{W}_{\mathrm{RF}}^{\mathrm{opt}}\mathbf{W}_{\mathrm{BB}}^{\mathrm{opt}} &= tr(\mathbf{M}_{\mathrm{MMSE}}^{H}\mathbb{E}\left[\mathbf{y}\mathbf{y}^{H}\right]\mathbf{M}_{\mathrm{MMSE}}) - 2\mathbb{R}\{tr(\mathbb{E}\left[(\mathbf{s}\mathbf{y}^{H})\mathbf{W}_{\mathrm{RF}}\mathbf{W}_{\mathrm{BB}}\right]\}+ \\ & tr(\mathbf{W}_{\mathrm{BB}}^{H}\mathbf{W}_{\mathrm{RF}}^{H}\mathbb{E}\left[(\mathbf{y}\mathbf{y}^{H})\right]\mathbf{W}_{\mathrm{RF}}\mathbf{W}_{\mathrm{BB}}) \\ &= tr(\mathbf{M}_{\mathrm{MMSE}}^{H}\mathbb{E}\left[\mathbf{y}\mathbf{y}^{H}\right]\mathbf{M}_{\mathrm{MMSE}}) - 2\mathbb{R}\{tr(\mathbf{M}_{\mathrm{MMSE}}^{H}\mathbb{E}\left[\mathbf{y}\mathbf{y}^{H}\right]\mathbf{W}_{\mathrm{RF}}\mathbf{W}_{\mathrm{BB}}\}+ \\ & tr(\mathbf{W}_{\mathrm{BB}}^{H}\mathbf{W}_{\mathrm{RF}}^{H}\mathbb{E}\left[(\mathbf{y}\mathbf{y}^{H})\right]\mathbf{W}_{\mathrm{RF}}\mathbf{W}_{\mathrm{BB}}) \\ &= tr\big((\mathbf{M}_{\mathrm{MMSE}}^{H}-\mathbf{W}_{\mathrm{BB}}^{H}\mathbf{W}_{\mathrm{RF}}^{H}\mathbb{E}\left[(\mathbf{y}\mathbf{y}^{H})\right]\times(\mathbf{M}_{\mathrm{MMSE}}^{H}-\mathbf{W}_{\mathrm{BB}}^{H}\mathbf{W}_{\mathrm{RF}}^{H})^{H}\big) \\ &= \|\mathbb{E}\left[(\mathbf{y}\mathbf{y}^{H})\right]^{\frac{1}{2}}(\mathbf{M}_{\mathrm{MMSE}}-\mathbf{W}_{\mathrm{BB}}\mathbf{W}_{\mathrm{RF}})^{H})\|_F^2,\end{aligned} \tag{3.21}$$

As we have $tr(\mathbb{E}\left[(\mathbf{s}\mathbf{y}^{H})\right]\mathbf{W}_{\mathrm{RF}}\mathbf{W}_{\mathrm{BB}} = tr(\mathbb{E}\left[(\mathbf{s}\mathbf{y}^{H})\right]\mathbb{E}\left[(\mathbf{y}\mathbf{y}^{H})\right]^{-1}\mathbb{E}[\mathbf{y}\mathbf{y}^{H}]\mathbf{W}_{\mathrm{RF}}\mathbf{W}_{\mathrm{BB}})$ and using the fact that $\mathbf{M}_{\mathrm{MMSE}}^{H}$=$\mathbb{E}[\mathbf{s}\mathbf{y}^{H}]\mathbb{E}[\mathbf{y}\mathbf{y}^{H}]^{-1}$, which implies that $tr(\mathbb{E}\left[(\mathbf{s}\mathbf{y}^{H})\right]\mathbf{W}_{\mathrm{RF}}\mathbf{W}_{\mathrm{BB}}$= $tr(\mathbf{M}_{\mathrm{MMSE}}^{H}\mathbb{E}\left[(\mathbf{y}\mathbf{y}^{H})\right]\mathbf{W}_{\mathrm{RF}}\mathbf{W}_{\mathrm{BB}})$, it follows based on (3.21) that optimization problem is equivalent to finding hybrid combiners which solved as the following problem:

$$\mathbf{W}_{\mathrm{RF}}^{\mathrm{opt}}\mathbf{W}_{\mathrm{BB}}^{\mathrm{opt}} = \underset{\mathbf{W}_{\mathrm{RF}}\mathbf{W}_{\mathrm{BB}}}{\arg\min} \quad \left\|\mathbb{E}[\mathbf{y}\mathbf{y}^{H}]^{\frac{1}{2}}(\mathbf{M}_{\mathrm{MMSE}}-\mathbf{W}_{\mathrm{RF}}\mathbf{W}_{\mathrm{BB}})\right\|_F \tag{3.22a}$$

$$\text{s.t} \quad \mathbf{W}_{\mathrm{RF}}^{c} \in \{\boldsymbol{b}_l^{r}, 1 \le l \le L\} \tag{3.22b}$$

This amounts to finding the projection of the unconstrained MMSE combiner $\mathbf{M}_{\mathrm{MMSE}}$ onto the set of hybrid combiners of the form $\mathbf{W}_{\mathrm{RF}}\mathbf{W}_{\mathrm{BB}}$ with $\mathbf{W}_{\mathrm{RF}}^{c} \in \boldsymbol{b}_l^{r}$. Thus, the design of MMSE receivers for the mm-Wave MIMO undergroud system of interest closely resembles the design of its hybrid beamformers. However, unlike the design

of the transmit beamforming, the projection now is not performed with respect to the standard norm $\|.\|_F^2$ but to $\mathbb{E}[\mathbf{y}\mathbf{y}^H]$-weighted Frobenius norm. Nevertheless, the same observations which have allowed us to leverage the structure of mm-Wave underhround channel to solve the precoding problem, as discussed before, could be translated to the receiver side to solve the combiner problem as well. Namely, because of the sparse nature of underground channel at 60 GHz, near-optimal receivers can be found by further constraining $\mathbf{W}_{\text{RF}}$ to have columns of the form $\mathbf{A}_{\text{Rx}}$, with $\mathbf{A}_{\text{Rx}}$, where $\mathbf{A}_{\text{Rx}} = [\boldsymbol{b}_1^r, ..., \boldsymbol{b}_L^r]$ is a $N_r \times L$ matrix. Thus, **Algorithm 2** provides the combiner solution by first finding the vector $\mathbf{A}_{\text{Rx}}$ and then designing $N_{\text{RF}}$ beamforming vectors to form the optimal $\mathbf{W}_{\text{RF}}$. After determining $\mathbf{W}_{\text{RF}}$, the optimal $\mathbf{W}_{\text{BB}}$ is calculated using step 5.

**Algorithm 2** Hybrid combiner design with hardware impairments

**Inputs:** $\mathbf{M}_{\text{MMSE}}$, $\mathbf{A}_r$

**Output:** $\mathbf{W}_{\text{RF}}$, $\mathbf{W}_{\text{BB}}$.

**Initialisation**: $\mathbf{W}_{\text{RF}}=\emptyset$; $\mathbf{W}_{\text{res}}=\mathbf{M}_{\text{MMSE}}$.

1: **for** $i \leq N_{\text{RF}}$ **do**

2: $\boldsymbol{\psi}_r = \mathbf{A}_r^H \mathbb{E}[\mathbf{y}\mathbf{y}^H]\mathbf{W}_{\text{res}}$;

3: $q = \underset{l=1,...,L}{\text{argmax}} (\boldsymbol{\psi}_r \boldsymbol{\psi}_r^H)_l$;

4: $\mathbf{W}_{\text{RF}} = [\mathbf{W}_{\text{RF}} \mid (\mathbf{A}_r)^{(q)}]$

5: $\mathbf{W}_{\text{BB}} = (\mathbf{W}_{\text{RF}}^H \mathbb{E}[\mathbf{y}\mathbf{y}^H]\mathbf{W}_{\text{RF}})^{-1} \mathbf{W}_{\text{RF}}^H \mathbb{E}[\mathbf{y}\mathbf{y}^H]\mathbf{M}_{\text{MMSE}}$

6: $\mathbf{W}_{\text{res}} = \frac{\mathbf{M}_{\text{MMSE}} - \mathbf{W}_{\text{RF}}\mathbf{W}_{\text{BB}}}{\|\mathbf{M}_{\text{MMSE}} - \mathbf{W}_{\text{RF}}\mathbf{W}_{\text{BB}}\|_F}$

7: **end for**

8: $\mathbf{W}_{\text{BB}} = \frac{\mathbf{W}_{\text{BB}}}{\|\mathbf{W}_{\text{RF}}\mathbf{W}_{\text{BB}}\|_F}$

9: $\mathbf{W}_{\text{RF}}$, and $\mathbf{W}_{\text{BB}}$

## 3.6 Simulation Results

In this section, we provide numerical results to validate the achievable rate performance of the proposed mm-Wave MIMO underground system, incorporating hybrid beamforming technique, over the underground mine channel, for which measurements have been fitted using geometrical one ring model. Analog beamforming and digital beamforming, implemented within a similar architecture as the proposed scheme, and relying on the one-ring channel model, are taken as a reference to study the performance penalty with hardware defaults. For the ideal and non ideal systems, the achievable rate results have been obtained by means of Monte Carlo simulations using $10^5$ trails. The system considers the practical hardware imperfections at both transmitter and receiver sides, and is operating in the frequencies ranging from 57 to 62 GHz, thus has a bandwidth of 5 GHz. Furthermore, it is assumed that the transmitter and the receiver are equipped with equal number of antenna elements $N_t = N_r$= 20, the number of RF chains of most of simulations is $N_{\text{RF}} = N_s = 2$, the number of paths in the geometrical model is $L = 3$. Distortion due to residual hardware error is modeled with parameters $k_t$=$k_r$=0.15.

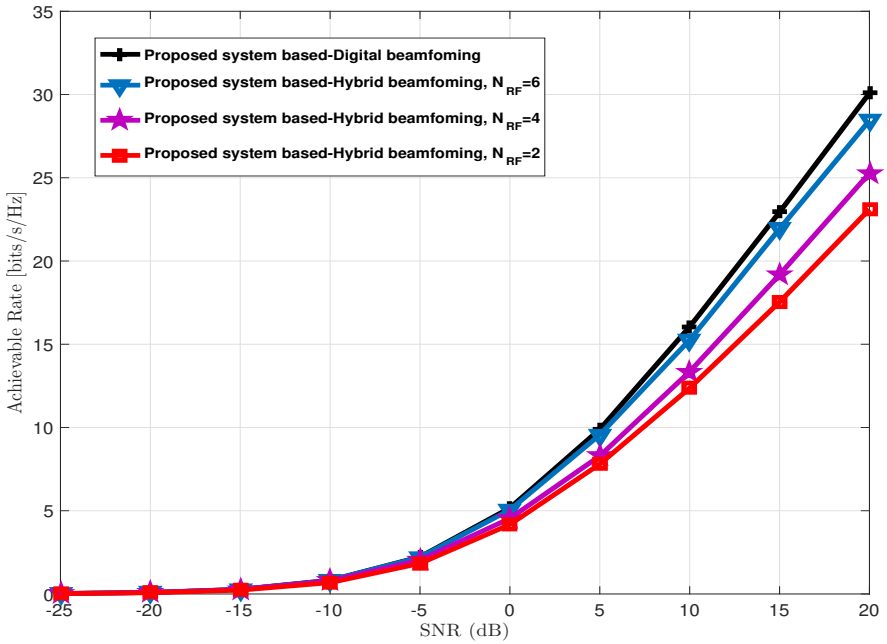


Figure 3.5: Impact of number of RF chains on the data rate performance of the proposed hybrid-beamforming-based mm-Wave uderground MIMO scheme.

Firstly, the achievable rate of the proposed system incorporating hybrid beam-

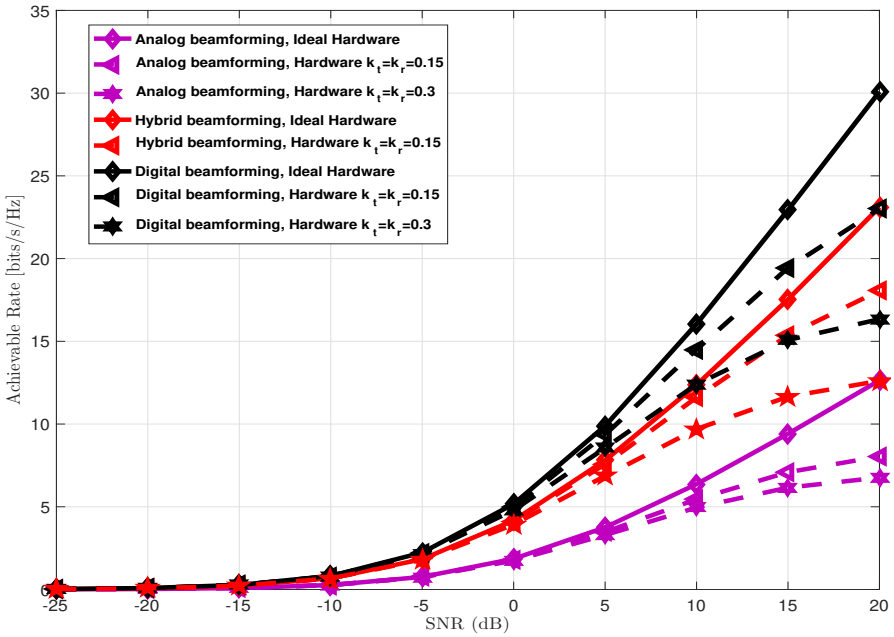


Figure 3.6: Performance comparison of the proposed system in the modeled underground mine channel with different levels of impairments.

forming is compared to the optimal fully digital beamforming-based alternative, and the corresponding results are illustrated in Figure 3.5. The analysis has been carried out with SNR ranging from $-25$ dB to 20 dB, when increasing the number of RF chains at the transceiver. From this Figure, it can be seen that the achievable rate of the proposed system is enhanced as the number of RF chains increases and becomes close to the attained performance of the optimal digital scheme, with a limited number of RF chains (6 in our case).

Figure 3.6 investigates the effect of the hardware impairments on the performance of the proposed system, relative to the fully-analog and the fully-digital counterparts. For this, the parameters $k_t$ and $k_r$ are varied in the set $\{0, 0.15, 0.3\}$. From Figure 3.6, we observe that the presence of the imperfections induces a saturation phenomena on the achieved rate at relatively high SNR values. Hence, whatever is the offered SNR, the system is not able to go beyond a given achievable rate. The reason for this effect is that the distortion noise power on both sides grows linearly and unboundedly with the transmit power. It is also observed that digital beamforming-based system experiences a critical performance penalty which exceeds 10 dB, when the hardware conditions vary from being ideal to undergoing an impairment factor of 0.3 at both the transmitter and the receiver sides. The proposed solution exhibits a little higher robustness to such hardware deviations from ideal case and outperforms

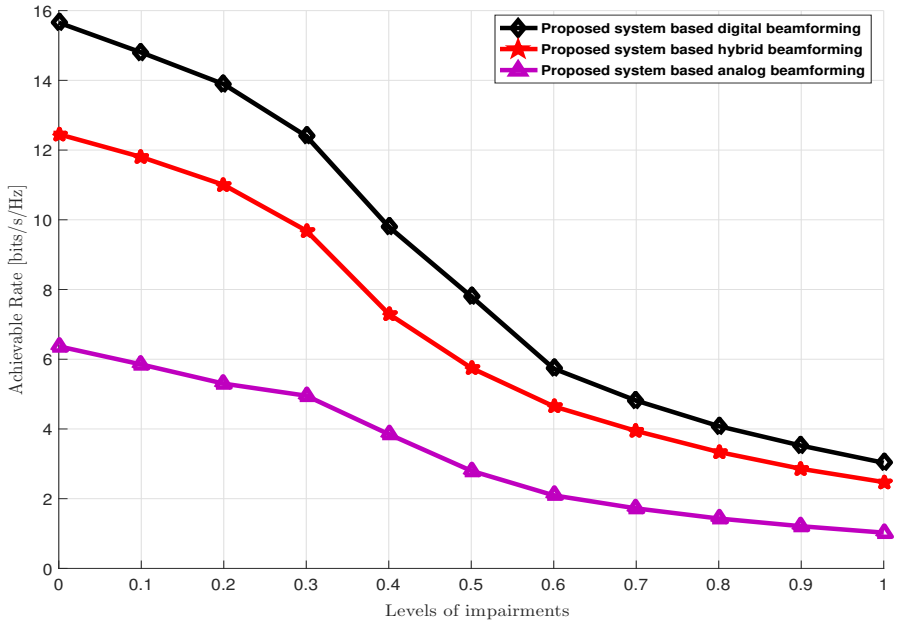


Figure 3.7: Impact of the transceiver impairment levels on the achievable rate of MIMO underground system.

digital beamforming-based system regardless of the conditions of operations of the hardware. Because of this, the proposed solution is considered appropriate for practical system deployments in such underground channels. Furthermore, we observe that, except for the fully analog scheme which is critically penalized by the hardware impairments, an increase in SNR tends to increase the achievable rate in both ideal and non-ideal conditions, for the proposed and the fully-digital schemes.

In Figure 3.7, we investigate the achievable rate performance of mm-Wave MIMO underground system as a function of the transceiver hardware impairments, $k_t = k_r$, under $SNR = 10$ dB. For this, the parameters $k_t$ and $k_r$ are varied to emulate the variation of the degree of impairments from non-existent to high. From Figure 3.7 comparing the behaviour of the proposed scheme along with analog and optimal digital beamforming architectures face to hardware defaults, it is seen that a performance loss is noted in the presence of increasing hardware distorsion conditions. More particularly, It is observed that the optimal fully-digital-beamforming scheme is the one exhibiting the highest degree of sensitivity to hardware defaults, which questions its suitability for such conditions. By contrast, the proposed solution is much more resilient to such imperfections, and performs in a comparable way to the optimal scheme when those get high. The fully-analog beamforming scheme attains a limited rate even in idealistic hardware operation, with this decreasing more with

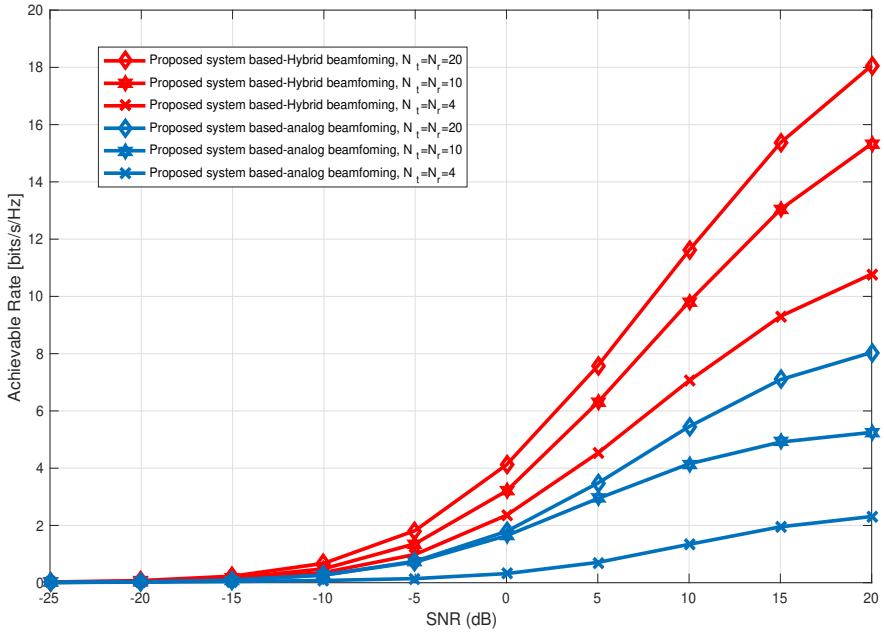


Figure 3.8: Performance comparison of mm-Wave MIMO underground system based-hybrid beamforming and analog beamforming-based counterpart for geometric underground channel with different antennas configurations.

higher hardware imperfections.

Figure 3.8 shows the performance comparison of the impaired mm-Wave MIMO underground system and fully-analog beamforming-based counterpart, under different antennas configuration $N_t = N_r = \{4, 10, 20\}$, both adopting geometrical one-ring -based underground channel model. The impairment factors during these simulations is maintained at $k_t$=$k_r$=0.15. From the Figure 3.8, it can be observed that the data rates of both systems are enhanced with increasing number of antennas. Furthermore, for the impingement of the hardware impairments on the fully-analog beamforming scheme is more critical, since the corresponding provided data rate with a $20 \times 20$ MIMO configuration, is inferior to that of the proposed hybrid-beamforming solution using a $4 \times 4$ antenna configuration. Again, this substantiates the efficacy of adopting the proposed hybrid beamforming for hardware impaired mm-Wave MIMO underground settings. Needless to mention that the gain gap retaining of hybrid beamforming over fully analog alternative increases with SNR.

Figure 3.9 shows the impact of the number of the path $L$ on the achievable rate of mm-Wave underground system-based hybrid precoding scheme. Its clear from the figure that at high SNR range, the degradation in the achievable rate performance of mm-Wave MIMO underground system is expected, as L increases. However, at low

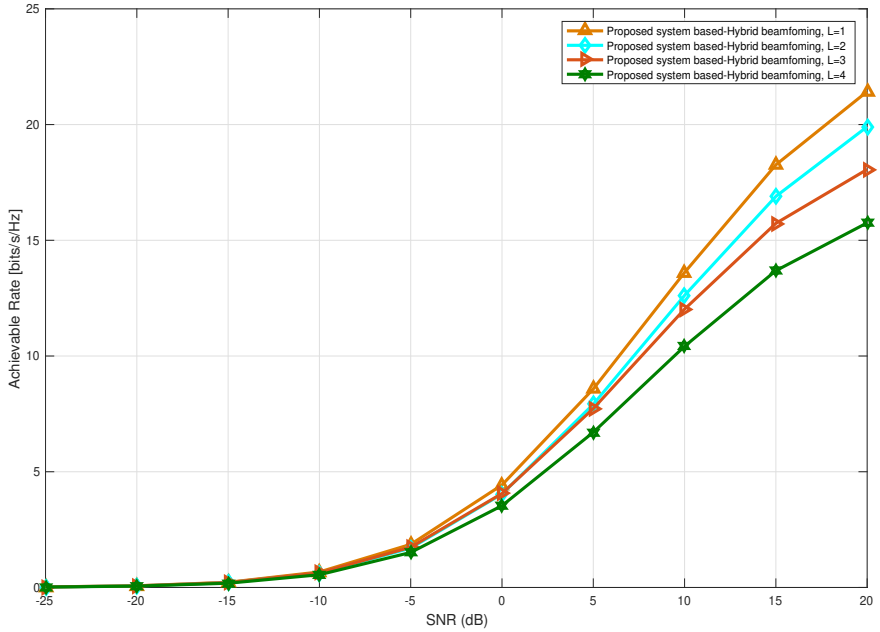


Figure 3.9: Effect of the multipaths on the achievable rate of mm-Wave MIMO underground system based hybrid beamforming system.

SNR regime the results indicate that the latter degradation is not quite significant. As expected, this technique is best used for channels with a few paths, e.g., mm-Wave underground channels.

Figure 3.10 shows the achievable rate performance of the proposed hardware impaired MIMO underground system based-hybrid precoding scheme with different Tx-Rx distances $d = \{3m, 5m, 10m\}$. Its noted that the achievable rate of the underground channel depend on the distacne between the Tx and Rx. More the distance increase, more the received power decrease for the mm-Wave, which reduce the coverture zone and limit the ray. More particulary, the performance degradation of the system at the distance d=10 m confirm the corresponding measurement of the channel at the 60 GHz in real undergreound mine environement.

Figure 3.11 shows the achievable rate achieved by increasing the data streams of the hardware impaired mm-Wave MIMO underground system based-hybrid beamforming scheme when the RF chains at the transceiver is fixed at 2. Clearly the increasing of the transmitted data streams increase the data rate of the proposed system especially at high SNR range.

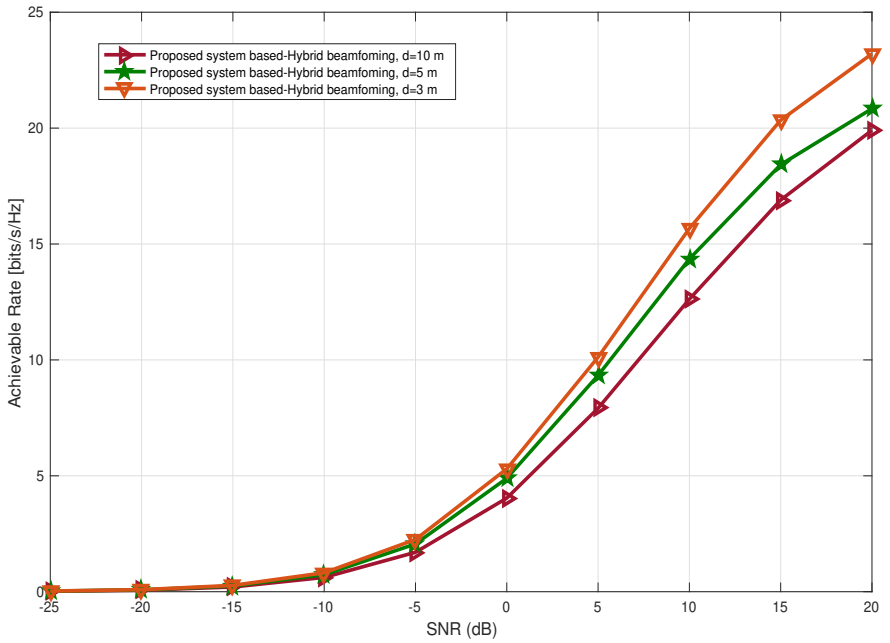


Figure 3.10: Achievable rate performance of hardware impaired mm-Wave MIMO underground system based-hybrid beamforming scheme with different Tx-Rx distances.

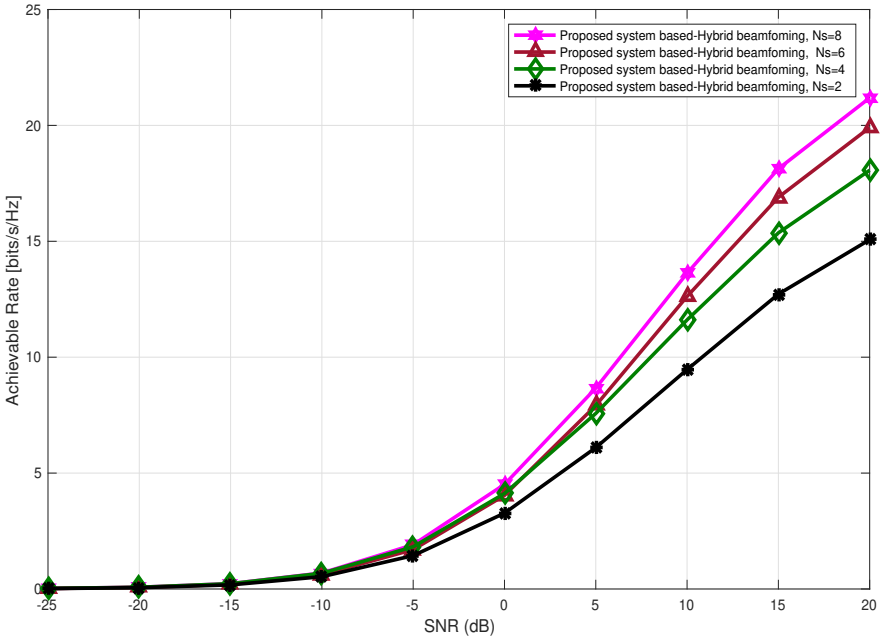


Figure 3.11: Achievable rate performance of hardware impaired mm-Wave MIMO underground system based-hybrid precoding scheme with different Ns data streams.

## 3.7 Conclusion

The impact of hardware imperfections play an crucial role in realistic scenarios. In this chapter, we consider the hardware imperfections, pertaining to the transmit and receive RF chains, in the design of the hybrid beamformer processing, deployed in the proposed mm-Wave MIMO underground architecture. Our work has taken a first look at the impact of transceiver hardware impairments on the performance of mm-Wave MIMO undergrund system-based hybrid beamformer, and has been also included for both fully digital beamforming structure and analog RF beamforming. We have applied a 2-D geometrical channel model, which is based on one ring configuration, to describe the propagation mechanism of our underground channel, and achievable rate performance was investigated based on this model and the modified transceiver structure under the idealistic assumptions of perfect CSI. Based on these conditions, a new expression for the achievable rate with transceiver hardware impairments was derived, using a additive distortion model. The higher performance and robustness against hardware imperfections of the proposed solution, relative to digital beamforming-based counterpart, have been demonstrated in these mm-Wave MIMO underground environments. Numerical results corroborate that the architecture indeed meets such objectives in a viable way, and shown that the hybrid beamforming processing attain reasonable gains compared with analog beamforming and achieve a close performance compared with the digital beamforming for the mm-Wave underground channel. It has been proved that the impact of hardware impairments such as additive distortion noise, vanishes asymptotically as the number of antennas grows large. The design of hybrid beamfomers and combiners matrices, is usually based on knowledge of the channel, in the next chapter we will study the mm-Wave MIMO underground channel estimation problem based on compressive sensing theorie.

# CHAPTER 4

# MM-WAVE UNDERGROUND CHANNEL ESTIMATION

## Contents

## 4.1 Introduction

In underground mine wireless communication systems, especially at the 60 GHz frequency band, the channel characteristics are a key factor which affects the mining applications [68]. One of the biggest impediments to mm-Wave underground propagation is the presence of materials with different dielectric properties, of irregularities along the walls, as well as the high path loss, which damages the communication scheme throughput enhancements [24]. To bridge the resulting significant link budget gap in such environments, directional multiple antennas have been recently adopted. Hence, finding techniques to increase the SE, while ensuring a viable QoS to face these channel adverse conditions, will necessitate a careful design of these communication systems for such high-stressed environment, along with a reliable channel estimation technique. In this chapter, the compressive sensing theory is used to accuratley estimate the mm-Wave underground channel with reduced overhead. For this, we present two new transceiver architectures for 5G network. This chapter puts forward the following main contributions:

- First, the STBC-FBMC/QAM system with two prototype filters is proposed for mm-Wave underground mine channel. In particular, an iterative algorithm for sparse channel estimation based on forward-backward (FB) processing is proposed, which can increase the accuracy of estimation and reduce the required pilot training without prior information of the sparsity level.

- Second, although mm-Wave MIMO systems promise to offer larger bandwidth and unprecedented peak data rates, their implementation in realistic scenarios faces some important issues that need to be solved. The inevitable imperfections, emerging from the transceiver hardware, make the mm-Wave MIMO underground mine channel estimation more challenging. To do that accurately, we develop an adaptive algorithm to estimate the mm-Wave MIMO underground channel parameters when the transmitter and receiver employ hybrid beamforming architectures and affected by the hardware impairments.

- Simulation results show that the proposed iterative FB channel estimation algorithm for STBC-FBMC system achieves a significative gain compared to the conventional OMP one. The results also illustrate that the presence of hardware impairments in mm-Wave MIMO underground system affect both the underground channel estimation and the achievable rate performance.

## 4.2 FBMC-STBC System Model

Consider a $2 \times 1$ STBC-FBMC system with two prototype filters and $K$ sub-carriers as illustrated in Figure 4.1, which is deployed over the mm-Wave underground channel. The measurements were performed using horn antennas at 40 m below the ground level [68]. At the transmitter side, the input data sequence $\mathbf{X}_{k,n}$ is firstly modulated using QAM scheme, and then separated into two groups $\mathbf{X}_{k,n}^{even}$ and $\mathbf{X}_{k,n}^{odd}$ of even and odd numbered sub-carrier symbols, respectively, prior to entering the space time encoders [49], which are given as:

$$\mathbf{X}_{k,n}^{even} = \mathbf{X}_{2\mathtt{w},n} \qquad k = 2\mathtt{w} \in \{0, 2, ..., K/2\}, \tag{4.1}$$

$$\mathbf{X}_{k,n}^{odd} = \mathbf{X}_{2\mathtt{w}+1,n} \qquad k = 2\mathtt{w}+1 \in \{1, 3, ..., K/2-1\}, \tag{4.2}$$

where $n = \{1, 2, ..., Ns\}$, with $Ns$ is the number of of transmitted FBMC symbols. After performing an IFFT operation, the QAM symbols of Alamouti scheme are multiplied by two different prototype filters $g_{2\mathtt{w},n}^{even}$ and $g_{2\mathtt{w}+1,n}^{odd}$, respectively, which can be obtained by the prototype function in the following way:

$$\begin{cases} g_{2\mathtt{w},n}^{even}(i) = g^{even}[i - n\frac{K}{2}]e^{j\frac{2\pi}{K}(2\mathtt{w})(i-\frac{L_f-1}{2})}, & \text{if} \quad k = 2\mathtt{w} \\ g_{2\mathtt{w}+1,n}^{odd}(i) = g^{odd}[i - n\frac{K}{2}]e^{j\frac{2\pi}{K}(2\mathtt{w}+1)(i-\frac{L_f-1}{2})}, & \text{if} \quad k = 2\mathtt{w}+1 \end{cases} \tag{4.3}$$

The two prototype filters are the $L_f = O\frac{K}{2}$ length, with $O$ is the overlapping factor, and which are designed to satisfy the mutually orthogonality conditions given by [88]:

$$\sum_{i=-\infty}^{\infty} g_{2\mathtt{w},n}^{even}(i) g_{2\mathtt{w}',n'}^{even*}(i) = \delta_{\mathtt{w},\mathtt{w}'}\delta_{n,n'}, \tag{4.4a}$$

$$\sum_{i=-\infty}^{\infty} g_{2\mathtt{w}+1,n}^{odd}(i) g_{2\mathtt{w}'+1,n'}^{odd*}(i) = \delta_{\mathtt{w},\mathtt{w}'}\delta_{n,n'}, \tag{4.4b}$$

$$\sum_{i=-\infty}^{\infty} g_{2\mathtt{w},n}^{even}(i) g_{2\mathtt{w}'+1,n'}^{odd*}(i) = 0 \tag{4.4c}$$

$$\sum_{i=-\infty}^{\infty} g_{2\mathtt{w},n}^{odd}(i) g_{2\mathtt{w}'+1,n'}^{even*}(i) = 0 \tag{4.4d}$$

where $\delta$ is the Dirac delta function.

The transmit symbols in the first time slot can be written as:

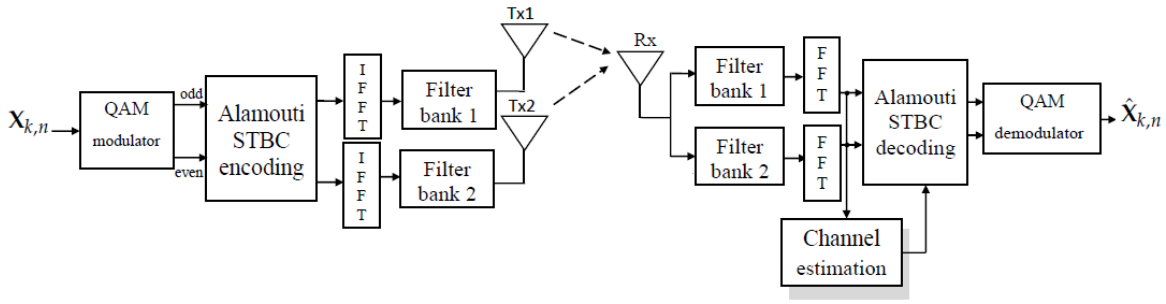


Figure 4.1: Block diagram of the adopted transceiver for mm-Wave $2 \times 1$ STBC-FBMC/QAM system.

$$A^{even}(i) = \sum_{\mathtt{w}=0}^{\mathtt{W}-1} \sum_{n=-\infty}^{\infty} g_{2\mathtt{w},n}^{even}(i) \mathbf{F}^H \mathrm{diag}(X_{2\mathtt{w},n}^{even}), \tag{4.5}$$

$$A^{odd}(i) = \sum_{\mathtt{w}=0}^{\mathtt{W}-1} \sum_{n=-\infty}^{\infty} g_{2\mathtt{w}+1,n}^{odd}(i) \mathbf{F}^H \mathrm{diag}(X_{2\mathtt{w}+1,n}^{odd}), \tag{4.6}$$

where $\mathbf{F}$ denotes an $\frac{K}{2} \times \frac{K}{2}$ unitary discrete Fourier transform (DFT) matrix, the index $i$ is the time sample, and $\mathtt{W} = K/2$ is the number of subcarriers. Therefore, under the orthogonality conditions given in (4.4), we can transmit QAM symbols in the FBMC system without intrinsic interference. Accordingly, the consecutive received signals, $\mathrm{r}_1$ and $\mathrm{r}_2$, are respectively given as:

$$\begin{aligned} \mathrm{r}_1 = \mathrm{r}(i) &= \mathrm{h}_1(l) \circledast A^{even}(i) + \mathrm{h}_2(l) \circledast A^{odd}(i+1) + \mathrm{n}_o(i), \\ \mathrm{r}_2 = \mathrm{r}(i+1) &= -\mathrm{h}_1(l) \circledast (A^{even}(i+1))^* + \mathrm{h}_2(l) \circledast (A^{odd}(i))^* + \mathrm{n}_o(i+1), \end{aligned} \tag{4.7}$$

where $\circledast$ is the convolution sign, $\mathrm{h}_1$ and $\mathrm{h}_2$ are the CIR of the transmit antennas 1 and 2, respectively, with length of $L$, and $\mathrm{n}_o$ is the AWGN with zero mean and variance of $\sigma_n^2$. At the receiver side, the received time domain FBMC signals, $\mathrm{r}_1$ and $\mathrm{r}_2$ passing through the underground channel, are matched by two different prototype filter banks $g_{2\mathtt{w}',n'}^{even}$ and $g_{2\mathtt{w}'+1,n'}^{odd}$, respectively, and then transformed to the frequency domain by applying the FFT operation. Hence, the corresponding signals at the two time slots, could be given as:

$$\mathrm{y}_1 = \mathrm{y}(t) = \mathbf{F} \sum_{i=-\infty}^{\infty} g_{2\mathtt{w}',n'}^{*even}(i) \mathrm{r}(i) = \mathrm{diag}(\mathrm{X}_{2\mathtt{w},n}^{even}) \mathbf{F}_L \mathrm{h}_1 + \mathrm{N}_1, \tag{4.8}$$

$$\mathrm{y}_2 = \mathrm{y}(t+1) = \mathbf{F} \sum_{i=-\infty}^{\infty} g_{2\mathtt{w}'+1,n'}^{*odd}(i) \mathrm{r}(i+1) = \mathrm{diag}(\mathrm{X}_{2\mathtt{w}+1,n}^{odd}) \mathbf{F}_L \mathrm{h}_2 + \mathrm{N}_2, \tag{4.9}$$

where $\mathrm{h}_1$ and $\mathrm{h}_2$ are the $\frac{K}{2}$-length CIR, which is generated by padding the $L$-length CIR with $\frac{K}{2} - L$ zeros as ($\mathrm{h} = [h_L, 0_{\frac{K}{2}-L}]$), with $L$ being the number of multipath components. Moreover, N is the AWGN vector with zero mean and unit variance elements, and $\mathbf{F}_L \in C^{\frac{K}{2}\times L}$ resulting from the extraction of the $\frac{K}{2}$ rows and the first $L$ columns from the $\frac{K}{2}$-dimension DFT matrix, given by:

$$\mathbf{F}_{\frac{K}{2}\times L} = \frac{1}{\sqrt{\frac{K}{2}}}\begin{bmatrix} 1 & w^{k_1} & \dots & w^{k_1(L-1)} \\ 1 & w^{k_2} & \dots & w^{k_2(L-1)} \\ \vdots & \vdots & \ddots & \vdots \\ 1 & w^{k_K} & \dots & w^{k_{\frac{K}{2}}(L-1)} \end{bmatrix} \tag{4.10}$$

where $w = e^{(-j2\pi/\frac{K}{2})}$. Letting $\mathbf{Y} = [\mathrm{y}_1, \mathrm{y}_2]^T$, we can write ( 4.8) and (4.9) in the compact form as:

$$\mathbf{Y} = \mathbf{\Phi h} + \mathbf{N}, \tag{4.11}$$

where $\mathbf{\Phi} = \left\{\mathrm{diag}(\mathrm{X}^{even}_{2\mathtt{w},n})\mathbf{F}_L, \mathrm{diag}(\mathrm{X}^{odd}_{2\mathtt{w}+1,n})\mathbf{F}_L\right\}$ is referred to as the measurement matrix, which is very important for guaranteeing a reliable underground channel estimator $\hat{\mathbf{h}}$ at the receiver and $\mathbf{h} = [\mathrm{h}_1, \mathrm{h}_2]^T \in C^{N_t L\times 1}$ is an aggregate CIR vector. The STBC-decoded symbols $\hat{X}^{even}_{2\mathtt{w},n}$ and $\hat{X}^{odd}_{2\mathtt{w}+1,n}$ could be expressed as:

$$\begin{aligned} \hat{X}^{even}_{2\mathtt{w},n} &= \hat{H}_1^* \mathrm{y}_1 + \hat{H}_2 \mathrm{y}_2^* \\ \hat{X}^{odd}_{2\mathtt{w}+1,n} &= \hat{H}_2^* \mathrm{y}_1 - \hat{H}_1 \mathrm{y}_2^* \end{aligned} \tag{4.12}$$

where $\hat{H}_1$ and $\hat{H}_2$ are the frequency domain channels of $\hat{h}_1$ and $\hat{h}_2$, respectively.

## 4.3 Compressive Sensing based-mm-Wave Underground Channel Estimation

In this section, we present a novel sparse channel estimation for STBC-FBMC system. We first present the pilots design, then we briefly introduce the conventional OMP based-underground channel estimation, followed by the proposed FB estimator to solve the channel estimation problem in the conventional OMP one.

### 4.3.1 Pilot Design of STBC-FBMC System

In the STBC-FBMC system model, the measurement matrix $\mathbf{\Phi}$ in (4.11) is very important for guaranteeing the reliable channel estimation. The pilots design is equivalent to designing the measurement matrix $\mathbf{\Phi}$, which lead to stable recovery of the channel matrix $\mathbf{h}$ in the proposed STBC-FBMC system. Figure 4.2 describes the pilot design for STBC-FBMC System, in which the pilot sequences is superimposed between Alamouti code block pairs without distorting the symmetry required. Accordingly, the two transmitted pilot sequences from two antennas are given as:

$$\mathbf{P}_1 = [p_1, -p_2^*, p_5, -p_6^*, ..., p_{K/2-1}, -p_{K/2}^*]^T, \tag{4.13}$$

$$\mathbf{P}_2 = [p_2, p_1^*, p_6, p_5^*, ..., p_{K/2}, p_{K/2-1}^*]^T, \tag{4.14}$$

where $P$ is the length of pilot sub-carriers. We only focus on the received pilots located at $p$, thus (4.11) can be then written as:

$$\mathbf{Y}_p = \mathbf{\Phi}_p \mathbf{h} + \mathbf{N}_p \tag{4.15}$$

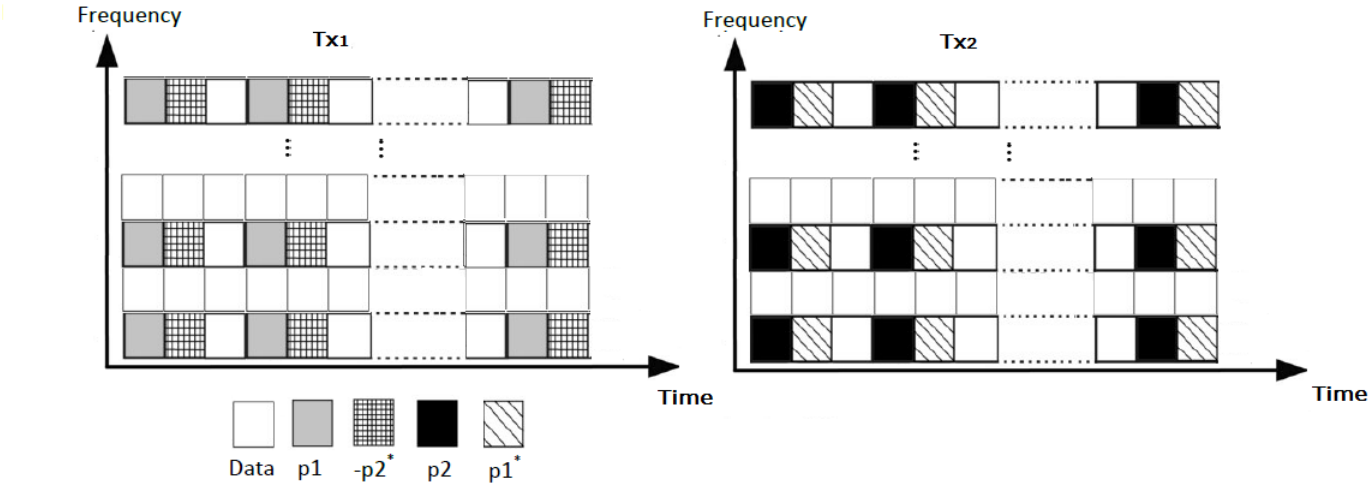


Figure 4.2: The pilots sequence for STBC-FBMC/QAM system.

where, $\mathbf{\Phi}_p \in C^{P \times L\,Nt}$ is the frequency domain measurement matrix determining the location of pilots with the required condition of identifiability $P \ll LN_t$.

### 4.3.2 Conventional OMP-based Channel Estimation

Before listing the detail of proposed FB-based mm-Wave underground channel estimator, we first introduce the conventional orthogonal matching pursuit (OMP) method developed in [70]. The measurements of mm-Wave underground mine channel showed that they normally have a limited number of paths due to the high free space path loss as illustrated in Figure 4.3. Due to the sparsity feature of the mm-Wave underground channel, OMP algorithm can be adapted to estimate the underground channel with a pilots sequence which is much lower than its length $L$ [69]. The key, is to first effectively estimate the location of the non-zero paths. To achieve this, **Algorithm 2** describe the process of estimating the underground channel under the assumption that the sparsity level $S_l$ is known. As a first step, OMP algorithm searches at each iteration the most correlated column among the remaining ones of $\mathbf{\Phi}_p$ with the current residual $\mathbf{r}$ by solving the optimization shown in Line 3, and appends the chosen column index into the set of chosen indices up to this stage (Line 5). Once all positions of the non-zero paths have been detected, the value of the channel coefficient matrix is estimated by solving the LS problem in Line 6. Finally, in Line 7, the contributions of the chosen column vectors to $\mathbf{Y}_p$ are subtracted to update the residual component $\mathbf{r}$. Our channel estimate is then $\hat{\mathbf{h}}$.

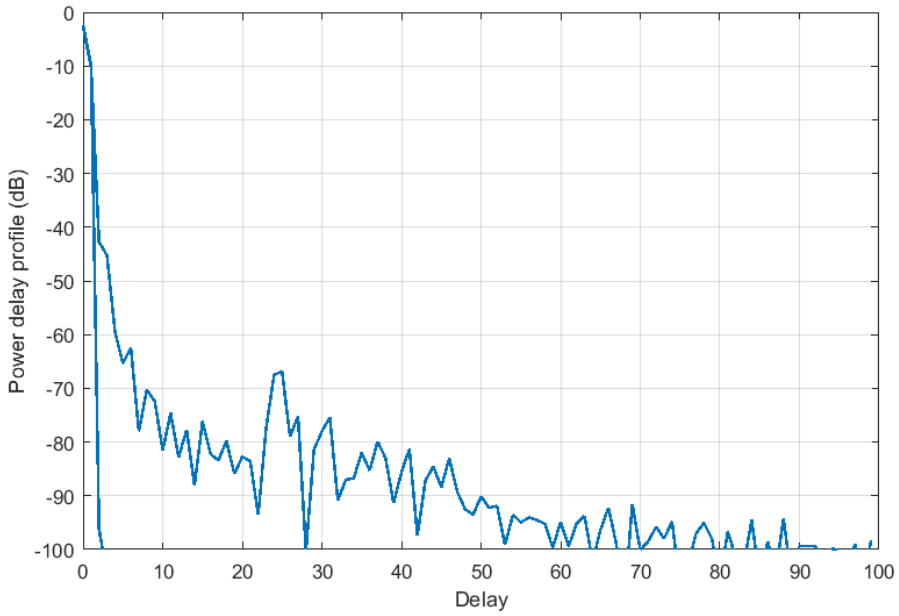


Figure 4.3: Illustration of the power delay profile of mm-Wave underground channel.

**Algorithm 3** OMP based-mm-Wave underground channel estimator

**Inputs:** $\mathbf{Y}_p$, $\mathbf{\Phi}_p$, $S_l$, Nt, $L$.

**Output:** the sparse estimate **h.**

**Initialisation :** $\mathbf{r}_0 = \mathbf{Y}_p$, $s = 0$, $\mathbf{h}^0 = 0$, $\Lambda^0 = \varnothing$

**for** $j = 1$**:** $N_r$ **do**

  **for** $s = 1$**:** $S_l N_t$ **do**

    $Z_s \longleftarrow$ **argmax** $\sum_{i=1}^{\mathbf{LNt}} \|\mathbf{\Phi}_p^H \mathbf{r}_s^j\|_2$**;**

  **end for**

  $\Lambda \longleftarrow \Lambda \bigcup Z_s$;

  $\mathbf{h}_\Lambda^{(s)} \longleftarrow \mathbf{\Phi}_\Lambda^\dagger \mathbf{Y}^j$ **and** $\mathbf{h}_\Lambda^{(s)} \longleftarrow 0$**;** % **LS estimation.**

  $\mathbf{r}_s \longleftarrow \mathbf{Y}^j - \mathbf{\Phi}_P \mathbf{h}_\Lambda^{(s)}$; % **Update Residual.**

**end for**

$\hat{\mathbf{h}} \longleftarrow \mathbf{h}^{(s)}$**;** % **Obtain the final channel estimation.**

### 4.3.3 Proposed FB Underground Channel Estimator

The conventional OMP has two major problems. The first problem is its inability to identify the correct sparse index position of the channel. The second is how to reduce the random error of the correlation matrix, which may result in performance degradation and high computational complexity. In this chapter, we propose a new iterative algorithm using a forward and backward processing for channel estimation based on [89], by exploiting the time domain sparsity feature of the mm-Wave underground mine channel. The algorithm is represented in details in **Algorithm 3**. The proposed FB approach combines the forward and backward processing to compute the correlation matrix between the received signal and the measurement matrix, in which we can examine the structure of correlation matrix formed by the forward step, and found a reduced computational complexity in channel estimation. In the other hand, backward step can potentially correct any errors caused by earlier forward step and avoid maintaining a large number of basis functions. A schematic diagram of the FB algorithm is depicted in Figure 4.4.

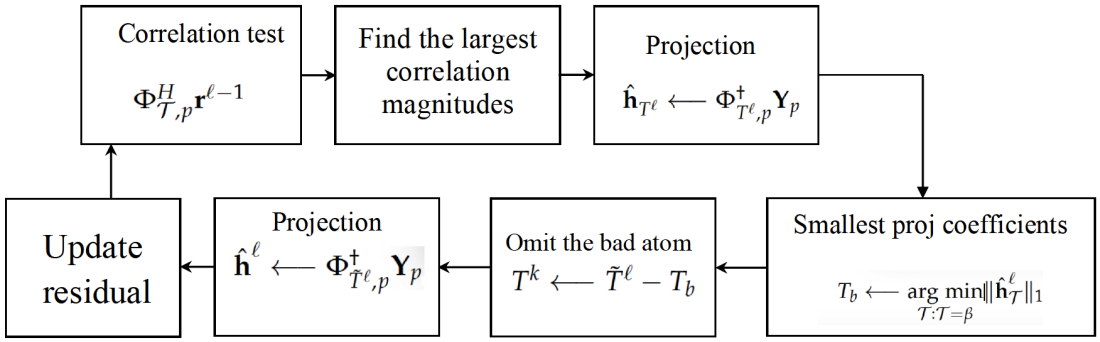


Figure 4.4: Description of the iterative FB algorithm.

In **Algorithm 3**, the process is mainly divided into the two steps forward and backward. At each iteration, the forward step aims at building-up the extended support estimate $\tilde{T}^\ell$. This is achieved by selecting at each time the $\alpha$ indices which yield the greatest correlation with the residual signal $\mathbf{r}$, among the remaining ones in the measurement matrix $\mathbf{\Phi}_p$ (step 3). Subsequently, the LS estimation is performed (step 4). However, unlike OMP algorithm, which directly use $\tilde{T}^\ell$ to reconstruct the sparse channel, the proposed algorithm utilizes $\tilde{T}^\ell$ as the initialization for the backward step process, which prunes the support estimate $\tilde{T}^\ell$ by removing the $\beta$ indices corresponding to the minimum magnitude. Consequently, the size of the estimated support set $T^\ell$ is reduced to the length $\alpha - \beta$ in each iteration (step 6). This step gives the pro-

**Algorithm 4** Proposed FB algorithm based-channel estimation approach

**Inputs:** $\mathbf{Y}_P$, $\mathbf{\Phi}_p$, $\mathrm{N}_t$, $\alpha$, $\beta$, $\varepsilon$, $\ell_{\max}$.

**Output:** The estimated channel $\hat{\mathbf{h}}$.

**Initialization** : The initial residual $\mathbf{r}^0 = \mathbf{Y}_p$, index set $T^0 = \emptyset$, $\ell = 0$

1: **while** $\| \mathbf{r}^\ell \|_2 \geq \| \varepsilon \mathbf{Y}_p \|_2$ **do**

2: $\ell = \ell + 1$

**Forward step**

3: $\tilde{T}^\ell \longleftarrow \tilde{T}^{\ell-1} \bigcup \arg\max_{\mathcal{T}:\mathcal{T}=\alpha} \sum_{\mathcal{T}=1}^{\mathrm{LN}_t} \|\Phi_{\mathcal{T},p}^H \mathbf{r}^{\ell-1}\|_1$;

4: Define $\hat{\mathbf{h}}^\ell \longleftarrow \Phi_{\tilde{T}^\ell,p}^\dagger \mathbf{Y}_p$; % LS estimation.

**Backward step**

5: $T_b \longleftarrow \arg\min_{\mathcal{T}:\mathcal{T}=\beta} \|\hat{\mathbf{h}}_{\mathcal{T}}^\ell\|_1$;

6: $T^\ell \longleftarrow \tilde{T}^\ell - T_b$ ; % Omit bad atom

7: $\hat{\mathbf{h}}_{T^\ell} \longleftarrow \Phi_{T^\ell,p}^\dagger \mathbf{Y}_p$; % orthogonal projection

8: $\mathbf{r}^\ell \longleftarrow \mathbf{Y}_p - \Phi_{T^\ell,p} \hat{\mathbf{H}}_{T^\ell}$; % Update residual.

9: **if** $|T|^\ell \geq \ell_{\max} \times N_t$ **then**

10: **break**

11: **end if**

12: **end while**

13: $\hat{\mathbf{h}} \longleftarrow 0$;

14: $\hat{\mathbf{h}} \longleftarrow \hat{\mathbf{h}}_{T^\ell}$; % Recovered sparse channel.

posed algorithm the ability to correct the errors generated in the first step. The sparse channel estimate $\hat{\mathbf{h}}^{\ell}$ is finally obtained by computing the orthogonal projection of $\mathbf{Y}_p$ onto the new support estimate, to produce an accurate recovery of the sparse channel components (step 7). The residual component is continuously updated until reaching the defined condition $\| \mathbf{r}^{\ell} \| \geq \| \varepsilon \mathbf{Y}_p \|$, where $\varepsilon$ is the predetermined threshold. If the stopping criteria is not met, a forcing stop is set after reaching a maximum number of iterations of $\ell_{\max} \times Nt$. The important condition in the performance of the proposed FB algorithm is to choose $\beta < \alpha$.

## 4.4 Mm-Wave Hybrid Underground MIMO System

We consider a hybrid mm-Wave MIMO underground system, comprising $N_t$ transmit antennas and $\mathrm{N_{RF}}$ RF chains to convey $N_s$ data streams over the underground channel simultaneously, while the receiver equipped with $N_r$ antennas and $\mathrm{N_{RF}}$ RF chains, as shown in Figure 4.5. The hybrid beamformer and combiner structure used is similar to those illustrated in the previous chapter. In order to transmit a signal, the transmitter applies two consecutive beamforming operations $\mathbf{F}_{\mathrm{BB}} \in \mathbb{C}^{N_{\mathrm{RF}} \times N_s}$ and $\mathbf{F}_{\mathrm{RF}} \in \mathbb{C}^{N_t \times N_{\mathrm{RF}}}$ denote as the baseband beamformer and analog beamformer, respectively. The residual transceiver hardware impairments can be modeled as additive distortion noise, which has been verified in [26], the received signal can be written as:

$$\mathbf{r} = \mathbf{H}(\mathbf{F}_{\mathrm{T}}\mathbf{s} + \boldsymbol{\eta}_t) + \boldsymbol{\eta}_r + \mathbf{n}, \tag{4.16}$$

where $\mathbf{s} \in \mathbb{C}^{N_s \times 1}$ is the transmitted symbol on the beamforming matrix, such that $\mathrm{E}[\mathbf{s}\mathbf{s}^H] = \frac{P_s}{N_s}\mathbf{I}_{N_s}$, with $P_s$ is the total transmit power at the transmitter, $\mathbf{F}_{\mathrm{T}} = \mathbf{F}_{\mathrm{RF}}\mathbf{F}_{\mathrm{BB}}$ is the hybrid beamformer matrix, $\mathbf{H} \in \mathbb{C}^{N_r \times N_t}$ is the mm-Wave underground channel matrix which capture the joint effect of path loss and multi-path fading, the additive distortion noise $\boldsymbol{\eta}_t, \boldsymbol{\eta}_r$ describe the residual transceiver impairments in the transmitter and receiver hardware, respectively, and $\mathbf{n} \sim CN(0, \sigma_n^2)$ represents the complex Gaussian noise. Similarly, at the receiver, the combiner $\mathbf{W}_{\mathrm{T}}$ also consists of RF and baseband combiners represented by $\mathbf{W}_{\mathrm{RF}} \in \mathbb{C}^{N_r \times N_{\mathrm{RF}}}$ and $\mathbf{W}_{\mathrm{BB}} \in \mathbb{C}^{N_{\mathrm{RF}} \times N_s}$, respectively

$$\mathbf{y} = \mathbf{W}_{\mathrm{T}}^H\mathbf{H}(\mathbf{F}_{\mathrm{T}}\mathbf{s} + \boldsymbol{\eta}_t) + \mathbf{W}_{\mathrm{T}}^H\boldsymbol{\eta}_r + \mathbf{W}_{\mathrm{T}}^H\mathbf{n}, \tag{4.17}$$

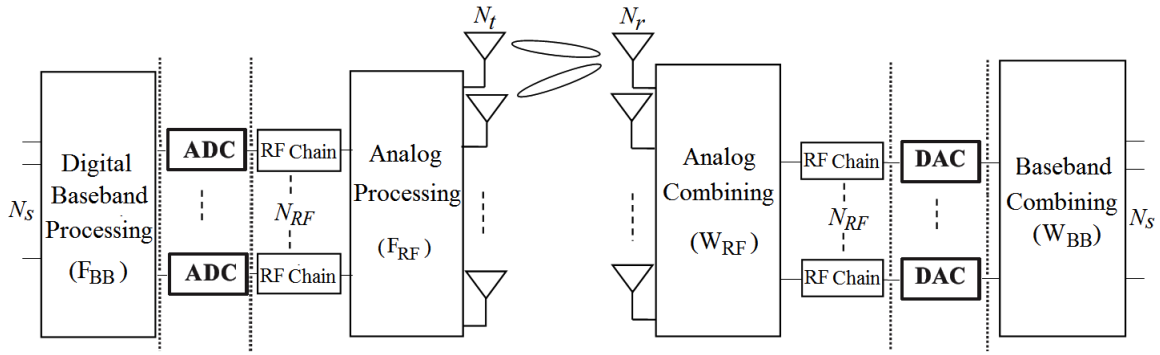


Figure 4.5: Transceiver structure of underground MIMO system based-hybrid beamforing structure.

In order to design the performance of large MIMO system in underground environment, we generate a virtual large MIMO channel matrix based on channel measurements obtained at different locations within an underground mine gallery, and at the same time a virtual directions is ed. The mm-Wave underground channel representation **H** in angle-domain can therefore be represented as:

$$\mathbf{H} = \sum_{l=0}^{L-1} \mathrm{h}_l \mathbf{a}_t(\theta_l)\mathbf{a}_r^H(\phi_l), \tag{4.18}$$

where $\mathrm{h}_l$ is the complex gain of the $l^{th}$ path obtained by measurement [68], and $\theta_l \in [0, 2\pi]$ and $\phi_l \in [0, 2\pi]$ are the $l^{th}$ path's virtual AoD/AoA of the transmitter and the receiver, respectively. For simplicity, we use the ULAs, $\mathbf{a}_t$ and $\mathbf{a}_r$ can be defined as:

$$\mathbf{a}_t(\theta_l) = [1, e^{j2\pi d \sin(\theta_l)/\lambda}, ..., e^{j2\pi(\mathrm{N_t}-1)d \sin(\theta_l)/\lambda}]^T, \tag{4.19}$$

$$\mathbf{a}_r(\phi_l) = [1, e^{j2\pi d \sin(\phi_l)/\lambda}, ..., e^{j2\pi(\mathrm{N_r}-1)d \sin(\phi_l)/\lambda}]^T, \tag{4.20}$$

where $\lambda$ is the wavelength of the carrier frequency, and $d$ is the antenna spacing. An equivalent representation of the channel is given by:

$$\mathbf{H} = \mathbf{A}_r \mathrm{diag}(\mathbf{h})\mathbf{A}_t^H, \tag{4.21}$$

where

$$\mathbf{h} = [h_1, h_2, ..., h_L]^T, \tag{4.22}$$

$$\mathbf{A}_t = [\mathrm{a}_t(\theta_1), \mathrm{a}_t(\theta_2), ..., \mathrm{a}_t(\theta_L)], \tag{4.23}$$

$$\mathbf{A}_r = [\mathrm{a}_r(\phi_1), \mathrm{a}_r(\phi_2), ..., \mathrm{a}_r(\phi_L)], \tag{4.24}$$

where $\mathbf{A}_t \in \mathbb{C}^{N_t \times L}$ and $\mathbf{A}_r \in \mathbb{C}^{N_r \times L}$ are the beamforming dictionary matrices at the transmitter and the receiver, respectively. In vector form, (4.21) can be rewritten as:

$$\mathrm{vec}(\mathbf{H}) = (\mathbf{A}_t^H \otimes \mathbf{A}_r).\mathrm{vec}(\mathbf{h}), \tag{4.25}$$

where the equality follows from the identity $\mathrm{vec}(\mathbf{ABC}) = (\mathbf{C}^H \otimes \mathbf{A}).\mathrm{vec}(\mathbf{B})$.

## 4.5 Hardware impaired MIMO Underground Channel Estimation

One of the most immediate challenges faced by mm-Wave channel estimation comes from signal propagation losses inherent in the frequency range and the large antenna arrays. Because of these losses, the omnidirectional transmission of any pilot signal results in very low received SNRs, which ultimately leads to less accurate channel estimation. As such, the pilot signals used in mm-Wave channel estimation will also require beamforming, in order to be received with a sufficiently high SNR. This means that narrower beams must be used to scan the mm-Wave channel in search of suitable propagation paths. The second challenge stems from the use of inexpensive hardware components in large MIMO arrays, which induce hardware impairments problem. In this section, we investigate the impact of hardware impairments on the channel estimation phase when using a hierarchical multi-resolution codebook method to construct the training beamforming vectors. Motivated by the sparse nature of mm-Wave channel in the space domain, estimating this channel is equivalent to estimating the AoD, AoA, and then estimating the path gain associated with each pair of AoD and AOA.

### 4.5.1 Sparse Formulation Problem

During the training period, we assume the transmitter employs a beamforming vector $\mathbf{f}_{\mathrm{p}}$, while the receiver uses a combining vector $\mathbf{w}_{\mathrm{p}}$ to combine the received signal, the resulting signal, under the impact of hardware impairements, can be written as:

$$y_{\mathrm{q,p}} = \mathbf{w}_{\mathrm{q}}^H \mathbf{H}(\mathbf{f}_{\mathrm{p}} \mathrm{s}_{\mathrm{p}} + \boldsymbol{\eta}_t) + \mathbf{w}_{\mathrm{q}}^H \boldsymbol{\eta}_r + \mathbf{w}_{\mathrm{q}}^H \mathrm{n}_{\mathrm{q,p}}, \tag{4.26}$$

where $\mathrm{s}_{\mathrm{p}}$ is the transmitted symbol on the beamforming vector $\mathbf{f}_{\mathrm{p}}$, such that $\mathbb{E}[\mathrm{s}_{\mathrm{p}} \mathrm{s}_{\mathrm{p}}^H] = P$, with $P$ being the average power used per transmission in the training phase. If $M_s^r$ such measurements are performed by the receiver vectors $\mathbf{w}_{\mathrm{q}}$; $q = 1, 2, ..., M_s^r$ at $M_s^r$ successive instants to detect the signal transmitted over the beamforming vector $\mathbf{f}_{\mathrm{p}}$, the resulting vector will be:

$$\mathbf{y}_p = \mathbf{W}_{\mathrm{T}}^H \mathbf{H}(\mathbf{f}_{\mathrm{p}} \mathrm{s}_{\mathrm{p}} + \boldsymbol{\eta}_t) + \mathbf{W}_{\mathrm{T}}^H \boldsymbol{\eta}_r + \mathrm{diag}(\mathbf{W}_{\mathrm{T}}^H [\mathrm{n}_{1,p}, ..., \mathrm{n}_{\mathrm{M}_s^t,p}]), \tag{4.27}$$

where $\mathbf{W}_{\mathrm{T}} = [\mathbf{w}_1, ..., \mathbf{w}_{\mathrm{M}_s^r}]$ is the $N_r \times \mathrm{M}_s^t$ combining matrix. Similarly, if the transmitter employs $M_s^t$ such beamforming vectors $\mathbf{f}_{\mathrm{p}}$; $p = 1, 2, ..., M_s^t$ at $M_s^t$ successive time slots, and the receiver uses the same measurement matrix $\mathbf{W}_{\mathrm{T}}$ to combine the received signal, considering all transmitted symbols have the same power, the resultant matrix can then be written by concatenating the $M_s^t$ processed vectors $\mathbf{y}_p$:

$$\mathbf{Y} = \sqrt{P} \mathbf{W}_{\mathrm{T}}^H \mathbf{H}(\mathbf{F}_{\mathrm{T}} + \boldsymbol{\eta}_t) + \mathbf{W}_{\mathrm{T}}^H \boldsymbol{\eta}_r + \mathbf{Q} \tag{4.28}$$

where $\mathbf{F}_{\mathrm{T}} = [\mathbf{f}_1, ..., \mathbf{f}_{\mathrm{M}_s^t}]$ is the $N_t \times \mathrm{M}_s^t$ beamforming matrix used by the transmitter, $\mathbf{Q}$ is an $M_s^r \times M_s^t$ noise matrix given by concatenating the MBS noise vectors. To formulate the sparse channel estimation problem, it is necessary to vectorize the received matrix $\mathbf{Y}$ to $\mathbf{y}_v$ as follows:

$$\begin{aligned} \mathbf{y}_v &= \sqrt{P}\mathrm{vec}(\mathbf{W}_{\mathrm{T}}^H \mathbf{H}(\mathbf{F}_{\mathrm{T}} + \boldsymbol{\eta}_t)) + \mathrm{vec}(\mathbf{W}_{\mathrm{T}}^H \boldsymbol{\eta}_r) + \mathrm{vec}(\mathbf{n}) \\ &= \sqrt{P}(\mathbf{W}_{\mathrm{T}}^H \otimes (\mathbf{F}_{\mathrm{T}} + \boldsymbol{\eta}_t))\mathrm{vec}(\mathbf{H}) + \mathbf{W}_{\mathrm{T}}^H \boldsymbol{\eta}_r + \mathbf{n}_v \\ &= \sqrt{P}(\mathbf{W}_{\mathrm{T}}^H \otimes (\mathbf{F}_{\mathrm{T}} + \boldsymbol{\eta}_t))(\mathbf{A}_t^H \otimes \mathbf{A}_r)\boldsymbol{\alpha} + \mathbf{W}_{\mathrm{T}}^H \boldsymbol{\eta}_r + \mathbf{n}_v \end{aligned} \tag{4.29}$$

where $(\mathbf{A}_t^H \otimes \mathbf{A}_r)$ is the $N_t N_r \times L$ matrix in which each column has the form $(\mathrm{a}_t^H(\theta_l) \otimes \mathrm{a}_r(\phi_l))$, with $l = 1, ..., L$. To complete the problem formulation, we quantize the AoAs and AoDs. Its assume that the AoAs, and AoDs are taken from a uniform grid of $N_Q$ points, with $N_Q \gg L$, i.e., we assume that $\mathrm{a}_t(\theta_l), \mathrm{a}_r(\phi_l) \in \left\{0, \frac{2\pi}{N_Q}, ..., \frac{2\pi N_Q - 1}{N_Q}\right\}$. Equation (4.29) can be written as:

$$\mathbf{y}_v = \sqrt{P_s}(\mathbf{W}_{\mathrm{T}}^H \otimes (\mathbf{F}_{\mathrm{T}} + \boldsymbol{\eta}_t))\mathbf{A}_D\boldsymbol{\alpha} + \boldsymbol{n}_Q \tag{4.30}$$

where $\mathbf{A}_D$ is the $N_t N_r \times N_Q^2$ dictionary matrix that consists of the $N_Q^2$ column vectors of the form $(\mathrm{a}_t^H(\theta_v) \otimes \mathrm{a}_r(\phi_u))$, with $\theta_v$, and $\phi_u$ is the $v^{th}$, and $u^{th}$ points, respectively, of the angles uniform grid, i.e., $\theta_v = \frac{2\pi v}{N_Q}$, $v = 1, ..., N_Q - 1$ and $\phi_u = \frac{2\pi u}{N_Q}$, $u = 1, ..., N_Q - 1$. $\boldsymbol{\alpha}$ is an $N_Q^2 \times 1$ vector which carries the path gains of the corresponding quantized directions, and $\boldsymbol{n}_Q = \mathbf{W}_{\mathrm{T}}^H \boldsymbol{\eta}_r + \mathbf{n}_v$ is the equivalent noise. Note that detecting the columns of $\mathbf{A}_D$ directly implies the detection of the AoAs and AoDs of the dominant paths of the channel. The path gains can be also determined by calculating the values of the corresponding elements in $\boldsymbol{\alpha}$.

The formulation of the vectorized received signal $\mathbf{y}_v$ in (4.30) represents a CS formulation of the channel estimation problem as $\boldsymbol{\alpha}$ has only $L$ non-zero elements and $L \ll N_Q^2$. Based on the problem formulation in (4.29), CS concept can be used to solve the estimation problem of the to quantized AoAs/AoDs. If we define the sensing matrix as $\boldsymbol{\Psi} = (\mathbf{W}_{\mathrm{T}}^H \otimes (\mathbf{F}_{\mathrm{T}} + \boldsymbol{\eta}_t))\mathbf{A}_D$, the objective of the CS algorithms will be to efficiently design the sensing matrix $\boldsymbol{\Psi}$ to guarantee the recovery of the $L$ non-zero elements of the vector $\boldsymbol{\alpha}$ with minimal measurements. One common criterion for that is the restricted isometry property (RIP), which requires the matrix $\boldsymbol{\Psi}^H\boldsymbol{\Psi}$ to be close to diagonal on average [90].

There are two categories in CS theory: standard CS and adaptive CS, and because the adaptive CS algorithms yield better performance than standard CS tools at low SNR, which is the typical case at mm-Wave systems before beamforming, and rely on successive bisections that can be used in the design of the training beamforming vectors [91], we focus on the adaptive CS tools that use the multi-resolution hierarchical codebook to design of the training beamforming vectors.

### 4.5.2 Adaptive Compressed Sensing Solution

In the adaptive CS [91], the training process is divided into a number of stages. The training precoding and combining matrices used at each stage are not determined a priori, but rather depend on the output of the earlier stages. More specifically, if the training process is divided into $Z$ stages, then the vectorized received signals of these stages are:

$$\begin{aligned}
\mathbf{y}^{(1)} &= \sqrt{P^{(1)}}\left((\mathbf{F}_{\mathrm{T}}^{(1)} + \boldsymbol{\eta}_t^{(1)})\mathbf{A}_t^H \otimes \mathbf{W}_{\mathrm{T}}^{H(1)}\mathbf{A}_r\right)\boldsymbol{\alpha} + \boldsymbol{n}_Q^{(1)} \\
\mathbf{y}^{(2)} &= \sqrt{P^{(2)}}\left((\mathbf{F}_{\mathrm{T}}^{(2)} + \boldsymbol{\eta}_t^{(2)})\mathbf{A}_t^H \otimes \mathbf{W}_{\mathrm{T}}^{H(2)}\mathbf{A}_r\right)\boldsymbol{\alpha} + \boldsymbol{n}_Q^{(2)} \\
&\vdots \\
\mathbf{y}^{(Z)} &= \sqrt{P^{(Z)}}\left((\mathbf{F}_{\mathrm{T}}^{(Z)} + \boldsymbol{\eta}_t^{(Z)})\mathbf{A}_t^H \otimes \mathbf{W}_{\mathrm{T}}^{H(Z)}\mathbf{A}_r\right)\boldsymbol{\alpha} + \boldsymbol{n}_Q^{(Z)}
\end{aligned} \tag{4.31}$$

The design of the $z^{th}$ stage training precoders and combiners, $\mathbf{F}_{\mathrm{T}}^{(z)}$, $\mathbf{W}_{\mathrm{T}}^{(z)}$ are adaptively designed based on the bisection concept depends on $\mathbf{y}^{(z-1)}$. In particular, the algorithm starts initially by dividing the vector $\boldsymbol{\alpha}$ in (4.31) into a number of partitions, which equivalently divides the AoAs/AoDs into a number of intervals, and design the training precoding and combining matrices of the first stage, $\mathbf{F}_{\mathrm{T}}^{(1)}$, $\mathbf{W}_{\mathrm{T}}^{(1)}$. The received signal $\mathbf{y}^{(1)}$ is then used to determine the partitions that are highly likely to have non-zero elements which are further divided into smaller partitions in the next stages until detecting the non-zero elements, the AoAs/AoDs, with the required resolution. If the number of precoding vectors used in each stage of the adaptive algorithm equals $\mathcal{K}$, where $\mathcal{K}$ is a design parameter, then the number of adaptive stages needed to detect the AoAs/AoDs with a resolution $\frac{2\pi}{N_Q}$ is $Z = \log_{\mathcal{K}} N_Q$, which we assume to be integer for ease of exposition. We will focus in the following section on the design of a multi-resolution beamforming codebook which is essential for the proper operation of the adaptive channel estimation algorithm.

### 4.5.3 Hybrid beamforming Based Multi-Resolution Hierarchical Codebook

The hybrid codebook contains the beamforming and the combining matrices $\mathcal{F}$ and $\mathcal{W}$ used by the transmitter and the receiver in the first stage of the channel estimation to recover the emitted signal at low SNR. By considering the RF impairments, the construction of the hybrid beamforming and combining matrices has a very-low complexity, and outperforms the analog-only beamforming codebooks thanks to its additional digital processing layer. The hierarchical beamforming codebook is composed of $Z$ levels, $\mathcal{F}_z; z = 1, 2, ..., Z$, where each level contains beamforming vectors

with a certain beamwidth that covers certain angular regions. Figure 4.6 presents the first three levels of an example codebook with a resolution parameter $N_Q = 256$, and $\mathcal{K} = 2$ beamforming vectors of each codebook level. In each codebook level, the beamforming vectors are divided into $\mathcal{K}^{z-1}$ subsets, which contain $\mathcal{K}$ beamforming vectors. Each subset $k$ is associated with a unique interval of the AoDs equal to $\{\frac{2\pi u}{N_Q}\}_{u \in I_{(z,k)}}$, where $I_{(z,k)} = \{\frac{(k-1)N_Q}{\mathcal{K}^{z-1}}, ..., \frac{kN_Q}{\mathcal{K}^{z-1}}\}$. This interval is further divided into $\mathcal{K}$ intervals in the next level, and each of the $\mathcal{K}$ beamforming vectors in this subset is designed so as to have an almost equal projection on the vectors $a_t(\theta_v)$,where $v$ is in the the sub-interval covered by this beamforming vector, and zero projection on the array response vectors corresponding to other angles. Physically, this implies the implementation of a beamforming vector with a certain beamwidth determined by these sub-intervals, and steered in pre-defined directions as illustrated in Figure 4.7.

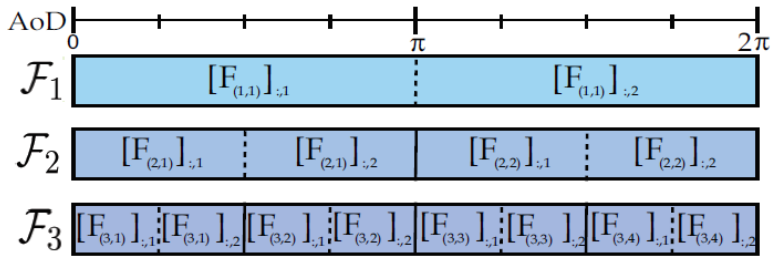


Figure 4.6: An example of the structure of a multi-resolution codebook.

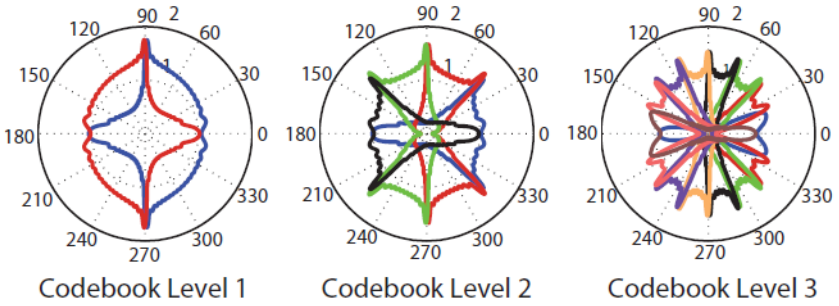


Figure 4.7: The resulting beam patterns of the beamforming vectors in the first three codebook levels of an example hierarchical codebook.

In each codebook level $z$, and subset $k$, the beamforming vectors $[\mathbf{F}_{z,k}]_{:,m}, m = 1...\mathcal{K}$ are designed such that:

$$[\mathbf{F}_{z,k}]^{*}_{:,m}\mathbf{a}_t(\theta_v) = \begin{cases} C_s, & \text{if } v \in J_{(z,k,m)} \\ 0, & \text{if } v \notin J_{(z,k,m)}. \end{cases} \tag{4.32}$$

where $J_{(z,k,m)} = \{\frac{N}{\mathcal{K}^z}(\mathcal{K}(k-1)+m-1)+1+...+\frac{N}{\mathcal{K}^z}(\mathcal{K}(k-1)+m)\}$ defines the intervals of AoDs associated with the beamforming vector $[\mathbf{F}_{(z,k)}]_{:,m}$ , and $C_s$ is a normalization constant that satisfies $\| \mathbf{F}_{(z,k)} \|_F = \mathcal{K}$. Therefore, the beamforming vectors desired are the solution of:

$$\mathbf{A}_t^H \mathbf{F}_{(z,k)} = C_s \mathbf{G}_{(z,k)} \tag{4.33}$$

where $\mathbf{G}_{(z,k)}$ is an $N \times K$ matrix where each column $m$ containing 1 in the locations $u$; $u \in J_{(z,k,m)}$, and zeros in the other locations. Now, we note that the transmitter AoDs matrix $\mathbf{A}_t^H$ is an over-complete dictionary with $N \geq N_t$. The approximate solution of (4.33) is given by:

$$\mathbf{F}_{(z,k)} = C_s(\mathbf{A}_t\mathbf{A}_t^H)^{-1}\mathbf{A}_t\mathbf{G}_{(z,k)} \tag{4.34}$$

As the beamforming matrix $\mathbf{F}_{(s,k)} = \mathbf{F}_{RF,(s,k)}\mathbf{F}_{BB,(z,k)}$, and each beamforming vector will be individually used in a certain time instant. The design of beamfoming vectors is detailled in Chapter 3.

### 4.5.4 Adaptive Estimation Algorithm for Mm-Wave Underground Channel

By considering the sparse channel estimation problem formulated in (4.30), an adaptive estimation algorithm for mm-Wave underground channel is considered to quickly search out the dominant channel direction for multi-path underground channel. The **Algorithm 5** makes $\mathcal{K}L$ outer iterations, which operates as follows:

**Algorithm 5** Underground Channel Estimation Algorithm

**Inputs:** $\mathcal{F}$, $\mathcal{W}$, $L$, $N_Q$, $\mathcal{K}$ beamforming

**Output:** AoDs, AoAs, and path gains for the L dominant paths.

**Initialization** : $\mathbf{M}^t_{(1,1)} = \{1, ..., 1\}$, $\mathbf{M}^r_{(1,1)} = \{1, ..., 1\}$, $Z = \log_{\mathcal{K}}(N_Q/L)$,

**for** $l \leq L$

**for** $z \leq Z$

**for** $m_t \leq \mathcal{K}L$

Tx uses $\mathcal{K}$ beamforming vectors of level $z$ of $[\mathbf{F}_{z,\mathbf{M}^t_{(l,z)}}]_{:,n_t}$

**for** $m_r \leq \mathcal{K}L$

Rx uses $\mathcal{K}$ beamforming vectors of level $z$ of $[\mathbf{W}_{z,\mathbf{M}^r_{(l,z)}}]_{:,n_r}$

$\mathbf{y}_{m_r} = \sqrt{P}[\mathbf{W}_{z,\mathbf{M}^r_{(l,z)}}]_{:,n_r}\mathbf{H}([\mathbf{F}_{z,\mathbf{M}^t_{(l,z)}}]_{:,n_t} + \boldsymbol{\eta}_t) + [\mathbf{W}_{z,\mathbf{M}^r_{(l,z)}}]_{:,n_r}\boldsymbol{\eta}_r + \mathbf{N}$,

$\mathbf{Y}^{(z)} = [\mathbf{y}_1, \mathbf{y}_2, ..., \mathbf{y}_K]^T$

**for** $p = 1 \leq l - 1$

$\boldsymbol{g} = \mathbf{F}_{(z,\mathbf{M}^t_{(l,z)})}[\mathbf{A}]_{:,\mathbf{M}^t_{(l,Z+1)}(1)} \odot \mathbf{W}_{(z,\mathbf{M}^r_{(l,z)})}[\mathbf{A}]_{:,\mathbf{M}^r_{(l,Z+1)}(1)}$

$\mathbf{Y}^{(z)} = \mathbf{Y}^{(z)} - (\mathbf{Y}^{(z)})^H \boldsymbol{g}(\boldsymbol{g}^H\boldsymbol{g})\boldsymbol{g}$

$\mathbf{Y}$ = matrix($\mathbf{Y}^{(z)}$) Return $\mathbf{Y}^{(z)}$ to the matrix form

$[m_t^*, m_r^*] = \arg\max \quad [\mathbf{Y} \odot \mathbf{Y}^*]$

$\mathbf{M}^t_{(l,z+1)}(1) = \mathcal{K}(m_t^* - 1) + 1$, $\mathbf{M}^r_{(l,z+1)}(1) = \mathcal{K}(m_r^* - 1) + 1$

**for** $p = 1 \leq l - 1$

$\mathbf{M}^t_{(l,z+1)}(p) = \mathbf{M}^t_{(p,z+1)}(1)$, $\mathbf{M}^r_{(l,z+1)}(p) = \mathbf{M}^r_{(p,z+1)}(1)$

$\hat{\theta}_l = \theta_{\mathbf{M}^t_{(p,Z+1)}(1)}$, $\hat{\phi}_l = \phi_{\mathbf{M}^r_{(p,Z+1)}(1)}$

$\boldsymbol{g} = \mathbf{F}_{(z,\mathbf{M}^t_{(l,z)})}[\mathbf{A}]_{:,\mathbf{M}^t_{(l,Z+1)}(1)} \odot \mathbf{W}_{(z,\mathbf{M}^r_{(l,z)})}[\mathbf{A}]_{:,\mathbf{M}^r_{(l,Z+1)}(1)}$

$\hat{\boldsymbol{\alpha}} = \sqrt{\frac{\rho}{P_{(Z)}G_{(Z)}}}\frac{\mathbf{Y}^{(z)}\boldsymbol{g}}{\boldsymbol{g}^*\boldsymbol{g}}$

1. In the initial stage of estimation, the Tx uses the $\mathcal{K}L$ training beamforming vectors of the first level of the codebook $\mathcal{F}$. For each of those vectors, the Rx uses the $\mathcal{K}L$ combining vectors of the first level of $\mathcal{W}$ to combine the received signal.

2. After the $\mathcal{K}L$ precoding-combining operations of this stage, the Rx selects a beam index that achieves the largest received signal power. As each one of the precoding/combining vectors is associated with a certain interval of the quantized AoA/AoD, the operation of the first stage divides the AoA and AoD interval into $\mathcal{K}L$ sub-intervals each. Hence, the selection of the maximum power received signal implies the selection of the dominant paths of the channel, and consequently the interval of the quantized AoA/AoD.

3. This process is repeated until we reach the required AoD resolution, and only one path is estimated at each iteration.

4. The trajectories used by the Tx to detect the first path is stored in the matrix $\mathbf{M}^t$ to be used in the next iterations. At each stage $z$, the contribution of the first path that has been already estimated in the previous iteration, which is stored in $\mathbf{M}^t$, is projected out before determining the new promising AoD intervals. In the next stage $z+1$, two AoD intervals are selected for further refinement, namely, the one selected at stage $z$ of this iteration, and the one selected by the first path at stage $z+1$ of the first iteration which is stored in $\mathbf{M}^t$. The selection of those two AoD intervals enables the algorithm to detect different path with AoDs separated by a resolution up to $\frac{2\pi}{N_Q}$.

5. The algorithm proceeds in the same way until the $L$ paths are solved. After estimating the angles AoAs/AoDs with the desired resolution, the algorithm finally computes the estimated path gains using a linear least squares estimator (LLSE).

## 4.6 Simulation Results

In this section, we present some numerical results to verify the accuracy of the different channel estimators for underground mine communications. To generate these results, the underground channel measurement is considered for different proposed systems. For the accuracy of the channel estimation, the normlalized mean-squared error (NMSE) is used for performance evaluation and is computed as:

$$\text{NMSE} = 10\log_{10}\frac{\sum_{l=0}^{L}\|\mathbf{H}_l - \hat{\mathbf{H}}_l\|_F^2}{\sum_{l=0}^{L}\|\mathbf{H}_l\|_F^2} \tag{4.35}$$

where $\|.\|_F$ stands for the Frobenuis norm of the operand.

### 4.6.1 Performance Evaluation of the Proposed FB-based Underground Channel Estimation

In these simulations, the performance of the proposed FB channel estimation for underground mine channel is investigated in term of NMSE and BER. The conventional OMP and LS estimators are used as a benchmark for the proposed alternative. The system model and the simulation scenario are as follows: We consider $2 \times 1$ STBC-FBMC system at the central frequency of 60 GHz. The maximum transmission distance Tx-Rx is 10 m, the channel level of sparsity is $S_l = 3$ ( for conventional OMP channel estimator), the threshold value is $\varepsilon = 10^{-7}$, the number of iterations per transmit antenna is $\ell_{\max} = 10$, and the number of tracked multi-path components is $L = 100$. Also, the number of pilots is $P = 128$ selected equispaced in the frequency domain. Furthermore, the PHYDYAS prototype filter with $O = 4$ is used. The filter coefficients in the sampled frequency domain are given by $G_0 = 1, G_1 = 0.971960, G_2 = \sqrt{2}/2$ and $G_3 = 0.235147$.

In Figure 4.8, we investigate the variation of the estimation quality regarding the parameters $\alpha$ and $\beta$. For this purpose, the performance over the practical SNR range spanning the values between $-10$ dB and 20 dB has been considered. As illustrated in Figure 4.8, even at low SNR, the proposed FB algorithm is well performing. Moreover, the proposed estimator provides the best accuracy when $\alpha = 6$ and $\beta = 2$. Hence, in this specific channel, decreasing $\alpha$ and $\beta$ allows achieving best results in terms of NMSE. This implies that the number of necessary iterations in the estimation process has been reduced, thus lowering the channel training time.

Therefore, setting the forward and backward parameters to $\alpha = 6$ and $\beta = 2$, respectively. The conventional OMP and the LS estimators are adopted for comparison. As shown in Figure 4.9, It can be observed that the proposed FB approach achieves better effectiveness compared to the conventional OMP estimator and the LS estimator. This is due to the feedback process encompassed in the proposed FB algorithm. The performance enhances with the SNR increase, thereby providing a higher degree of data reliability. Indeed, the both compressive sensing estimators offer higher

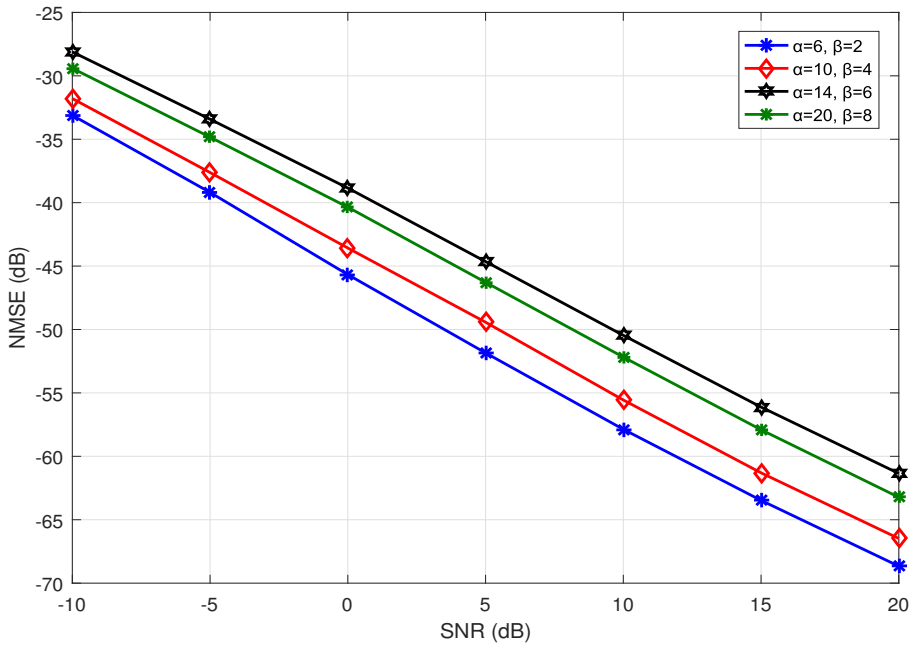


Figure 4.8: NMSE Performances of the proposed algorithm for different values of $\alpha$ and $\beta$.

performance than LS estimator for the whole of SNR regime under test, since the temporal sparsity of mm-Wave underground channels is leveraged for the enhanced channel estimation performance, and reduces the NMSE by 15 dB for values of SNR of $-5$ dB.

With the same system setup, we demonstrate the efficiency of the proposed FB estimator for STBC-FBMC system when increasing the number of transmit antennas. From the Figure 4.10, it can be noted that the proposed FB-based channel estimation approach achieves a good performance even at SNR is low, and the performance gap increases with SNR. Moreover, the proposed estimator provides the best accuracy when increasing the number of antennas, but this increases the error estimation. For instance, at SNR = 0 dB, 5 dB gain in estimation accuracy is provided with FB estimator in the case of $4 \times 1$.

Figure 4.11 provides the BER performance comparison between our proposed FB estimator, the conventional OMP estimator and the LS estimator. The BER performance with the perfect CSI is also included as the benchmark for comparison. From Figure 4.11, it can be observed that the proposed FB-based channel estimation scheme and OMP estimator exhibit identical performance at low SNR regime. However, when the SNR increases above 5 dB, it is seen that the BER achieved by the FB-based underground channel estimator method perform better than the conventional OMP method by about 1.5 dB while possesses less than 1 dB gap from that of the perfect CSI. In

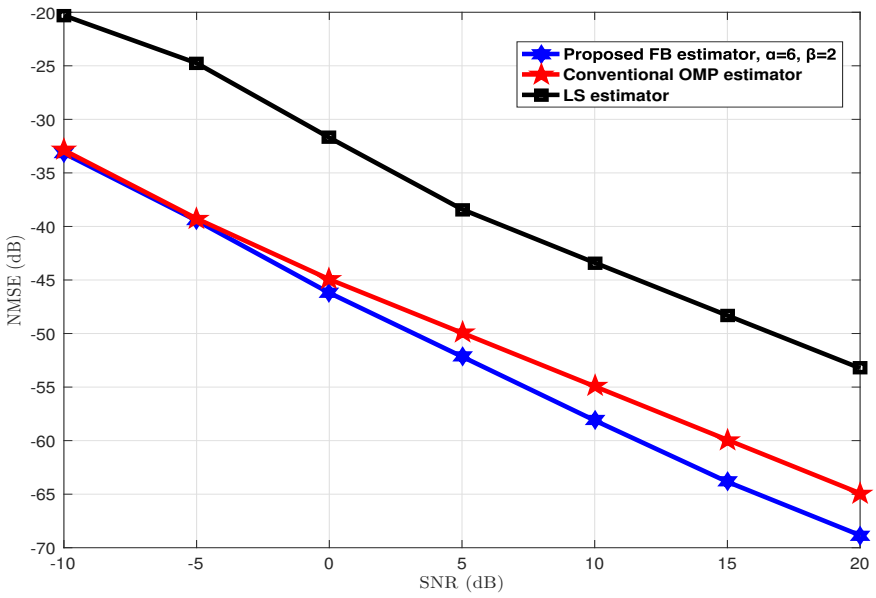


Figure 4.9: NMSE performance comparison between the proposed FB channel estimator and the both conventional OMP and LS estimators.

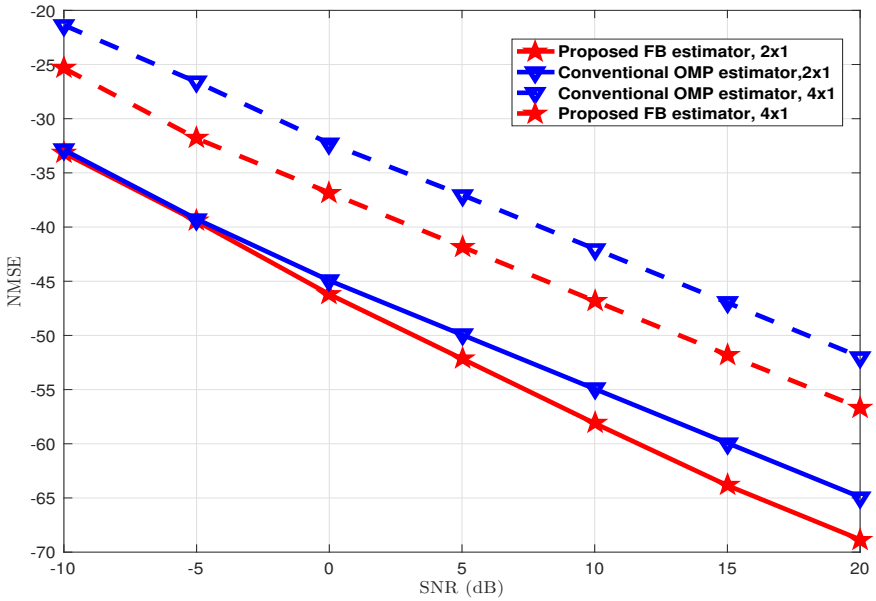


Figure 4.10: NMSE performance comparison between the conventional OMP and proposed FB-based estimation techniques.

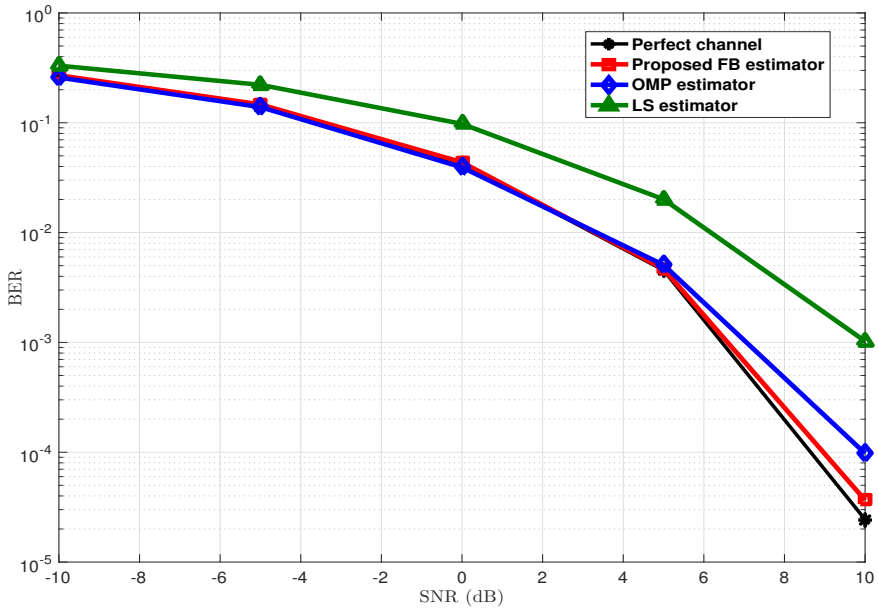


Figure 4.11: BER performance comparison against SNR with perfect CSI in mm-Wave STBC-FBMC system.

addition, the LS estimator performs the worst, although it is very simple. This coming from the fact that the both FB and OMP-based underground channel algorithm is more efficient than the conventional LS estimator for the sparse channel.

### 4.6.2 Performance Evaluation of Hardware Impaired Large MIMO Underground System

The performance of the proposed underground channel estimator for hardware impaired large MIMO system is examined through computer simulation with the following parameters. The system is operated at 60 GHz carrier frequency, has a bandwidth of 5 GHz, the transmitter and the receiver are equipped with $N_t = N_r = 20$ and $N_{\text{RF}} = 2$. The results are based on the measured mm-Wave MIMO underground channel which is assumed to consist of $L = 3$ non-zeros paths. For channel estimation, the AoA/AoD resolution parameter $N_Q = 64$, and with $\mathcal{K} = 2$ beamforming vectors at each stage.

Figure 4.12 provides the comparison of the achievable rate versus the SNR for MIMO underground system based-hybrid beamforming in both cases of perfect and

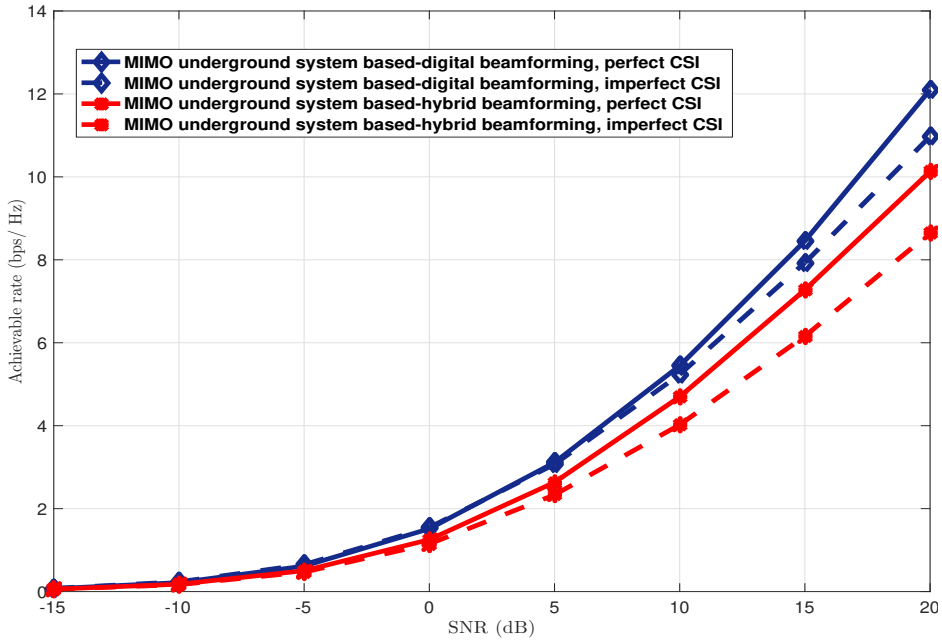


Figure 4.12: Achievable rate performace of the estimated MIMO underground channel under ideal hardware.

imperfect CSI by considering ideal hardware, along with the optimal full beamforming solution is considered. The results indicate that comparable gains can be achieved using the proposed MIMO underground system despite their imperfect channel. Also, the results show that the achievable rate performance degradation of MIMO underground system based-hybrid beamforming is less than 1 bps/Hz compared with the system based digital beamforming solution that requires much more RF hardware.

In Figure 4.13, the joint impact of imperfect channel estimation for for different levels of impairments $k_t = k_r \in \{0, 0.15, 0.3\}$ on the achievable rate performance is studied, and compared with the ideal system with perfect CSI and ideal hardware at the transceiver for mm-Wave underground channel. We can observe from this figure, that at low SNRs, transceiver hardware impairments have negligible impact on the achievable rates even with imperfect CSI, while at high SNRs, transceiver hardware impairments decrease the achievable rates for all cases. More importantly, hardware impairments create a SNR wall, which cannot be crossed by increasing the transmit power. We can see that the achievable rate performance under perfect CSI and ideal hardware increases as SNR increases.

Figure 4.14 shows the NMSE performance of the hardware impaired MIMO underground channel-based hybrid beamforming scheme against SNR for different levels

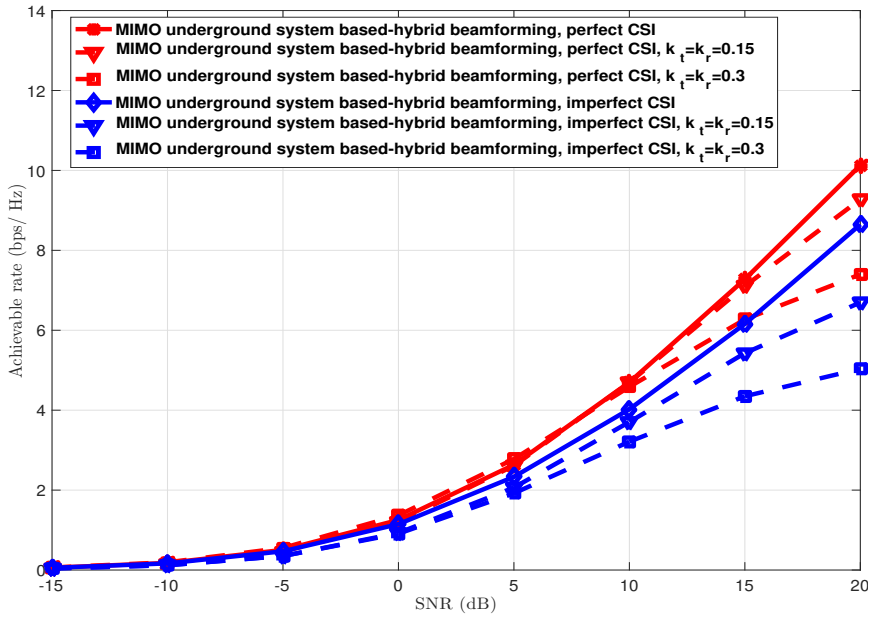


Figure 4.13: Impact of both the hardware impairments and imperfect channel estimation on the achievable rate performance.

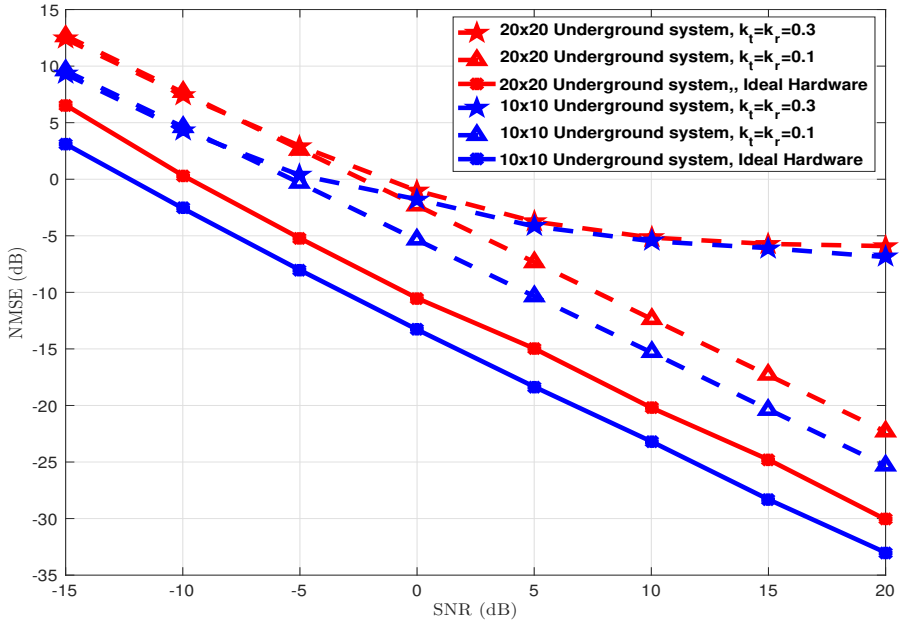


Figure 4.14: NMSE performance of the hardware impaired MIMO underground channel.

of impairments. For comparaison, the NMSE without transceiver hardware impairments ($i.e., k_t = k_r = 0$) is also shown. We consider two antenna configurations, i.e., $N_t = N_r = 10$ and $N_t = N_r = 20$. From this figure, it can be observed that without the existence of hardware impairments, increasing the SNR decreases the NMSE monotonically towards zero. However, in the presence of hardware impairments, we observe a fundamentally different behavior. Specifically, when the number of transceiver antennas is large.

## 4.7 Conclusion

In this Chapter, we have focused on compressive sensing channel estimation problem in mm-Wave underground system using the real measurements of channel at the frequency band of 60 GHz. Firstly, we have presented the conventional OMP based-channel estimation applied to STBC-FBMC system with two prototypes filters, then we have designed an iterative FB processing-based mm-Wave underground channel estimation approach to estimate the channel using pilot sub-carriers simultaneously. In the proposed approach, two consecutive processing steps are carried out to accurately identify the sparse components of the channel. In the forward step, the support estimate is enlarged. Then, the obtained path index of the channel is used as the initialization set in the backward process to allow the feedback cancellation of the possibly incorrect indices. The performance of the proposed FB approach is compared with the conventional OMP and LS estimators in terms of NMSE and BER. It was shown that, in addition to the improvement of the channel estimation accuracy from a limited number of pilots, hence enhancing the spectral efficiency, another important property of the proposed approach lies in its blindness to the sparsity level. It was seen that quasi-perfect channel reconstruction was obtained by tuning the forward and backward coefficients, $\alpha$ and $\beta$. It has been verified that the FB approach is an efficient method for sparse underground channel estimation in STBC-FBMC/QAM transmission networks. The second contribution of this chapter is investigate the impact of transceiver hardware inaccuracies on the channel estimation of mm-Wave MIMO underground system when exploiting the channel reciprocity. For this, we have investigated the problem of channel estimation under hardware impairments for the underground MIMO system based hybrid beamforming. Numerical results showed that, the transceiver hardware impairments have a deleterious impact on the achievable rate and channel estimation.

# CHAPTER 5

# BEAMFORMING UAV RELAY-AIDED MM-WAVE SYSTEM

## Contents

## 5.1 Introduction

Mm-Wave communications have been envisioned as a dominant candidate for enhancing the data rate, due to the huge bandwidth availability in their frequency bands, and the great potentialities they offer for massive arrays adoption [7,12]. However, there are a number of problems with mm-Wave communication that must be overcome for its full potential to be realized. The first problem is posed by the very high propagation loss, which drastically limits the communication distance. Another significant challenge is their sensitivity to blockage from surrounding objects, e.g. high-rise buildings, which classifies the links between the BSs and users into LOS and NLOS [36]. On the other hand, high channel dynamics, particularly in some outdoor environments, make the blockage a quite challenging problem [92]. To address these difficulties, in this chapter, we are interested in an urban type environment where the UAV is used as a flying relay to assist the mm-Wave communication from various ground BSs to multiple users. The main contributions of this chapter are:

- First, to explore the potential gain of UAV-based amplify and forward (AF) multi-antenna relay, we generate the geometric 3D mm-Wave channel, then we demonstrate that UAV-based AF multi-antenna relay can mitigate the blockage and path loss drawbacks usually occurring in the multi-user mm-Wave MIMO-OFDM communications.

- Second, to fully exploit the advantages of distributed BSs and improve communication quality under strict hardware constraints in UAV enable communications, we propose a hybrid beamforming-thru scheme between the multiple BSs, the relay and the ground users, merging the spatial processing and the AF operation.

- The third contribution is to design a two stages distributed optimization approach to define a users-BSs association pattern, while maximizing sum data rates in our proposed scenario.

- Finally, the achievable data rate of relay networks with multiple source-destination pairs is investigated when CSI is available at the both sides. Through simulations, we analyse the performances of the proposed system: (i) the effect of the UAV altitude on the achievable rates and show the efficiency of the proposed system, (ii) users-BSs association, and (iii) the achievable rate of the proposed system based-UAV relay. Simultaneously, it also studies the of the multi-user mm-Wave MIMO-OFDM system under correlated channels.

## 5.2 Multi-user Mm-Wave MIMO-OFDM System Model

We consider a single-cell consisting of a set of BSs denoted $N_{\text{BS}}$, simultaneously connected to $U$ users with the help of one UAV relay and surrounded by a number of city buildings as shown in Figure 5.1. In this system, there is no direct link between the source nodes (BSs) and their destinations (users) due to blockage and large shadowing, hence the information can only be delivered through the UAV relay. The proposed UAV relay-enabled architecture focuses on a half-duplexing AF relaying between BSs and users, hence it cannot transmit and receive at the same time. In order to enhance the communication quality, both of the BSs and the UAV relay are equipped with massive MIMO deployments at the 28 GHz frequency band. Meanwhile, to reduce the cost at users end, only a single omnidirectional antenna is assumed. The hybrid beamforming structure is applied between the multiple BSs, the UAV relay, and the ground users as illustrated in Figure 5.2. Specifically, the number of antennas at each BS and the UAV relay are denoted as $N_t$ and $N_{\text{re}}$, respectively, and both BSs and UAV hold the same number of RF chains, denoted as $N_{\text{RF}}$, where $N_t \geq N_{\text{re}} \gg N_{\text{RF}}$, and $N_{\text{RF}} = U$ to support the $U$ users. Similarly, the total number of streams are $N_s = U$. Furthermore, each user is equipped with only one RF chain and no baseband beamformer, thereby, reducing the processing complexity at the destination.

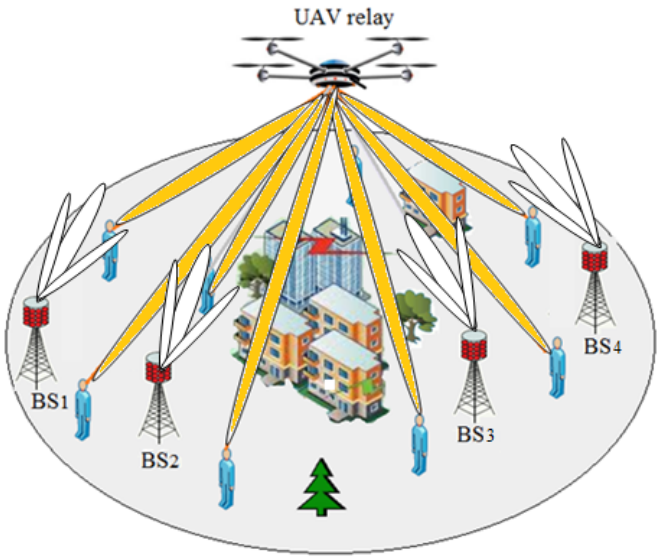


Figure 5.1: System model for UAV relay-enabled architecture for multi-user mm-Wave MIMO-OFDM system.

For our scenario, it is assumed that the BSs and the users are randomly distributed in a specified region using stochastic geometry approach and according to a Matern type-I hard-core process [93], with an intensity of $\lambda_a$ per $m^2$, and a minimum separation of $d_{\text{BS}}^{\min}$ and $d_U^{\min}$ with their neighbors, respectively. Without loss of generality, we consider that the UAV can dynamically fly in the horizontal space with a fixed altitude in the three-dimensional (3D) plane, and the corresponding coordinates are $(x_r,y_r,z_r)$. Equivalently, we refer by $(x_j,y_j,z_j)$ to the 3D position of the $j^{th}$ BS, and with $(x_u,\ y_u)$ to the 2D location of the $u^{th}$ user. Since UAV usually navigates much faster than the ground nodes, we assume the channel variation mainly comes from UAV relay movements.

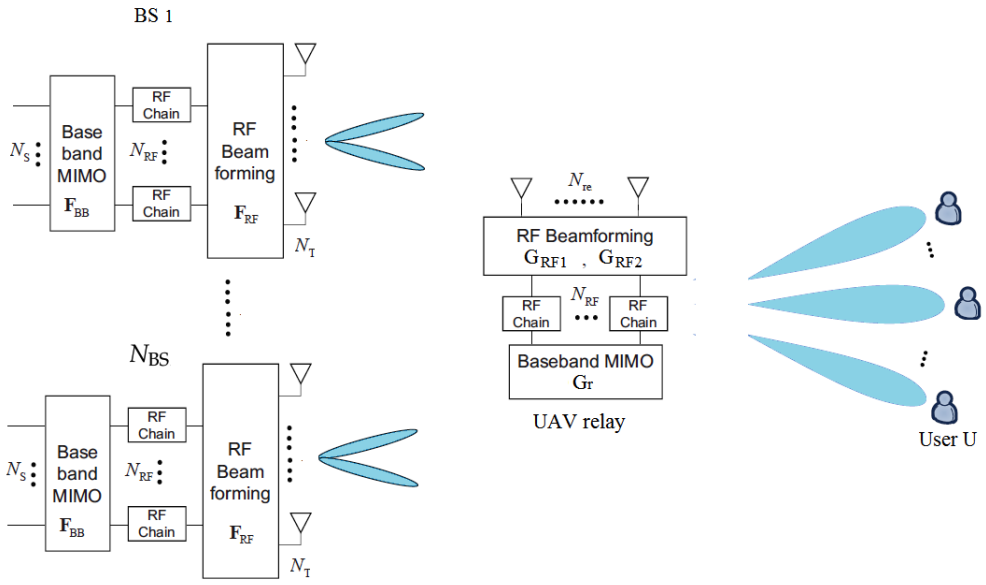


Figure 5.2: UAV relay based-hybrid beamforming architecture.

To deal with the frequency selective fading, the multi-user mm-Wave massive MIMO system normally uses OFDM scheme [33]. Suppose the number of OFDM sub-carriers is $K$. It is important to emphasize here that the RF beamforming matrix is the same for all sub-carriers, because the RF beamformer cannot be implemented separately for each sub-carrier. This means that the RF beamformer is assumed to be frequency flat while the baseband beamformers can be different for each sub-carrier.

For convenience, let us represent the symbols transmitted from each source node as $\mathbf{s}=[s_1, s_2, ..., s_U]^T$. The transmission process from the sources to the destinations takes place during two phases, where each BS node is allowed to transmit to each user but sends a different data symbol than the other BSs:

• During the first transmission phase, each $j^{th}$ BS node applies a $N_t \times U$ beamforming matrix, denoted $\mathbf{F}^j(k)$, to transmit a symbol for each user. The transmitted signal from the $j^{th}$ BS using the $k^{th}$ sub-carrier can be expressed as:

$$\mathbf{x}^j(k) = \mathbf{F}^j(k)\mathbf{s}^j(k), \tag{5.1}$$

where $\mathbf{F}^j(k) = \mathbf{F}^j_{\mathrm{RF}}\mathbf{F}^j_{\mathrm{BB}}(k)$ is the hybrid beamforming matrix for the $j^{th}$ BS, with $\mathbf{F}^j_{\mathrm{RF}}$ being the $N_t \times U$ analog RF matrix, and $\mathbf{F}^j_{\mathrm{BB}}(k) = [\mathbf{f}^{(1,j)}_{\mathrm{BB}}(k), \mathbf{f}^{(2,j)}_{\mathrm{BB}}(k), ..., \mathbf{f}^{(U,j)}_{\mathrm{BB}}(k)]$ is the $U \times U$ baseband beamforming matrix. Let $\mathbf{s}^j(k) = [s^{(1,j)}(k), ..., s^{(u,j)}(k), ..., s^{(U,j)}(k)]^T$ represent the transmitted symbols from the $j^{th}$ BS node, such that $\mathrm{E}[\mathbf{s}^j(k)(\mathbf{s}^j(k))^H] = \frac{P}{U}\mathrm{I}_{N_s}$, with $P$ representing the total signal power at the $j^{th}$ BS. The total power constraint at the source is given as:

$$P_s = \mathrm{E}[\mathbf{x}^j(k)(\mathbf{x}^j(k))^H] = \mathrm{tr}\big(\mathbf{F}^j_{\mathrm{RF}}\mathbf{F}^j_{\mathrm{BB}}(k)(\mathbf{F}^j_{\mathrm{BB}}(k))^H(\mathbf{F}^j_{\mathrm{RF}})^H\big), \tag{5.2}$$

The received signal at the UAV relay in the $k^{th}$ sub-carrier could thus be represented as:

$$\mathbf{y}(k) = \sum_{j=1}^{N_{\mathrm{BS}}} \mathbf{H}^j_1(k) \sum_{u=1}^{U} \mathbf{F}^j_{\mathrm{RF}}\mathbf{f}^{(u,j)}_{\mathrm{BB}}(k)\mathrm{s}^{(u,j)}(k) + \mathbf{w}(k), \tag{5.3}$$

where $\mathrm{s}^{(u,j)}(k)$ is the transmit symbol which BS $j$ intends to transmit to user $u$, $\mathbf{H}^j_1 \in \mathbb{C}^{N_{re} \times N_t}$ is the frequency domain channel matrix between the $j^{th}$ BS and UAV relay, and $\mathbf{w}(k) \in \mathbb{C}^{N_{\mathrm{re}} \times 1}$ is the additive white Gaussian noise vector whose entries are with zero mean and $\sigma_r^2$ variance.

• In the second phase, the transmitted signal from the BSs is firstly received through $U \times N_{\mathrm{re}}$ analog receive matrix $\mathbf{G}_{\mathrm{RF2}}$ at the UAV relay, then amplified by the $U \times U$ baseband matrix $\mathbf{G}_{\mathrm{r}}(k)$, and subsequently forwarded to all users through the $N_{\mathrm{re}} \times U$ analog transmit matrix $\mathbf{G}_{\mathrm{RF1}}$ [42]. The signal transmitted by the UAV relay is expressed as:

$$\begin{aligned}
\mathbf{x}_r(k) &= \mathbf{G}_{\mathrm{RF1}}\mathbf{G}_{\mathrm{r}}(k)\mathbf{G}_{\mathrm{RF2}}\mathbf{y}(k) \\
&= \mathbf{G}_{\mathrm{RF1}}\mathbf{G}_{\mathrm{r}}(k)\mathbf{G}_{\mathrm{RF2}} \sum_{j=1}^{N_{\mathrm{BS}}} \mathbf{H}^j_1(k) \sum_{u=1}^{U} \mathbf{F}^j_{\mathrm{RF}}\mathbf{f}^{(u,j)}_{\mathrm{BB}}(k)\mathrm{s}^{(u,j)}(k) + \mathbf{G}_{\mathrm{RF1}}\mathbf{G}_{\mathrm{r}}(k)\mathbf{G}_{\mathrm{RF2}}\mathbf{w}(k) \\
&= \mathbf{G}(k) \sum_{j=1}^{N_{\mathrm{BS}}} \mathbf{H}^j_1(k) \sum_{u=1}^{U} \mathbf{F}^j_{\mathrm{RF}}\mathbf{f}^{(u,j)}_{\mathrm{BB}}(k)\mathrm{s}^{(u,j)}(k) + \mathbf{W}(k),
\end{aligned} \tag{5.4}$$

where $\mathbf{G}(k) = \mathbf{G}_{\mathrm{RF1}}\mathbf{G}_{\mathrm{r}}(k)\mathbf{G}_{\mathrm{RF2}}$ represents the overall relay processing matrix at the UAV relay, and $\mathbf{W}(k) = \mathbf{G}_{\mathrm{RF1}}\mathbf{G}_{\mathrm{r}}(k)\mathbf{G}_{\mathrm{RF2}}\mathbf{w}(k)$ encompasses the equivalent noise [32]. Assuming the transmission power at the relay is $P_r$, the power constraint at the UAV relay is:

$$\begin{aligned} P_r &= \mathrm{tr}\Big\{E[\mathbf{x}_r(k)\mathbf{x}_r^H(k)]\Big\} \\ &= \mathrm{tr}\Big\{\Big(\mathbf{G}(k)\sum_{j=1}^{N_{\mathrm{BS}}}\mathbf{H}_1^j(k)\mathbf{F}^j(k)\Big)\Big(\mathbf{G}(k)\sum_{j=1}^{N_{\mathrm{BS}}}\mathbf{H}_1^j(k)\mathbf{F}^j(k)\Big)^H + \sigma_r^2\mathbf{W}(k)\mathbf{W}^H(k)\Big\}, \end{aligned} \tag{5.5}$$

The recovered signal at the $u^{th}$ user could be written as:

$$\begin{aligned} \mathrm{Y}_u(k) &= \mathbf{H}_{2,u}(k)\mathbf{x}_r^u(k) + \sum_{u'\neq u}^{U}\mathbf{H}_{2,u}(k)\mathbf{x}_r^{u'}(k) + \mathrm{W}_u(k), \\ &= \mathbf{H}_{2,u}(k)\mathbf{G}(k)\sum_{j=1}^{N_{\mathrm{BS}}}\mathbf{H}_1^j(k)\mathbf{F}_{\mathrm{RF}}^j\mathbf{f}_{\mathrm{BB}}^{(u,j)}(k)\mathrm{s}^{(u,j)}(k) + \\ &\sum_{u'\neq u}^{U}\mathbf{H}_{2,u}(k)\mathbf{G}(k)\sum_{j=1}^{N_{\mathrm{BS}}}\mathbf{H}_1^j(k)\mathbf{F}_{\mathrm{RF}}^j\mathbf{f}_{\mathrm{BB}}^{(u',j)}(k)\mathrm{s}^{(u',j)}(k) + \mathrm{W}_u(k), \end{aligned} \tag{5.6}$$

The first part in (5.6) is the superposition of desired signals that user $u$ receives from the BSs. The second part is multi-user interference that degrades the quality of the detected signals. The third part is the additive white noise at the $u^{th}$ user, while $\mathbf{H}_2 \in \mathbb{C}^{U\times N_{re}}$ is the frequency domain channel matrix between the UAV relay and the users. For the UAV-assisted mm-Wave wideband communications involved herein, both channels $\mathbf{H}_1^j$ and $\mathbf{H}_{2,u}$ are represented using a 3D geometric model.

## 5.3 3D Geometry based-UAV Mm-Wave Channel Model

When dealing with terrestrial communications, Saleh-Valenzuela model is sufficient to depict the propagation within the corresponding channels [94]. However, radio wave propagation in air-to-ground (A2G) communications has different mechanisms [95]. Herein, we describe the UAV-assisted mm-Wave wideband communications channel model between the $j^{th}$BS node and the multi-antennas UAV relay, and also between the UAV relay and the grounds users. Both channels $\mathbf{H}_1^j$ and $\mathbf{H}_{2,u}$ used in our system model are Fourier transforms of temporal channels. Hence, the corresponding channels impulse response $\mathbf{h}_1^j$ and $\mathbf{h}_{2,u}$ could be expressed as [96]:

$$\mathbf{h}_1^j(t) = \sum_{l=1}^{L} \frac{\alpha_l^j}{[D^j]^\nu} e^{(-j2\pi f_d T_s \cos\varphi_l^j + \gamma_l^j)} \mathbf{a}_t^j(\phi_l^{j,t}, \theta_l^{j,t}) \mathbf{a}_r^j(\phi_l^{j,r}, \theta_l^{j,r}), \tag{5.7}$$

$$\mathbf{h}_{2,u}(t) = \sum_{l=1}^{L} \frac{\alpha_l^u}{[D^u]^\nu} e^{(-j2\pi f_d T_s \cos\varphi_l^u + \gamma_l^u)} \mathbf{a}_t^u(\phi_l^{u,t}, \theta_l^{u,t}), \tag{5.8}$$

where $\alpha_l^j$ and $\alpha_l^u$ are the small-scale fading coefficients associated with the $l^{th}$ propagation path of the $j^{th}$ BS and the one of the $u^{th}$ user, respectively, $D^j$ is the distance between the $j^{th}$ BS and UAV relay, $D^u$ is the distance between the UAV relay and the $u^{th}$ user, $L$ is the number of multi-paths which is assumed to be the same for the BS-relay and the relay-user links, $\nu$ is the large-scale fading coefficient, $f_d$ is the maximum Doppler frequency, $T_s$ is the system sampling period, $\varphi_l^j$ and $\varphi_l^u$ are the angle between the transmitted signal and the motion direction of the $l^{th}$ path emanating from the $j^{th}$ BS, and the one originating from UAV relay, repectively, $\gamma_l$ refers to the corresponding initial phases. The vectors $\mathbf{a}_t^j(\phi_l^{j,t}, \theta_l^{j,t})$, $\mathbf{a}_r^j(\phi_l^{j,r}, \theta_l^{j,r})$, and $\mathbf{a}_t^u(\phi_l^{u,t}, \theta_l^{u,t})$ are the array response at the BS source, the receiving UAV relay and at the destination, respectively. In this chapter, we consider the uniform square planar array (USPA) with $\sqrt{N_x} \times \sqrt{N_x} (x \in$ BSs or relay$)$ antenna elements, which can be defined as:

$$\mathbf{a}_t^j(\phi_l^{j,t}, \theta_l^{j,t}) = \frac{1}{\sqrt{N_x}} \Big[1, ..., e^{j\frac{2\pi\delta_j}{\lambda_c}\left((\sqrt{N_x}-1)\sin(\theta_l^{j,t})\sin(\phi_l^{j,t}) + (\sqrt{N_x}-1)\cos(\phi_l^{j,t})\right)}\Big]^T, \tag{5.9}$$

$$\mathbf{a}_r^j(\phi_l^{j,r}, \theta_l^{j,r}) = \frac{1}{\sqrt{N_x}} \Big[1, ..., e^{j\frac{2\pi\delta_r}{\lambda_c}\left((\sqrt{N_x}-1)\cos(\theta_l^{j,r})\sin(\phi_l^{j,r}) + (\sqrt{N_x}-1)\cos(\phi_l^{j,r})\right)}\Big]^T, \tag{5.10}$$

$$\mathbf{a}_t^u(\phi_l^{u,t}, \theta_l^{u,t}) = \frac{1}{\sqrt{N_x}} \Big[1, ..., e^{j\frac{2\pi\delta_r}{\lambda_c}\left((\sqrt{N_x}-1))\cos(\theta_l^{u,t})\sin(\phi_l^{u,t}) + (\sqrt{N_x}-1)\cos(\phi_l^{u,t})\right)}\Big]^T, \tag{5.11}$$

where, for the $l^{th}$ path, $\phi_l^{j,t}$, $\theta_l^{j,t}$, $\phi_l^{j,r}$, $\theta_l^{j,r}$ represent the azimuth AoD, the elevation AoD, the azimut AoA and the elevation AoA corresponding to the $j^{th}$ BS, respectively, while $\phi_l^{u,t}$, $\theta_l^{u,t}$ represent the azimuth AoD, the elevation AoD of the UAV relay when communicating with the $u^{th}$ user, respectively. Moreover, $\delta_j$ (or $\delta_r$) represent the spacing between two adjacent antenna elements on each BS node (or on the UAV relay), and $\lambda_c$ is the signal carrier wavelength. Defining the distance between the UAV relay and the $j^{th}$ BS as:

$$D^j = \sqrt{(x_j - x_r)^2 + (y_j - y_r)^2 + (z_j - z_r)^2}, \tag{5.12}$$

The corresponding angles pertaining to the LOS in ( 5.7) are retrieved as:

$$\varphi_0^j = \arccos \sqrt{(x_j - x_r)^2 + (z_j - z_r)^2}/D^j, \tag{5.13}$$

$$\theta_0^j = \arcsin \sqrt{(y_j - y_r)^2}/D^j, \tag{5.14}$$

$$\phi_0^j = \arccos(z_r/D^j), \tag{5.15}$$

Thus, the ones corresponding to other multipath components are derived as:

$$\text{ang}_l^j = (\text{ang}_{\text{LOS}}^j - \pi/2) + \pi * \mathcal{U}, \tag{5.16}$$

where $\mathcal{U}$ is uniformly distributed over [0,1]. The angles in (5.8) from the UAV relay to the $u^{th}$ user are generated in the same way. In the frequency domain, any channel response at the $k^{th}$ sub-carrier could be written as:

$$\mathbf{H}(k) = \sum_{t=0}^{N-1} \mathbf{h}(t) e^{-j\frac{2\pi kt}{K}}, \quad k = 1, ..., K \tag{5.17}$$

## 5.4 Performance Analysis

In this section, we derive analytical expressions for the achievable data rate of the proposed multi-user mm-Wave MIMO-OFDM system, which relies on UAV relay architecture, assuming perfect effective channel knowledge. The quality of the wireless link is measured in terms of the signal to interference-and-noise ratio (SINR). Treating the interference as noise, the received SINR of $u^{th}$ user by direct transmission can be calculated as follows:

$$\text{SINR}_{(s,d)} = \frac{\left| \sum_{j=1}^{N_{\text{BS}}} \mathbf{H}_u^j(k) \mathbf{F}_{\text{RF}}^j \mathbf{f}_{\text{BB}}^{(u,j)}(k) \right|^2}{\sum_{u' \neq u}^{U} \left| \sum_{j=1}^{N_{\text{BS}}} \mathbf{H}_u^j(k) \mathbf{F}_{\text{RF}}^j \mathbf{f}_{\text{BB}}^{(u',j)}(k) \right|^2 + \sigma_u^2(k)} \tag{5.18}$$

where $\mathbf{H}_u^j(k)$ is the frequency domain channel between the $j^{th}$ BS and the $u^{th}$ user. According to the signal model introduced in (5.6), the SINR received by user $u^{th}$ from BS $j^{th}$ trough UAV relay, denoted by $\vartheta_{uj}$, can be derived as:

$$\vartheta_{uj} = \frac{\left| \sum_{j=1}^{N_{\mathrm{BS}}} \mathbf{H}_{2,u}(k)\mathbf{G}(k)\mathbf{H}_1^j(k)\mathbf{F}_{\mathrm{RF}}^j\mathbf{f}_{\mathrm{BB}}^{(u,j)}(k) \right|^2}{\sum_{u'\neq u}^{U} \left| \sum_{j=1}^{N_{\mathrm{BS}}} \mathbf{H}_{2,u}(k)\mathbf{G}(k)\mathbf{H}_1^j(k)\mathbf{F}_{\mathrm{RF}}^j\mathbf{f}_{\mathrm{BB}}^{(u',j)}(k) \right|^2 + \sigma_u^2(k)} \tag{5.19}$$

where $\sigma_u(k)$ is the noise power at the $u^{th}$ user, $\left| \sum_{j=1}^{N_{\mathrm{BS}}} \mathbf{H}_{2,u}(k)\mathbf{G}(k)\mathbf{H}_1^j(k)\mathbf{F}_{\mathrm{RF}}^j\mathbf{f}_{\mathrm{BB}}^{(u,j)}(k) \right|^2$ is the desired signal power, $\sum_{u'\neq u}^{U} \left| \sum_{j=1}^{N_{\mathrm{BS}}} \mathbf{H}_{2,u}(k)\mathbf{G}(k)\mathbf{H}_1^j(k)\mathbf{F}_{\mathrm{RF}}^j\mathbf{f}_{\mathrm{BB}}^{(u',j)}(k) \right|^2$ is the inter-user interference. Accordingly, the achievable rate provisioning from the $j^{th}$ BS to the $u^{th}$ user when communicating through the UAV relay is calculated as follows:

$$R_{uj} = b_{uj}\left[\log_2(1+\vartheta_{uj})\right] \tag{5.20}$$

From (5.20) we can write the allocated bandwidth $b_{uj}$ as follows:

$$b_{uj} = \frac{R_{uj}}{\vartheta_{uj}} \tag{5.21}$$

The total data rate of all associated users with each BS in the network can be written as:

$$R_{\mathrm{sum}} = \sum_{u=1}^{U} R_{uj} \tag{5.22}$$

## 5.5 Multi-user Hybrid Beamforming Algorithm

For UAV relay-assisted multi-user mm-Wave MIMO-OFDM architecture with a large number of antennas, it is costly to connect each antenna to a separate RF chain and more complicated than using direct transmission [97]. A hybrid beamforming relay, where each RF chain is connected to multiple antennas, can significantly reduce the system cost [98]. Throughout this section, a two-phase wideband hybrid beamformer algorithm is designed to maximize the data rate of the users at the destination. In the first phase, we aim to design the RF analog beamforming and combining matrices $\mathbf{F}_{\mathrm{RF}}^j$ and $\mathbf{G}_{\mathrm{RF2}}$ in order to maximize the desired signal power of each BS and the digital beamforming $\mathbf{F}_{\mathrm{BB}}^j(k)$ in order to manage the interfrence between BSs. In the second phase, the digital beamforming of the UAV relay $\mathbf{G}_r(k)$ is constructed to manage the multi-user interference. Hence, the beamforming at the relay corresponding to the emitting $j^{th}$ BS could be decomposed as:

$$\mathbf{G}(k) = \mathbf{G}_{\mathrm{RF1}}\mathbf{G}_r(k)\mathbf{G}_{\mathrm{RF2}} \tag{5.23}$$

- In phase I, the analog beamforming and combining matrices at the BS and the UAV relay are designed to maximize the desired signal power, neglecting interference between different data streams. Let $\mathcal{F}_{RF}^{j}$ , $\mathcal{G}_{RF1}$ and $\mathcal{G}_{RF2}$ denote the set of analog beamforming matrices $\mathbf{F}_{RF}^{j}(:,u)$ , $\mathbf{G}_{RF1}(:,u)$ and $\mathbf{G}_{RF2}(u,:)$, $u = 1,...,U$, respectively, which are selected from the array response vectors as follow:

$$\mathcal{G}_{RF1} = \mathbf{A}_{t-rel} = [\mathbf{a}_t^1(\phi_l^t,\theta_l^t),...,\mathbf{a}_t^U(\phi_l^t,\theta_l^t)]^T \tag{5.24}$$

$$\mathcal{G}_{RF2} = \mathbf{A}_{r-rel} = [\mathbf{a}_r^{j,1}(\phi_l^{j,r},\theta_l^{j,r}),...,\mathbf{a}_r^{j,U}(\phi_l^{j,r},\theta_l^{j,r})]^T \tag{5.25}$$

$$\mathcal{F}_{RF}^{j} = \mathbf{A}_t^j = [\mathbf{a}_t^{j,1}(\phi_l^{j,t},\theta_1^{j,t}),...,\mathbf{a}_t^{j,U}(\phi_l^{j,t},\theta_l^{j,t})]^T \tag{5.26}$$

The $j^{th}$ BS and the UAV relay select $\mathbf{g}_{\mathrm{u}}^{\star}$ and $\mathbf{f}_u^{j\star}$ that solve:

$$\left\{\mathbf{g}_u^{\star},\mathbf{f}_u^{j\star}\right\} = \underset{\mathbf{g}_u\in\mathcal{G}_{RF2},\mathbf{f}_u^j\in\mathcal{F}_{RF}^j}{\arg\max} \left\|\mathbf{g}_u\mathbf{H}_1^j(k)\mathbf{f}_u^j\right\|, \quad u = 1,2,...,U, \tag{5.27}$$

where $\mathbf{g}_u$ and $\mathbf{f}_u^j$ denote, respectively, the $u^{th}$ row of $\mathbf{G}_{\mathrm{RF2}}$, and the $u^{th}$ column of $\mathbf{F}_{\mathrm{RF}}^{j}$ in a descending order, according to their respective Frobenius norms. Thus the $j^{th}$ BS sets $\mathbf{F}_{\mathrm{RF}}^{j} = [\mathbf{f}_1^{j\star},...,\mathbf{f}_U^{j\star}]$ and $\mathbf{G}_{\mathrm{RF2}} = [\mathbf{g}_1^{\star},...,\mathbf{g}_U^{\star}]$. We can then obtain the effective channel as:

$$\mathbf{H}_e^j(k) = \mathbf{G}_{\mathrm{RF2}}\mathbf{H}_1^j(k)\mathbf{F}_{\mathrm{RF}}^j \tag{5.28}$$

Then, the design of $\mathbf{F}_{\mathrm{BB}}^{j}(k)$ at the $j^{th}$ BS based on ZF has a form of:

$$\mathbf{F}_{\mathrm{BB}}^{j}(k) = \mathbf{H}_e^j(k)^H(\mathbf{H}_e^j(k)\mathbf{H}_e^j(k)^H)^{-1} \tag{5.29}$$

- In phase II, the design problem of the RF beamforming $\mathbf{G}_{\mathrm{RF1}}$ to maximize the desired signal power for user $u$, and neglecting the other users' interference is given as:

$$\mathbf{r}_{\mathrm{u}}^{\star} = \underset{\mathbf{r}_{\mathrm{u}} \in \mathcal{G}_{RF1}}{\arg\max} \left\| \mathbf{H}_{2,u}(k)\mathbf{r}_{\mathrm{u}} \right\|, \quad \mathrm{u} = 1, ..., U, \tag{5.30}$$

The relay sets $\mathbf{G}_{\mathrm{RF1}} = [\mathbf{r}_1^{\star}, \mathbf{r}_2^{\star} ..., \mathbf{r}_U^{\star}]$. The effective channel of the $u^{th}$ user is given as:

$$\mathbf{h}_{ef}^{u}(k) = \mathbf{H}_{2,u}(k)\mathbf{G}_{\mathrm{RF1}} \tag{5.31}$$

Based on ZF scheme, the $\mathbf{G}_{\mathrm{r}}(k)$ is given as:

$$\mathbf{G}_{\mathrm{r}}(k) = \mathbf{H}_{ef}(k)^{H}(\mathbf{H}_{ef}(k)\mathbf{H}_{ef}(k)^{H})^{-1}, \quad \mathbf{H}_{ef}(k) = [\mathbf{h}_{ef}^{1}(k), ..., \mathbf{h}_{ef}^{U}(k)] \tag{5.32}$$

The hybrid beamforming for multi-user mm-Wave MIMO-OFDM system is summarized in **Algorithm 6**:

## 5.6 Joint User Association and Rate Maximization

In practice, the deployment of mm-Wave BSs mainly depends on the geographical distribution of target users and the environmental blockages, as well as candidate BS sites. In this work, we consider a communication between many BSs and users via one UAV relay aquipped with multiple antennas, where the UAV relay is moving in the horizontal plane with a fixed altitude. This configuration aims at ensuring a more likely presence of a direct LoS connection between the BSs and users. We assume that Matern type-I hard-core process is used to generate the distribution of all users and BSs which respects a given distance between the neighbors over a square region of area $A_s$ [93]. We formulate our user association problem as a mixed Binary non-linear programming (MBNLP) and solve it through a novel optimization scheme which we refer to as two-stage distributed algorithm. The proposed algorithm involves joint users association and data rate maximization under the constrainst of bandwidth limitation for all BSs and the QoS for all users. The use of hybrid beamforming can significantly impact the rate of the overall system, and consequently the users association with each BS.

**Algorithm 6** Hybrid beamforming relaying design

**Inputs:** $\mathbf{A}_{t-rel}$, $\mathbf{A}_{r-rel}$, $\mathbf{A}_t^j$

**Phase 1**

1: The sources and the UAV relay select and that solve:

$$\left\{\mathbf{g}_{\mathrm{u}}^{\star}, \mathbf{f}_{\mathrm{u}}^{j\star}\right\} = \underset{\mathbf{g}_u \in \mathcal{G}_{RF2}, \mathbf{f}_u^j \in \mathcal{F}_{RF}^j}{\arg\max} \left\| \mathbf{g}_{\mathrm{u}} \mathbf{H}_1^j(k) \mathbf{f}_{\mathrm{u}}^j \right\|, \quad \mathrm{u} = 1, ..., U,$$

2: BS sets $\mathbf{F}_{\mathrm{RF}}^j = [\mathbf{f}_1^{j\star}, \mathbf{f}_2^{j\star}, ..., \mathbf{f}_{\mathrm{U}}^{j\star}]$,

3: UAV relay sets $\mathbf{G}_{\mathrm{RF2}} = [\mathbf{g}_1^{\star}, \mathbf{g}_2^{\star}, ..., \mathbf{g}_{\mathrm{U}}^{\star}]$,

4: The UAV relay feeds $\mathbf{H}_e^j(k) = \mathbf{G}_{\mathrm{RF2}} \mathbf{H}_1^j(k) \mathbf{F}_{\mathrm{RF}}^j$ back to each BS node

5: The $j^{th}$ BS designs $\mathbf{F}_{\mathrm{BB}}^j(k) = \mathbf{H}_e^j(k)^H (\mathbf{H}_e^j(k) \mathbf{H}_e^j(k)^H)^{-1}$ and normalizes

$\mathbf{F}_{\mathrm{BB}}^j(k) = \frac{\mathbf{F}_{\mathrm{BB}}^j(k)}{\|\mathbf{F}_{\mathrm{RF}}^j \mathbf{F}_{\mathrm{BB}}^j(k)\|_F}$

**Phase 2**

6: For each user $u$, the UAV relay and the user select and that solve:

$$\mathbf{r}_{\mathrm{u}}^{\star} = \underset{\mathbf{r}_{\mathrm{u}} \in \mathcal{G}_{RF1}}{\arg\max} \left\| \mathbf{H}_{2,u}(k) \mathbf{r}_{\mathrm{u}} \right\|, \quad \mathrm{u} = 1, ..., U,$$

7: UAV relay sets $\mathbf{G}_{\mathrm{RF1}} = [\mathbf{r}_1^{\star}, \mathbf{r}_2^{\star} ..., \mathbf{r}_U^{\star}]$,

8: For each user $u$, $\mathbf{h}_{ef}^u(k) = \mathbf{H}_{2,u}(k) \mathbf{G}_{\mathrm{RF1}}$, the user feeds back $\mathbf{h}_{ef}(k)$ to the UAV relay where: $\mathbf{h}_{ef}^u(k) = \arg\max \left\| (\mathbf{h}_{ef}^u(k))^H \mathbf{h}_{ef}^u(k) \right\|$,

9: The relay designs:

$\mathbf{G}_r(k) = \mathbf{H}_{ef}(k)^H (\mathbf{H}_{ef}(k) \mathbf{H}_{ef}(k)^H)^{-1}$, $\mathbf{H}_{ef}(k) = [\mathbf{h}_{ef}^1(k), ..., \mathbf{h}_{ef}^U(k)]$,

10: Finally normalizes :

$\mathbf{G}_r(k) = \frac{\mathbf{G}_r(k)}{\|\mathbf{G}_{\mathrm{RF1}} \mathbf{G}_r(k)\|_F}$

In the initialization step, we compute the distribution of both the BSs and the users in a specified region. The procedure mainly consists of two steps which is summarized in **Algorithm 7**. The first step deals with the users, while the other accounts for the distribution of the BSs. For the former, as a system parameter, the algorithm needs to know the rectangular area, $A_s$, the average density of users, $\lambda_a$ per $m^2$, the minimum separation between them, $d_U^{\min}$, in meters, and the number of users $U$. Using these parameters, users are distributed randomly using the afore-mentioned Matern type-I hard-core process. The average number of random distribution users in the rectangular area, $A_s$, is given as $\bar{U} = \lambda_a e^{(-\lambda_a d_U^{\min})} A_s$. Finally, we pick $U$ points out of the total generated points, hence getting the 2D locations of each user as $(x_u, y_u)$, where $u \in \bar{U}$. We distribute the BSs in the given area similarly by using same parameters as of the distribution of users, except for the separation distance being equal to $d_{\text{BS}}^{\min}$ and for the height of all BS fixed to a maximum defined height $z_j$. This provides 3D locations of the BSs as $(x_j, y_j, z_j)$.

**Algorithm 7** System Initialization

**Inputs:** $\text{N}_{BS}$, $U$, $A_s$, $\lambda_a$, $d_U^{\min}$ ,$d_{BS}^{\min}$, $z_j^{\max}$.

**Output:** $(x_i,y_i)$, $(x_j,y_j,z_j)$.

1: Distribution of users

2: $(x_u,y_u) \longleftarrow$ Matern Process($A_s$, $\lambda_a$, $d_U^{\min}$)

3: $(x_u,y_u) \longleftarrow$ Randomly select $U$ number of points out of the total $(x_u,y_u)$

4: Distribution of BSs

5: $(x_j,y_j) \longleftarrow$ Matern Process($A_s$, $\lambda_a$, $d_{BS}^{\min}$) and $z_j = z_j^{\max}$

Before modeling the problem, let us introduce the following constraints:

- User scheduling constraint: each user can be associated with only one BS at a time. Thus, we have:

$$\sum_{j=1}^{N_{\text{BS}}} A_{uj} \leq 1, u \in U \tag{5.33}$$

- QoS constraint for users:

$$\mathrm{SINR}_{uj} A_{uj} \geq \mathrm{SINR}_u^{\min}, \qquad \forall u, j, \tag{5.34}$$

where $\mathrm{SINR}_u^{\min}$ denotes the minimum SINR of the system. Our problem could afterwards be formulated as:

$$\max_{\{A_{uj}\}} \sum_{u=1}^{U} \sum_{j=1}^{N_{\mathrm{BS}}} (\chi R_{uj} + (\chi - 1)) A_{uj} \tag{5.35a}$$

$$\text{Subject to} \sum_{u=1}^{U} \sum_{j=1}^{\mathrm{N}_{BS}} R_{uj} A_{uj} \leq R \tag{5.35b}$$

$$\sum_{u=1}^{\mathrm{U}} A_{uj} b_{uj} \leq B_j, \qquad \forall j, \tag{5.35c}$$

$$\mathrm{SINR}_{uj} A_{uj} \geq \mathrm{SINR}_u^{\min}, \qquad \forall u, j, \tag{5.35d}$$

$$\sum_{u=1}^{\mathrm{U}} A_{uj} \leq N_l, \qquad \forall j, \tag{5.35e}$$

$$\sum_{j=1}^{N_{\mathrm{BS}}} A_{uj} \leq 1, \quad u \in U, \tag{5.35f}$$

$$A_{uj} \in \{0, 1\} \tag{5.35g}$$

$$x_{min} \leq x_u \leq x_{max} \tag{5.35h}$$

$$y_{min} \leq y_u \leq y_{max} \tag{5.35i}$$

where $\chi = \{0 \text{ or } 1\}$ is a weighting factor, and $\mathbf{A} \in C^{U \times N_{BS}}$ is the users-BSs association matrix, in which each element translates a simple correspondence law expressed as follows:

$$A_{uj} = \begin{cases} 1, & \text{if user } u \text{ is associated to BS } j \\ 0, & \text{otherwise.} \end{cases} \tag{5.36}$$

Before studying the optimization problem, the limiting factors that affect the communication between users and BSs are discussed below. Three major factors have a direct effect on the association of users and BSs, namely, data rate, bandwidth, number of links of the BSs. The objective function (5.35a) jointly maximizes the user-BSs association and their data rate, while constraint (5.35b) ensures that the wireless link between each user and BS has not less than a predefined data rate $R$. Constraint (5.35c) sets the upper limit of the offered bandwidth of each BS. Moreover, constraint (5.35d) satisfies a minimum SINR requirement of the system, (5.35e) assures that the users are associated to a $j^{th}$ BS via the UAV relay through $N_l$ links, and constraint (5.35f) restricts each user to be associated with only one BS. Constraints (5.35h) and (5.35i) show that it is necessary that the UAV relay 2D coordinates belong to the target area. Finding an optimal solution to such a problem may involve searching over continuous 3D coordinates of UAV relay and for every possible users-BSs association. In practice, problem (5.35a) is mathematically challenging as it involves a non-convex objective function, and non-convex and non-linear constraints. A description of the proposed algorithm to solve such a problem is given in **Algorithm 8**. This algorithm is designed to use the processing of two network nodes including users, and BSs communicating through one UAV relay link. Therefore, it is divided into two stages that are distributed among those nodes.

- Stage 1: Selection procedure:

  This stage is performed for each user individually, in which the users select the corresponding BSs on a one-to-one basis. During this selection procedure, the BSs send a broadcast initialization signal using multiple antennas beamforming, and following the "max SINR" rule, while the $u^{th}$ user picks up the BS which has the strongest signal by calculating the SINR at his level with all available BSs according to (5.19), sorts them in a decreasing order, and then compares their SINR with the minimum required SINR (line 4). In this case, the user connects to the nearest BSs that satisfies the constraint (5.35d). Then, it sends feedback with 1 to the selected BS corresponding to the maximum SINR if $A_{uj}$=1, and 0 feedback to others if their $A_{uj}$=0. Based on the obtained temporal association, a set of vectors $\mathcal{V} = [\mathcal{V}_1, ..., \mathcal{V}_j, ..., \mathcal{V}_{N_{\text{BS}}}]$ is created, where each vector $\mathcal{V}_j$ from $\mathcal{V}$ represents a list of possible users associated to individual BSs. The list of users is created by adding the $u^{th}$ user to the vector $\mathcal{V}_j$ corresponding to the serving BS $j$ (line 5). Then, based on the association, we decide which BSs should be turned off, as those BSs do not improve the users quality of service.

- Stage 2: BS control and decision:

  Based on the preferred BSs selected in Stage 1, each BS receives a number of association requests from a group of users. However, due to the limitation of available bandwidth, not all of them can eventually get associated with the BSs, so an admission control is required here to maximize the number of users and the sum-rate as per the objective criterion (5.35a). To do that, each BS $j$, on its turn, distributively chooses the users among those who requested to be associated and whom necessitating a minimum bandwidth (5.35c) and rejects the remaining users by modifying their request to $A_{uj} = 0$. Each rejected user attempts to connect to his second most preferred BS (based on the ordered set of indices), if no more bandwidth is left on this BS. Before associating the selected requesting users, the constraints of the maximum number of supported links $N_l$ (5.35e) and the data rate limit (5.35b) are verified, and then the association matrix $\mathbf{A}$ is updated. The process stops if all the requests of users are already entertained and no further request is remaining for the $j^{th}$ BS. By doing so, we have fulfilled the objective criterion of maximizing the sum-rate.

## 5.7 Simulation Results

In this section, simulation results are discussed to demonstrate the effectiveness of multi-user mm-Wave massive MIMO-OFDM system relying on an UAV AF relay, incorporating hybrid beamforming functionality. In the considered system both BSs and users are distributed over a square region of area $A_s = 4 \times 4\ km^2$, with an average density of $\lambda_a$= 2 $\times 10^{-6}$ per $m^2$, and a minimum separation of $d_{\text{BS}}^{\min} = 300m$ and $d_U^{\min} = 100m$. The operating frequency is 28 GHz frequency, and the bandwidth is 500 MHz. We assume the number of BSs is $N_{BS} = 3$, each equipped with $N_t = 64$ antennas, and supporting $U = 25$ single-antenna users. Without loss of generality, the UAV relay is assumed to hold 32 antennas and move with a velocity $v$= 30 km/h. The number of links $N_l = 7$, the applied data rate $R = 2$ Gbps, the maximum bandwidth B = 500 MHz and the minimum SINR is $-5$ dB. All the mm-Wave channels are assumed to experience multi-path fading, and has a number of path components $L = 3$, and the number of sub-carriers is $K = 64$. The performance metric of the system are taken as the achievable sum-rate and the users-BS association.

Figure 5.3 illustrates the achievable sum-rate versus the relay altitude for different values of its location in the horizontal plane, i.e $x_r$ and $y_r$, when SNR equals $-5$ dB.

**Algorithm 8** Two-stage distributed algorithm

**Inputs:** $\mathrm{N}_{BS}$, $\mathrm{B}_j$, $N_l$, $\vartheta_{uj}$, $U$, $b_{uj}$ , $R$, $\mathrm{SINR}_u^{\min}$

**Output:** The associated users **A**.

**Initialization** : $\mathbf{A} = \emptyset$;

1: Generate the association matrix **A**.

**Stage 1**

2: **for** $u$ from 1 to $U$, **do**

3: idx $=$ argmax$\{\vartheta_{uj}\}$ ;

4: $\mathcal{V}_{\text{idx}} = \mathcal{V}_{\text{idx}} \bigcup u$ ; indices of $\mathcal{V}_{\text{idx}}$ sorted in decreasing order.

5: **end for**

**Stage 2**

6: **for** $j = 1 : \mathrm{N_{BS}}$ **do**

7: Find max $R_{uj}$ with min $b_{uj}$

8: **if** $A_{ij} b_{uj} \leq B_j$, and update the indicators $A_{uj} = 0$;

9: **end for**

10: **Until** Bandwidth limit is reached or each user has been either connected.

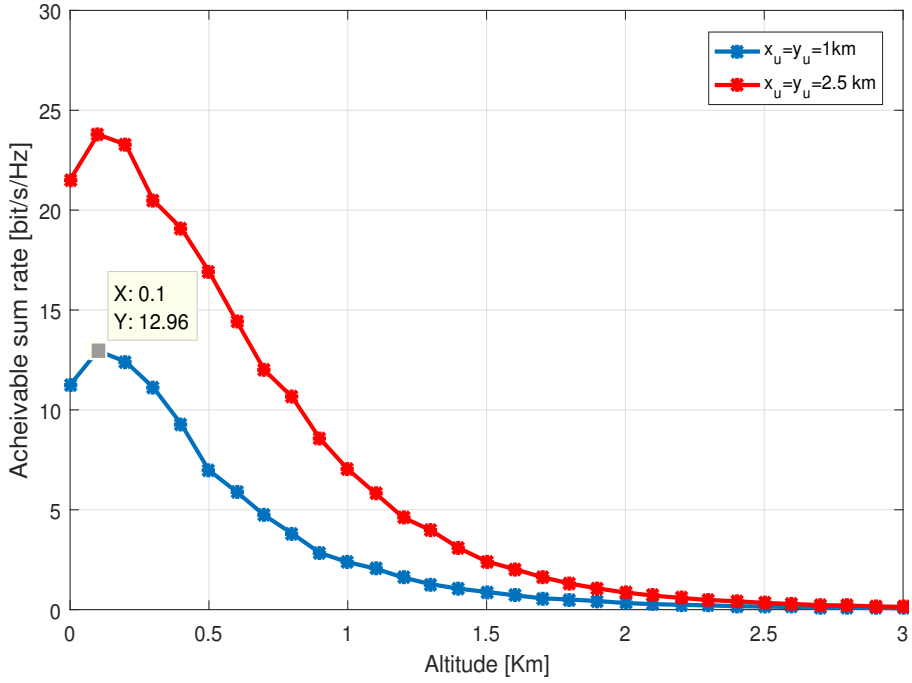


Figure 5.3: The achievable rate performance of the multi-user mm-Wave massive MIMO-OFDM system.

As we can see from this figure, the achievable sum-rate increases when the UAV's altitude gets higher. This might be due to the dual effects of higher probability of the presence of a LOS in the network when the altitude increases and to the efficient hybrid beamforming performed between the BSs and the relay to a certain value of the altitude. As it can be noted from Figure 5.3, the optimal UAV altitude which maximizes the attainable sum rate is 100 m, and beyond this value, the performance degrades to lead to the outage of the link at an altitude of 3 km. It is believed that this is owing to the fact that the mm-Wave signals suffer from high losses over long distances.

Figure 5.4 investigates the impingement of the incorporation of an UAV relay in the system, along with the effect of the retained altitude on the performance. The benefit of the relaying enriched with the hybrid beamforming finds its great efficiency at quite reasonable SNR values, when the UAV altitude is 100 m, since 20 bits/s/Hz performance gain is noted over the system with no relaying, when SNR is 10 dB. The alternative with no relay refers to the mm-Wave massive MIMO-OFDM aided-hybrid beamforming without UAV relay. On the other hand, when h=1km, the penalty of the path losses on the proposed system is such significant that the cooperative diversity system sees its performance become inferior to the one of the counterpart without a relaying device.

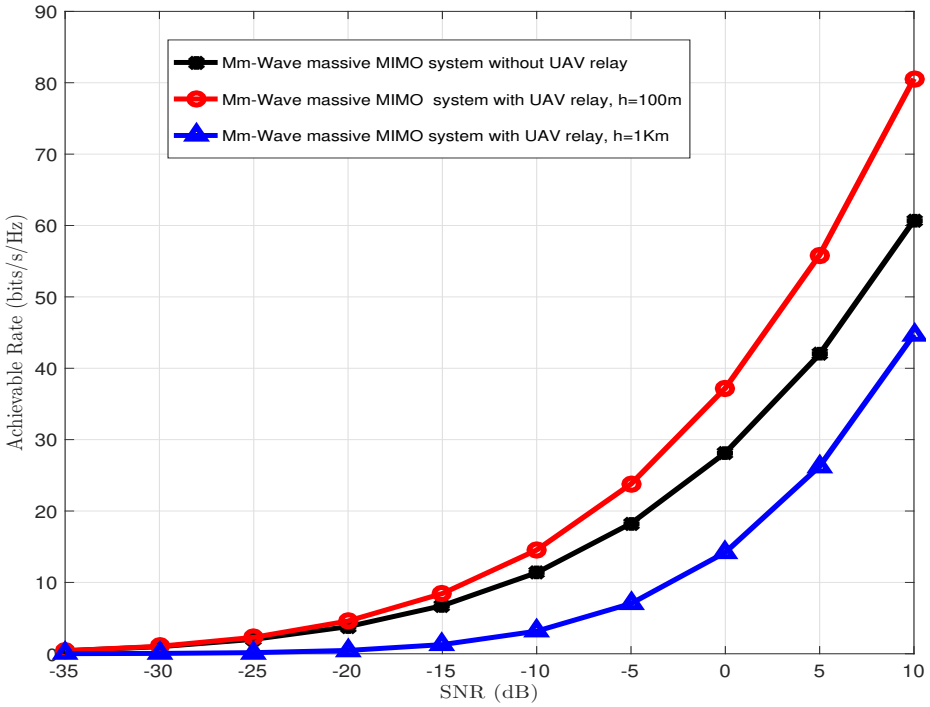


Figure 5.4: Impact of the presence of the relay on the sum rate performance of the multi-user mm-Wave massive MIMO-OFDM system.

Figure 5.5 investigates the achievable rate performance of the multi-user mm-Wave MIMO-OFDM system when using the hybrid, the analog, and the optimal digital beamforming structures. From this figure, it appears clearly that the analog beamforming-based structure achieves a significantly lower achievable rate than the one adopting optimal digital beamforming especialy at high SNR range. On the contrary, the proposed hybrid beamforming relay achieves near-optimal performance over the whole SNR range in consideration. This confirms the efficiency of the proposed hybrid beamforming relay scheme for multi-user mm-Wave MIMO-OFDM system.

In Figure 5.6, the achievable rate performance of the distributed BS antennas configuration of multi-user mm-Wave MIMO-OFDM system is compared with co-located antennas alternative, when using the same simulation parameters. From Figure 5.6, it is observed that, the gain in the achievable rate brought from retaining distributed BS configuration, in mm-Wave massive MIMO-OFDM system, is significant over the co-located antennas counterpart. This is due to the spatial correlation arising from co-localizing antennas in mm-Wave MIMO-OFDM system, which has a drastic effect on the achievable rate performance.

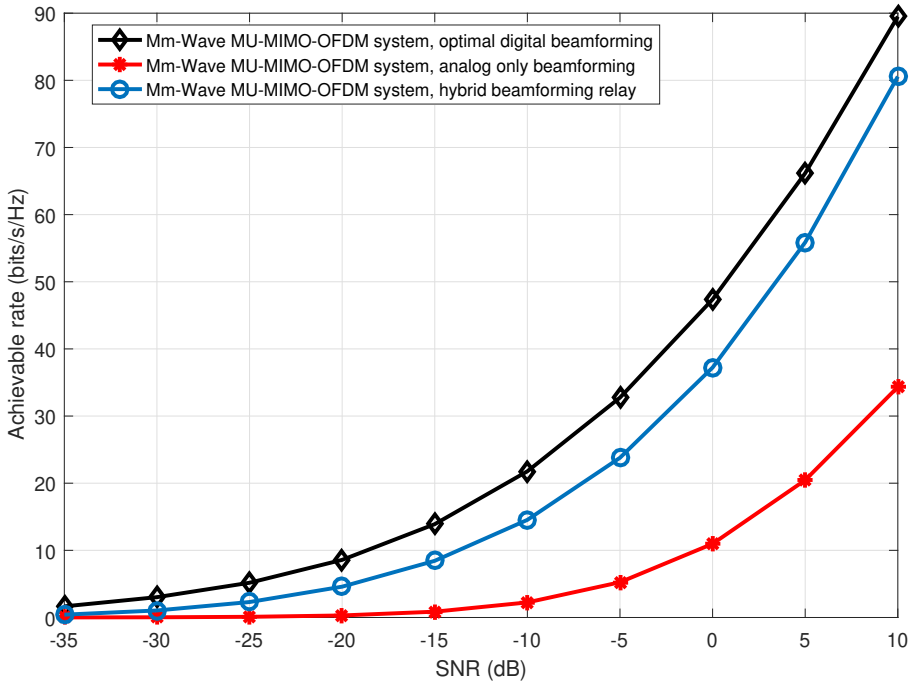


Figure 5.5: Achievable rates performance using the hybrid beamforming relay, analog beamforming and the optimal digital beamforming for the proposed system.

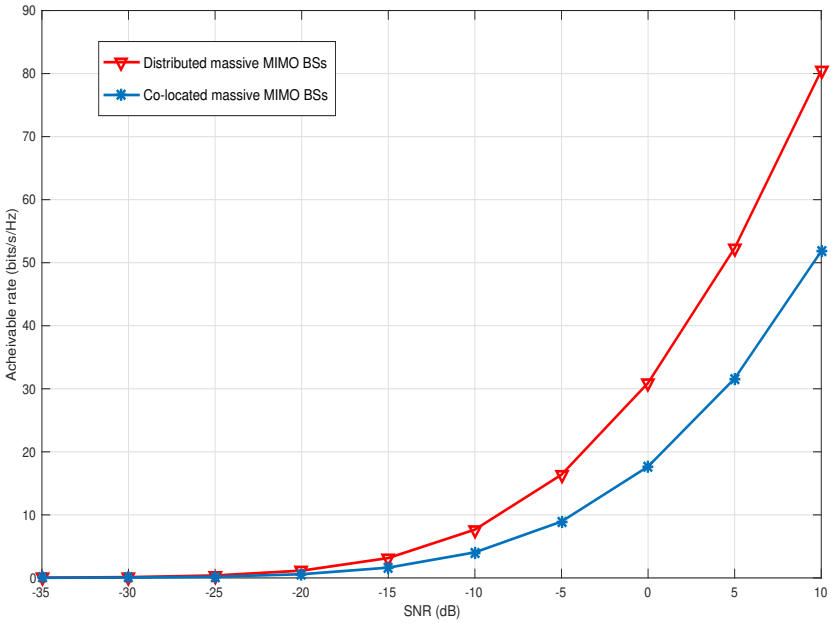


Figure 5.6: Achievable rate of large-scale distributed antennas and co-located MIMO against the SNR.

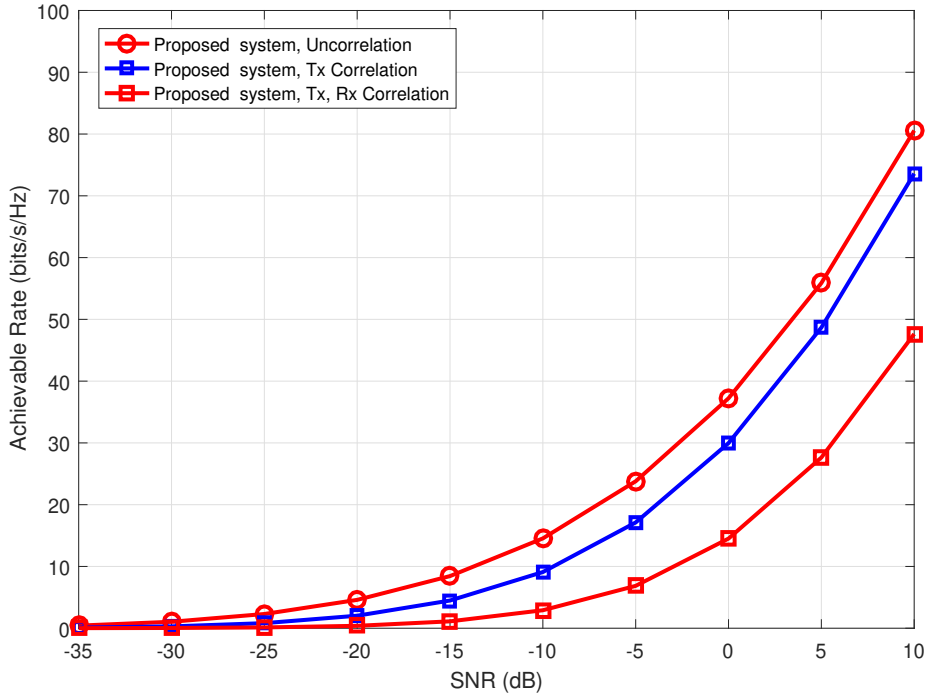


Figure 5.7: Performance of the proposed multi-user mm-Wave MIMO-OFDM system over spatial correlated underground channel

Figure 5.7 shows the impact of spatial correlation using Kronecker model on the achievable rate of multi-user mm-Wave MIMO-OFDM system, when the correlation parameter $r = 0.8$. From this figure, it is noted that the transmit side spatial correlation induces only a marginal effect on the achievable data rate. Assuming a high correlation at the transmit and the receive levels results in a more important achievable rate, in particular at high SNR range. However, the performance losses in this mm-Wave massive MIMO context remains reasonable, knowing that we have adopted this pessimistic assumption of high spatial correlation.

Figure 5.8 shows a spatial distribution of the BSs, the relay and the users, where the relay is placed at a fixed height $z_r = 100$ m in a possible configuration of the network. The figure shows also the user-BSs association through the served subscribers among the total, who are present in this flexible cell, for the multi-user mm-Wave massive MIMO-OFDM system with and without the UAV relay. The same distributed approach for optimization as in Algorithm 8 has been adapted to the scenario which does not involve a relay. It can be noted that the relay-based scheme allows to serve a higher number of users at a given time.

Figure 5.9 compares the number of users associated with each BS in multi-user mm-Wave MIMO-OFDM system with and without UAV relay, when the UAV relay

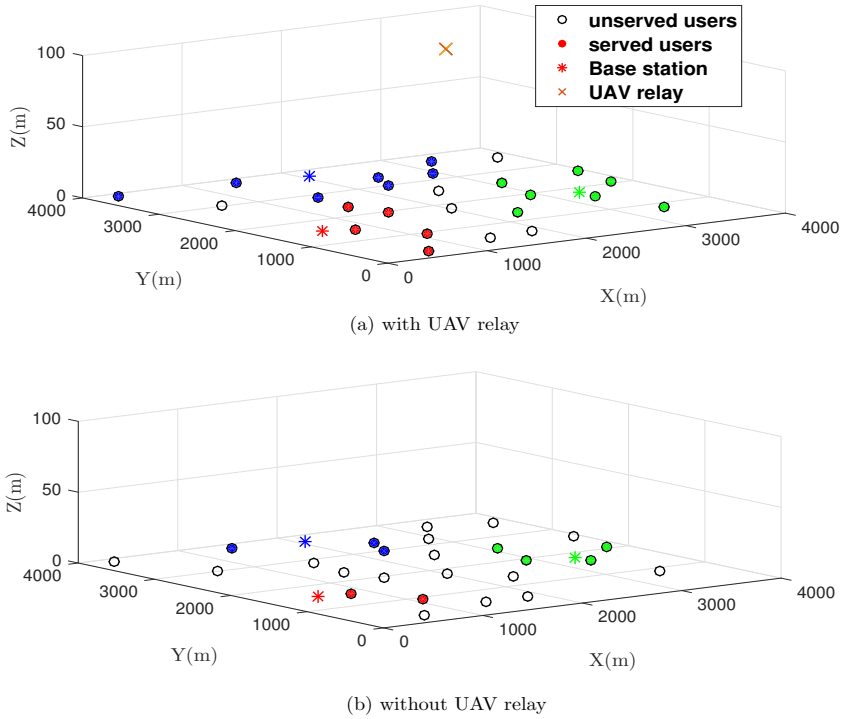


(a) with UAV relay

(b) without UAV relay

Figure 5.8: Users-BSs association for multi-user mm-Wave MIMO-OFDM system.

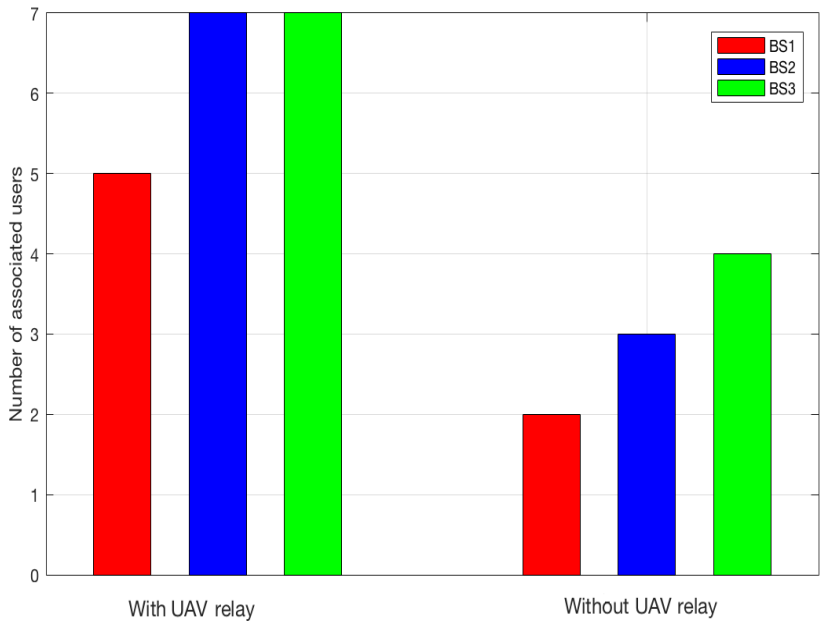


Figure 5.9: Associed user for multi-user mm-Wave MIMO-OFDM system with and without UAV relay.

altitude is $z_r = 100$. From this figure, we can note that the number of associated users with the help of a UAV relay, is superior to that without relay, regardless of the considered BS.

## 5.8 Conclusion

The influence of LOS blockage on mm-Wave communications is a very serious problem. In this chapter, we have presented a new design of UAV architecture, in which UAV operates as a multi antennas relay in a multi-user mm-Wave MIMO-OFDM communication context, thereby mitigating the drawbacks of blockage encountered in mm-Wave networks. Subsequently, a good link reliability between every BS and multiple ground users is maintained. To achieve such an objective, a two stage distributed algorithm which searches the best user-BSs association, while maximizing the sum user data rate, under spatial and bandwidth constraints in mm-Wave frequency band, is proposed. Furthermore, in order to mitigate the interference impediment and overcome the propagation losses in such environments, hybrid beamforming relay-thru scheme is adopted between the multiple BSs, the relay, and the ground users, merging the spatial processing and the AF operation. The proposed architecture was shown to achieve a quite satisfying sum-rate performance in the mm-Wave MIMO-OFDM system. Through simulations, we confirm the efficiency of the proposed multi-user mm-Wave MIMO-OFDM system and highlight the effect of the UAV altitude on the achievable rates. Furthermore, the performance of the proposed two stage distributed algorithm in terms of sum data rate and number of associated users was thouroughly presented.

# CHAPTER 6

# CONCLUSION

## Contents

Mm-Wave communications will be used in 5G mobile communication systems, but they experience severe path loss and have high sensitivity to physical objects, leading to complicated network architectures. A large multiple antennas arrays at both the transmitter and the receiver has been suggested and theoretically proven its efficiency in combination with hybrid beamforming structure. Based on mm-Wave multi antennas transmission, this thesis provides new architecture solutions in order to enhance the performance and the quality of transmissions at mm-Wave frequency bands. In particular, we have been interested in the underground communication at the 60 GHz band based on real channel measurements, which were performed in an underground mine environment. Since future communication systems dedicated to mm-Wave applications are calling for increasing users data rates, our focus has been turned to investigating the importance of using the UAV relay in urban environment.

## 6.1 Summary of Results and Insights

The proposed solutions in the considered context require knowledge of short-range transmission challenges of mm-Wave communications and beamforming methods to tackle the crucial problems faced by mm-Wave frequency bands. Through studies on current research advances on mm-Wave massive MIMO, we demonstrate directions to solve the limited transmission problems:

- We have presented a new MIMO underground system encompassing hybrid beamformer structure, in which the impact of hardware impairments have been incorporated in the transceiver processing. In addition, we proposed a 2-D geometrical channel model from one ring model using the real channel measurements carried out in a mine at the 60 GHz band. The proposed architecture aims at enhancing the achievable rate performance in the adverse underground wireless mm-Wave channels, while reducing the impingement of hardware transceivers practical defects on it. Through simulations, we have been demonstrated the higher performance and robustness against hardware imperfections of the proposed hybrid beamforming solution, relative to both analog beamforming and full digital beamforming-based counterpart. It has been proved that the impact of hardware impairments vanishes asymptotically as the number of
- We have firstly proposed a new iterative compressive estimation based on the

concept of forward and backward processing and applied to STBC-FBMC/QAM system. The proposed estimation algorithm is based on two consecutive processing steps for identifying the sparse components of the channel, which called forward selection and backward removal steps, in which iteratively expands and compresses the support estimate, and thus increase the accuracy of estimation without prior information of the sparsity level, hence improving the ability to cover up for the errors made in the conventional OMP algorithm. Through simulation results, it was shown that, in addition to the improvement of the channel estimation accuracy from a limited number of pilots, another important property of the proposed FB algorithm lies in its blindness to the sparsity level of the channel. While the hardware impairments are inherent in any practical communication system, the second contribution of this chapter concerned in investigating theirs impact on underground channel estimation when the transmitter and the receiver employ hybrid beamforming architectures. To do that accurately, we proposed an adaptive algorithm to estimate the mm-Wave underground channel based on CS technique using hierarchical multi-resolution codebook design for training beamforming. Through simulations results, we conclude that, the transceiver hardware impairments have a deleterious impact on the achievable rate and channel estimation.

- We have proposed a new design of UAV deployment in which UAV operates as a beamforming relay for short distance mm-Wave communication, thereby mitigating the drawbacks of both the blockage and the multi-user interference. Subsequently, a good link reliability between every ground BSs an users is maintained. To achieve such an objective, a two stage distributed algorithm which searches the best user-BSs association, while maximizing the sum user data rate, has derived. This is aided by exploiting hybrid beamforming between the BSs, the UAV relay, and the ground users thereby reducing the degrees of interference and complexity. Through simulation, we have confirmed the efficiency of the proposed multi-user mm-Wave MIMO-OFDM system and highlight the effect of the UAV altitude on the achievable rates. The performance of the proposed distributed algorithm in terms of sum data rate and the number of associated users have presented.

## 6.2 Future Works

On top of the advantages shown in this work that prove how MIMO architecture improve the total performance of mm-Wave communications, others important techniques of this work can be further improved, and more areas in MIMO technology that need to be further investigated. Following the work presented in this thesis, we conclude by offering several extensions related to the proposed schemes. Some potential major future directions here include:

- The 60 GHz channel measurements were carried for MIMO system, must be extended to massive MIMO architecture studied in Chapter 3.
- The multiplicative impairments models for large MIMO underground system need to be considered for future works and develop the analytical expression that can serve as performance metric to investigate practical system performance.
- Although the FB channel estimation proposed in Chapter 4, we can studied the proposed algorithm for the large MIMO systems.
- It would also be interesting to develop impairment-aware hybrid precoding and channel estimation solutions. Based on the insights that will be obtained from analyzing hybrid architectures under practical circuit models, it might be possible to design new optimized hybrid architectures, and channel estimation solutions that take these insights into consideration. Further, developing solutions that are more robust to the hardware impairments can boost the actual performance of hybrid architectures under practical conditions. Therefore, developing such hybrid architectures and associated signal processing solutions is important for future mm-Wave MIMO underground systems.
- Related to the work presented in Chapter 5, one promising extension would be to study the presence of eavesdropper in the system and finding a solution to secure the transmission in multi-user mm-Wave systems.

# BIBLIOGRAPHY


[1] N. Costa, S. Haykin, Multiple-input multiple-output channel models: Theory and practice, Vol. 65, John Wiley & Sons, 2010.

[2] J. Rodriguez, Fundamentals of 5G mobile networks, John Wiley & Sons, 2015.

[3] J. G. Andrews, S. Buzzi, W. Choi, S. V. Hanly, A. Lozano, A. C. Soong, J. C. Zhang, What will 5g be?, IEEE Journal on selected areas in communications 32 (6) (2014) 1065–1082.

[4] A. Gupta, R. K. Jha, A survey of 5g network: Architecture and emerging technologies, IEEE access 3 (2015) 1206–1232.

[5] E. Hossain, M. Hasan, 5g cellular: key enabling technologies and research challenges, arXiv preprint arXiv:1503.00674 (2015).

[6] I. F. Akyildiz, S. Nie, S.-C. Lin, M. Chandrasekaran, 5g roadmap: 10 key enabling technologies, Computer Networks 106 (2016) 17–48.

[7] F. Rusek, D. Persson, B. K. Lau, E. G. Larsson, T. L. Marzetta, O. Edfors, F. Tufvesson, Scaling up mimo: Opportunities and challenges with very large arrays, IEEE signal processing magazine 30 (1) (2013) 40–60.

[8] M. G. Bellanger, Specification and design of a prototype filter for filter bank based multicarrier transmission, in: icassp, Vol. 1, Citeseer, 2001, pp. 2417–2420.

[9] E. G. Larsson, O. Edfors, F. Tufvesson, T. L. Marzetta, Massive mimo for next generation wireless systems, IEEE Communications Magazine 52 (2) (2014) 186–195.

[10] H. Q. Ngo, E. G. Larsson, T. L. Marzetta, Energy and spectral efficiency of very large multiuser mimo systems, IEEE Transactions on Communications 61 (4) (2013) 1436–1449.

[11] T. L. Marzetta, Noncooperative cellular wireless with unlimited numbers of base station antennas, IEEE Transactions on Wireless Communications 9 (11) (2010) 3590–3600.

[12] S. Rangan, T. S. Rappaport, E. Erkip, Millimeter-wave cellular wireless networks: Potentials and challenges, Proceedings of the IEEE 102 (3) (2014) 366–385.

[13] Z. Pi, F. Khan, An introduction to millimeter-wave mobile broadband systems, IEEE communications magazine 49 (6) (2011) 101–107.

[14] P. Smulders, Exploiting the 60 ghz band for local wireless multimedia access: Prospects and future directions, IEEE communications magazine 40 (1) (2002) 140–147.

[15] S.-K. Yong, P. Xia, A. Valdes-Garcia, 60GHz Technology for Gbps WLAN and WPAN: from Theory to Practice, John Wiley & Sons, 2011.

[16] S. A. M. Tariq, Characterization and modelling of scattered wireless channel at 60 ghz in an underground mine gallery, Ph.D. thesis, École Polytechnique de Montréal (2016).

[17] M. Ghaddar, L. Talbi, M. Nedil, I. B. Mabrouk, T. A. Denidni, Mm-waves propagation measurements in underground mine using directional mimo antennas, IET Microwaves, Antennas & Propagation 10 (5) (2016) 517–524.

[18] B. Farhang-Boroujeny, Filter bank multicarrier modulation: A waveform candidate for 5g and beyond, Advances in Electrical Engineering 2014 (2014).

[19] R. Nissel, E. Zöchmann, M. Lerch, S. Caban, M. Rupp, Low-latency miso fbmc-oqam: It works for millimeter waves!, in: 2017 IEEE MTT-S International Microwave Symposium (IMS), IEEE, 2017, pp. 673–676.

[20] I. B. Mabrouk, L. Talbi, M. Nedil, Y. Coulibaly, T. Denidni, Effect of antenna directivity on performance of multiple input multiple output systems in an underground gold mine, IET microwaves, antennas & propagation 6 (5) (2012) 555–561.

[21] K. Ghanem, M. Nedil, S. Azzeddine, N. Kandil, T. Denidni, Achievable capacity in underground channels using mimo antenna systems, in: Antennas and Propagation Society International Symposium (APSURSI), 2013 IEEE, IEEE, 2013, pp. 378–379.

[22] I. B. Mabrouk, L. Talbi, M. Nedil, K. Hettak, Mimo-uwb channel characterization within an underground mine gallery, IEEE Transactions on Antennas and Propagation 60 (10) (2012) 4866–4874.

[23] M. El Khaled, P. Fortier, M. L. Ammari, A performance study of line-of-sight millimeter-wave underground mine channel, IEEE Antennas and Wireless Propagation Letters 13 (2014) 1148–1151.

[24] M. Ghaddar, L. Talbi, M. Nedil, I. B. Mabrouk, T. A. Denidni, Mm-waves propagation measurements in underground mine using directional mimo antennas, IET Microwaves, Antennas & Propagation 10 (5) (2016) 517–524.

[25] C. Studer, M. Wenk, A. Burg, Mimo transmission with residual transmit-rf impairments, in: Smart Antennas (WSA), 2010 International ITG Workshop on, IEEE, 2010, pp. 189–196.

[26] E. Björnson, J. Hoydis, M. Kountouris, M. Debbah, Massive mimo systems with non-ideal hardware: Energy efficiency, estimation, and capacity limits, IEEE Transactions on Information Theory 60 (11) (2014) 7112–7139.

[27] E. Björnson, M. Matthaiou, M. Debbah, Massive mimo with non-ideal arbitrary arrays: Hardware scaling laws and circuit-aware design, IEEE Transactions on Wireless Communications 14 (8) (2015) 4353–4368.

[28] S. Rangan, T. S. Rappaport, E. Erkip, Millimeter-wave cellular wireless networks: Potentials and challenges, Proceedings of the IEEE 102 (3) (2014) 366–385.

[29] A. S. Poon, M. Taghivand, Supporting and enabling circuits for antenna arrays in wireless communications, Proceedings of the IEEE 100 (7) (2012) 2207–2218.

[30] A. Alkhateeb, J. Mo, N. Gonzalez-Prelcic, R. W. Heath, Mimo precoding and combining solutions for millimeter-wave systems, IEEE Communications Magazine 52 (12) (2014) 122–131.

[31] A. Alkhateeb, O. El Ayach, G. Leus, R. W. Heath, Channel estimation and hybrid precoding for millimeter wave cellular systems, IEEE Journal of Selected Topics in Signal Processing 8 (5) (2014) 831–846.

[32] X. Xue, T. E. Bogale, X. Wang, Y. Wang, L. B. Le, Hybrid analog-digital beamforming for multiuser mimo millimeter wave relay systems, in: 2015 IEEE/CIC International Conference on Communications in China (ICCC), IEEE, 2015, pp. 1–7.

[33] J. Rodríguez-Fernández, N. González-Prelcic, K. Venugopal, R. W. Heath, Frequency-domain compressive channel estimation for frequency-selective hybrid millimeter wave mimo systems, IEEE Transactions on Wireless Communications 17 (5) (2018) 2946–2960.

[34] A. Alkhateeby, G. Leusz, R. W. Heath, Compressed sensing based multi-user millimeter wave systems: How many measurements are needed?, in: Acoustics, Speech and Signal Processing (ICASSP), 2015 IEEE International Conference on, IEEE, 2015, pp. 2909–2913.

[35] P. Schniter, A. Sayeed, Channel estimation and precoder design for millimeter-wave communications: The sparse way, in: Signals, Systems and Computers, 2014 48th Asilomar Conference on, IEEE, 2014, pp. 273–277.

[36] S. Singh, M. N. Kulkarni, A. Ghosh, J. G. Andrews, Tractable model for rate in self-backhauled millimeter wave cellular networks, IEEE Journal on Selected Areas in Communications 33 (10) (2015) 2196–2211.

[37] S. Biswas, S. Vuppala, J. Xue, T. Ratnarajah, On the performance of relay aided millimeter wave networks, IEEE Journal of Selected Topics in Signal Processing 10 (3) (2016) 576–588.

[38] L. Sboui, H. Ghazzai, Z. Rezki, M.-S. Alouini, Achievable rate of multi-relay cognitive radio mimo channel with space alignment, in: International Conference on Cognitive Radio Oriented Wireless Networks, Springer, 2015, pp. 17–29.

[39] S. S. Soliman, N. C. Beaulieu, Exact analysis of dual-hop af maximum end-to-end snr relay selection, IEEE Transactions on Communications 60 (8) (2012) 2135–2145.

[40] M. Asadpour, B. Van den Bergh, D. Giustiniano, K. A. Hummel, S. Pollin, B. Plattner, Micro aerial vehicle networks: An experimental analysis of challenges and opportunities, IEEE Communications Magazine (2014).

[41] E. P. De Freitas, T. Heimfarth, I. F. Netto, C. E. Lino, C. E. Pereira, A. M. Ferreira, F. R. Wagner, T. Larsson, Uav relay network to support wsn connectivity, in: Ultra Modern Telecommunications and Control Systems and Workshops (ICUMT), 2010 International Congress on, IEEE, 2010, pp. 309–314.

[42] X. Xue, Y. Wang, L. Dai, C. Masouros, Relay hybrid precoding design in millimeter-wave massive mimo systems, IEEE Transactions on Signal Processing 66 (8) (2018) 2011–2026.

[43] S. Zhang, H. Zhang, Q. He, K. Bian, L. Song, Joint trajectory and power optimization for uav relay networks, IEEE Communications Letters 22 (1) (2018) 161–164.

[44] A. Merwaday, I. Guvenc, Uav assisted heterogeneous networks for public safety communications, in: 2015 IEEE wireless communications and networking conference workshops (WCNCW), IEEE, 2015, pp. 329–334.

[45] S. A. W. Shah, T. Khattab, M. Z. Shakir, M. O. Hasna, A distributed approach for networked flying platform association with small cells in 5g+ networks, in: GLOBECOM 2017-2017 IEEE Global Communications Conference, IEEE, 2017, pp. 1–7.

[46] S. Goyal, M. Mezzavilla, S. Rangan, S. Panwar, M. Zorzi, User association in 5g mmwave networks, in: 2017 IEEE Wireless Communications and Networking Conference (WCNC), IEEE, 2017, pp. 1–6.

[47] Y. Lin, W. Yu, Optimizing user association and frequency reuse for heterogeneous network under stochastic model, in: 2013 IEEE global communications conference (GLOBECOM), IEEE, 2013, pp. 2045–2050.

[48] T. E. Bogale, L. B. Le, Massive mimo and mmwave for 5g wireless hetnet: Potential benefits and challenges, IEEE Vehicular Technology Magazine 11 (1) (2016) 64–75.

[49] S. M. Alamouti, A simple transmit diversity technique for wireless communications, 1998 (1998).

[50] B. Farhang-Boroujeny, Ofdm versus filter bank multicarrier, IEEE signal processing magazine 28 (3) (2011) 92–112.

[51] J. Du, S. Signell, Comparison of cp-ofdm and ofdm/oqam in doubly dispersive channels, in: Future Generation Communication and Networking (FGCN 2007), Vol. 2, IEEE, 2007, pp. 207–211.

[52] Q. Bai, J. A. Nossek, On the effects of carrier frequency offset on cyclic prefix based ofdm and filter bank based multicarrier systems, in: 2010 IEEE 11th International Workshop on Signal Processing Advances in Wireless Communications (SPAWC), IEEE, 2010, pp. 1–5.

[53] P. Siohan, C. Siclet, N. Lacaille, Analysis and design of ofdm/oqam systems based on filterbank theory, IEEE transactions on signal processing 50 (5) (2002) 1170–1183.

[54] M. Bellanger, Fs-fbmc: An alternative scheme for filter bank based multicarrier transmission, in: 2012 5th International Symposium on Communications, Control and Signal Processing, IEEE, 2012, pp. 1–4.

[55] C. Lélé, P. Siohan, R. Legouable, The alamouti scheme with cdma-ofdm/oqam, EURASIP Journal on Advances in Signal Processing 2010 (2010) 2.

[56] M. Renfors, T. Ihalainen, T. H. Stitz, A block-alamouti scheme for filter bank based multicarrier transmission, in: 2010 European Wireless Conference (EW), IEEE, 2010, pp. 1031–1037.

[57] R. Zakaria, D. Le Ruyet, M. Bellanger, Maximum likelihood detection in spatial multiplexing with fbmc, in: 2010 European Wireless Conference (EW), IEEE, 2010, pp. 1038–1041.

[58] H. Nam, M. Choi, S. Han, C. Kim, S. Choi, D. Hong, A new filter-bank multicarrier system with two prototype filters for qam symbols transmission and reception, IEEE Transactions on Wireless Communications 15 (9) (2016) 5998–6009.

[59] A. Goldsmith, S. A. Jafar, N. Jindal, S. Vishwanath, Capacity limits of mimo channels, IEEE Journal on selected areas in Communications 21 (5) (2003) 684–702.

[60] H. Q. Ngo, E. G. Larsson, T. L. Marzetta, Aspects of favorable propagation in massive mimo, in: 2014 22nd European Signal Processing Conference (EUSIPCO), IEEE, 2014, pp. 76–80.

[61] X. Gao, O. Edfors, F. Rusek, F. Tufvesson, Massive mimo performance evaluation based on measured propagation data, IEEE Transactions on Wireless Communications 14 (7) (2015) 3899–3911.

[62] R. W. Heath, N. Gonzalez-Prelcic, S. Rangan, W. Roh, A. M. Sayeed, An overview of signal processing techniques for millimeter wave mimo systems, IEEE journal of selected topics in signal processing 10 (3) (2016) 436–453.

[63] D. T. Emerson, The work of jagadis chandra bose: 100 years of millimeter-wave research, IEEE Transactions on Microwave Theory and Techniques 45 (12) (1997) 2267–2273.

[64] C. Park, T. S. Rappaport, Short-range wireless communications for next-generation networks: Uwb, 60 ghz millimeter-wave wpan, and zigbee, IEEE Wireless Communications 14 (4) (2007) 70–78.

[65] S. K. Yong, C.-C. Chong, An overview of multigigabit wireless through millimeter wave technology: Potentials and technical challenges, EURASIP journal on wireless communications and networking 2007 (1) (2007) 50–50.

[66] M. R. Akdeniz, Y. Liu, M. K. Samimi, S. Sun, S. Rangan, T. S. Rappaport, E. Erkip, Millimeter wave channel modeling and cellular capacity evaluation, IEEE journal on selected areas in communications 32 (6) (2014) 1164–1179.

[67] S. A. M. Tariq, C. Despins, S. Affes, C. Nerguizian, Statistical modeling of 60 ghz wireless channel in an underground mine gallery, in: Ubiquitous Wireless Broadband (ICUWB), 2015 IEEE International Conference on, IEEE, 2015, pp. 1–5.

[68] I. B. Mabrouk, J. Hautcoeur, L. Talbi, M. Nedil, K. Hettak, Feasibility of a millimeter-wave mimo system for short-range wireless communications in an underground gold mine, IEEE Transactions on Antennas and Propagation 61 (8) (2013) 4296–4305.

[69] E. J. Candès, M. B. Wakin, An introduction to compressive sampling, IEEE signal processing magazine 25 (2) (2008) 21–30.

[70] W. U. Bajwa, J. Haupt, A. M. Sayeed, R. Nowak, Compressed channel sensing: A new approach to estimating sparse multipath channels, Proceedings of the IEEE 98 (6) (2010) 1058–1076.

[71] T. S. Rappaport, S. Sun, R. Mayzus, H. Zhao, Y. Azar, K. Wang, G. N. Wong, J. K. Schulz, M. Samimi, F. Gutierrez, Millimeter wave mobile communications for 5g cellular: It will work!, IEEE access 1 (2013) 335–349.

[72] A. L. Swindlehurst, E. Ayanoglu, P. Heydari, F. Capolino, Millimeter-wave massive mimo: The next wireless revolution?, IEEE Communications Magazine 52 (9) (2014) 56–62.

[73] R. W. Heath, N. Gonzalez-Prelcic, S. Rangan, W. Roh, A. M. Sayeed, An overview of signal processing techniques for millimeter wave mimo systems, IEEE journal of selected topics in signal processing 10 (3) (2016) 436–453.

[74] J. Wang, Z. Lan, C.-W. Pyo, T. Baykas, C.-S. Sum, M. A. Rahman, R. Funada, F. Kojima, I. Lakkis, H. Harada, et al., Beam codebook based beamforming protocol for multi-gbps millimeter-wave wpan systems, in: GLOBECOM 2009-2009 IEEE Global Telecommunications Conference, IEEE, 2009, pp. 1–6.

[75] S. Hur, T. Kim, D. J. Love, J. V. Krogmeier, T. A. Thomas, A. Ghosh, Millimeter wave beamforming for wireless backhaul and access in small cell networks, IEEE transactions on communications 61 (10) (2013) 4391–4403.

[76] S. Akoum, O. El Ayach, R. W. Heath, Coverage and capacity in mmwave cellular systems, in: 2012 conference record of the forty sixth Asilomar conference on signals, systems and computers (ASILOMAR), IEEE, 2012, pp. 688–692.

[77] A. Ghosh, T. A. Thomas, M. C. Cudak, R. Ratasuk, P. Moorut, F. W. Vook, T. S. Rappaport, G. R. MacCartney, S. Sun, S. Nie, Millimeter-wave enhanced local area systems: A high-data-rate approach for future wireless networks, IEEE Journal on Selected Areas in Communications 32 (6) (2014) 1152–1163.

[78] E. G. Larsson, O. Edfors, F. Tufvesson, T. L. Marzetta, Massive mimo for next generation wireless systems, arXiv preprint arXiv:1304.6690 (2013).

[79] L. Kong, L. Ye, F. Wu, M. Tao, G. Chen, A. V. Vasilakos, Autonomous relay for millimeter-wave wireless communications, IEEE Journal on Selected Areas in Communications 35 (9) (2017) 2127–2136.

[80] E. Bjornson, P. Zetterberg, M. Bengtsson, B. Ottersten, Capacity limits and multiplexing gains of mimo channels with transceiver impairments, IEEE Communications Letters 17 (1) (2012) 91–94.

[81] J. Zhang, L. Dai, X. Zhang, E. Björnson, Z. Wang, Achievable rate of rician large-scale mimo channels with transceiver hardware impairments, IEEE Transactions on Vehicular Technology 65 (10) (2015) 8800–8806.

[82] D.-S. Shiu, G. J. Foschini, M. J. Gans, J. M. Kahn, Fading correlation and its effect on the capacity of multielement antenna systems, IEEE Transactions on communications 48 (3) (2000) 502–513.

[83] S. Buzzi, C. D'Andrea, On clustered statistical mimo millimeter wave channel simulation, arXiv preprint arXiv:1604.00648 (2016).

[84] S. Yoo, J. Lee, K. Kim, Geometry-based one-ring models for mimo systems: Modeling accuracy assessment and improvement, IEEE Transactions on Wireless Communications 15 (7) (2016) 4583–4597.

[85] J. A. Tropp, A. C. Gilbert, Signal recovery from random measurements via orthogonal matching pursuit, IEEE Transactions on information theory 53 (12) (2007) 4655–4666.

[86] O. Kolawole, A. Papazafeiropoulos, T. Ratnarajah, Impact of hardware impairments on mmwave mimo systems with hybrid precoding, in: 2018 IEEE Wireless Communications and Networking Conference (WCNC), IEEE, 2018, pp. 1–6.

[87] T. Kailath, A. H. Sayed, B. Hassibi, Linear estimation, no. BOOK, Prentice Hall, 2000.

[88] B. Kwon, S. Kim, D. Jeon, S. Lee, Iterative interference cancellation and channel estimation in evolved multimedia broadcast multicast system using filter-bank multicarrier-quadrature amplitude modulation, IEEE Transactions on Broadcasting 62 (4) (2016) 864–875.

[89] T. Zhang, Adaptive forward-backward greedy algorithm for learning sparse representations, IEEE transactions on information theory 57 (7) (2011) 4689–4708.

[90] M. Rossi, A. M. Haimovich, Y. C. Eldar, Spatial compressive sensing for mimo radar, IEEE Transactions on Signal Processing 62 (2) (2013) 419–430.

[91] M. A. Iwen, A. H. Tewfik, Adaptive strategies for target detection and localization in noisy environments, IEEE Transactions on Signal Processing 60 (5) (2012) 2344–2353.

[92] J. Zhao, F. Gao, W. Jia, S. Zhang, S. Jin, H. Lin, Angle domain hybrid precoding and channel tracking for millimeter wave massive mimo systems, IEEE Transactions on Wireless Communications 16 (10) (2017) 6868–6880.

[93] B. Matérn, Spatial variation, Vol. 36, Springer Lecture Notes in Statistics, 1986.

[94] L. Liang, W. Xu, X. Dong, Low-complexity hybrid precoding in massive multiuser mimo systems, IEEE Wireless Communications Letters 3 (6) (2014) 653–656.

[95] M. Mozaffari, W. Saad, M. Bennis, M. Debbah, Optimal transport theory for cell association in uav-enabled cellular networks, IEEE Communications Letters 21 (9) (2017) 2053–2056.

[96] J. Zhao, F. Gao, L. Kuang, Q. Wu, W. Jia, Channel tracking with flight control system for uav mmwave mimo communications, IEEE Communications Letters 22 (6) (2018) 1224–1227.

[97] J. Lee, Y. H. Lee, Af relaying for millimeter wave communication systems with hybrid rf/baseband mimo processing, in: Communications (ICC), 2014 IEEE International Conference on, IEEE, 2014, pp. 5838–5842.

[98] W. Xu, J. Liu, S. Jin, X. Dong, Spectral and energy efficiency of multi-pair massive mimo relay network with hybrid processing, IEEE Transactions on Communications 65 (9) (2017) 3794–3809.